Trace Gas Analysis of Krypton for the XENON Dark Matter Project

Hans Kettling

Diplomarbeit

Institut für Kernphysik
Mathematisch-Naturwissenschaftliche Fakultät
Westfälische Wilhelms-Universität Münster

Februar 2012

Westfälische
Wilhelms-Universität
Münster

Referent:	Prof. Dr. C. Weinheimer
Korreferent:	Prof. Dr. A. Khoukaz

There is a theory which states that if ever anyone discovers exactly what the Universe is for and why it is here, it will instantly disappear and be replaced by something even more bizarre and inexplicable.

There is another theory which states that this has already happened.

Douglas Adams

Abstract

In the last decades it has become evident that the evolution of our universe and the matter it consists of are dominated by so far unknown components. The Standard Model of particle physics only describes about 5 % of the universe's composition. The other unknown components are called Dark Matter and Dark Energy which contribute to the energy distribution of the universe by about 25 % and 70 %, respectively.

The XENON Project searches for Dark Matter by detecting the nuclear recoil signal induced by a Weakly Interacting Massive Particle (WIMP) in a two phase xenon time projection chamber (TPC). Interactions in the liquid phase cause scintillation and ionization signals. The electrons are drifted from the liquid into the gaseous phase and accelerated there, causing fluorescence light. Both light signals are detected by arrays of photosensitive detectors. The efficiency of the detector strongly depends on the purity of the xenon. In particular β-decay of ^{85}Kr constitutes one of the fundamental backgrounds of the experiment.

Therefore the group of Prof. Dr. C. Weinheimer at Münster, who is one of the collaborators of the XENON Project, develops among other things a cryogenic distillation column in order to reduce the level of krypton contamination in xenon to the low ppt[1] range.

This thesis presents a purity analysis for trace amounts of krypton in xenon based on mass spectrometry. In particular the sensitivity of the mass spectrometry technique is enhanced by orders of magnitude by a cold trap with liquid nitrogen, exploiting the differences in vapor pressure of krypton and xenon at temperatures around 77 kelvin.

This cold trap enhanced mass spectrometry technique provides a sensitivity of ~ 100 ppt and therefore gives rise to a utile diagnostic tool for the development of a cryogenic distillation column.

The setup has been tested to determine the krypton concentration in commercially available xenon gas from *AirLiquide*. The obtained value of (1.1 ± 0.4) ppb notably agrees with the reference paper from the company, who could only give an upper limit of < 10 ppb, but shows that the technique has a much higher precision and can be used to determine the krypton concentration in xenon accurately.

---

[1] ppt = parts per trillion = 10^{-12}

Zusammenfassung

In den letzten Jahrzehnten wurde entdeckt, dass die Evolution des Universums und seine Materiedichte fast ausschließlich von unbekannten Komponenten bestimmt wird. Das Standardmodell der Teilchenphysik ist lediglich in der Lage 5 % der Zusammensetzung des Universums zu beschreiben. Die übrigen unbekannten Komponenten werden Dunkle Materie und Dunkle Energie genannt, welche jeweils 25 % und 70 % der Energiedichte ausmachen.

Das XENON Dark Matter Projekt sucht nach Dunkler Materie indem es einen Kernrückstoß eines schwach wechselwirkenden massiven Teilchens (engl. WIMP) in einer zwei Phasen Xenon Zeitprojektionskammer (engl. TPC) nachweist. Wechselwirkungen im flüssigen Xenon führen zu Szintillation und Ionization.

Die entstehenden Elektronen werden von der flüssigen in die Gasphase gedriftet und dort weiter beschleunigt wobei erneut Szintiallationslicht entsteht. Beide Szintillationssignale werden von Photomultipliern detektiert.

Die Effizienz des Detetors hängt stark von der Reinheit des Xenongases ab. Insbesondere der β-Zerfall von ^{85}Kr verursacht eines der Hauptstörsignale des Experimentes.

Deshalb entwickelt die Arbeitsgruppe von Prof. Dr. C. Weinheimer aus Münster, welche einer der Kollaborationspartner des XENON Projektes ist, unter anderem eine Destillationssäule für Krypton, um die Menge an Krypton Verunreinigungen im Xenongas auf ppt[2] Niveau zu verringern.

In dieser Diplomarbeit wird eine Spurenanalyse zur Detektion von Kryptonverunreinigungen in Xenongas basierend auf der Technik der Massenspektrometrie behandelt. Kernpunkt ist die Verbesserung der Messempfindlichkeit der Massenspektrometrie um mehrere Größenordnungen durch eine zusätzliche Kältefalle mit flüssigem Stickstoff, welche die unterschiedlichen Dampfdrücke von Krypton und Xenon bei 77 Kelvin nutzt. Die Kombination der Massenspektrometrie mit einer Kältefalle ermöglicht eine Nachweisgrenze von ~ 100 ppt und stellt somit ein wichtiges Diagnostikinstrument für die Entwicklung der Destillationssäule dar.

Experimentell wurde die Kryptonkonzentration im Xenongas der Firma *AirLiquide* untersucht. Der ermittelte Wert von (1.1 ± 0.4) ppb stimmt mit der Spezifikation der Firma überein, die lediglich eine obere Grenze von < 10 ppb für die Kryptonkonzentration angeben konnte.

---

[2] engl. ppt = parts per trillion = 10^{-12}

Contents

1. Introduction

Two of the major questions of humankind are where we come from and what our world is made of. For thousands of years people have tried to answer these and similar questions both from theological and scientific points of view. In the last decades it has become evident that the evolution of our universe and the matter it consists of are dominated by so far unknown components. The Standard Model of particle physics only describes about 5 % of the universe's composition. The other unknown components are called Dark Matter and Dark Energy which contribute to the energy distribution of the universe by about 25 % and 70 %, respectively.

The XENON Project searches for Dark Matter by detecting the nuclear recoil signal induced by Dark Matter in the form of a Weakly Interacting Massive Particle (WIMP) in a two phase xenon time projection chamber (TPC). β-decay of ^{85}Kr constitutes one of the fundamental backgrounds of the experiment. Therefore the group of Prof. Dr. C. Weinheimer at Münster, who is one of the collaborators of the XENON Project, develops among other things a cryogenic krypton distillation column in order to reduce the level of krypton contamination to the low ppt[1] range.

In this thesis several evidence for Dark Matter, as well as a theoretical discussion are presented in chapter 2. Furthermore the direct detection method of the XENON Dark Matter Project is described in more detail in chapter 3. In particular the currently running XENON100 experiment and the research and development (R&D) for its successor XENON1T performed at Münster are described. The following chapter (4) deals with different detection and purification methods for krypton contaminations in xenon in general. Chapter 5 covers a detailed description of the experimental setup developed during this thesis for detection of trace amounts of krypton in xenon. The experimental results as well as previous calibration measurements are presented in chapters 6, 7 and 8. An overall summary follows in chapter 9.

---

[1] ppt = parts per trillion = 10^{-12}

2. Theory of Dark Matter

In this chapter several evidence for Dark Matter as well as the properties of possible Dark Matter candidates are outlined.
Furthermore, the concept of supersymmetry, which naturally gives rise to one of the most favored Dark Matter candidates, is introduced. Finally, different detection methods for this well motivated candidate are discussed.

2.1. Evidence for Dark Matter

Today there is overwhelming evidence for the existence of Dark Matter, although its direct detection has not been confirmed yet. There are plenty of experiments searching for this new type of matter. Some experiments like DAMA [Ber08] and CoGeNT [Aal11] have claimed a detection, but these results are in conflict with most of the other experiments which have better sensitivities and have not detected any signals so far.
Without claiming completeness some of the most important evidence for Dark Matter are presented in the following sections.

2.1.1. Galactic rotation curves

In 1933 Zwicky [Zwi33] discovered that the velocity dispersion of galaxies within the Coma Cluster deviates from the expected dispersion. As the velocity of outer galaxies was much too high to be caused by the observed visible mass, he stated that there is also some non-visible[1] matter present in the cluster and coined the term *Dark Matter*. Later on in the 1970s Rubin confirmed this hypothesis with her studies of the rotational velocities of stars in spiral galaxies. According to Newtonian dynamics one would expect that the rotation velocity decreases with higher radii. Rubin showed that the velocity does not decrease, but stays constant.
Calculating the force balance between centrifugal force F_c of a mass M and velocity v outside a galactic core with the gravitational force F_G leads to

$$F_{G,out} = \frac{G_N M m}{r^2} = \frac{mv^2}{r} = F_C \tag{2.1}$$

$$\Rightarrow \qquad v^2 = \frac{GM}{r} \tag{2.2}$$

$$\Rightarrow \qquad v \propto \frac{1}{\sqrt{r}} \tag{2.3}$$

Hence the orbital velocity of stars within a galaxy or galaxies within a cluster should decrease with distance. This is not observed in almost all galaxies.
Figure 2.1 shows the rotation curve of the galaxy NGC 6503. The dashed and dotted curves are the contribution to the rotational velocity due to the observed disk and gas, respectively. The dot-dashed curve represents the assumed contribution of Dark Matter forming a halo around the galaxy.

---

[1] No electromagnetic interaction

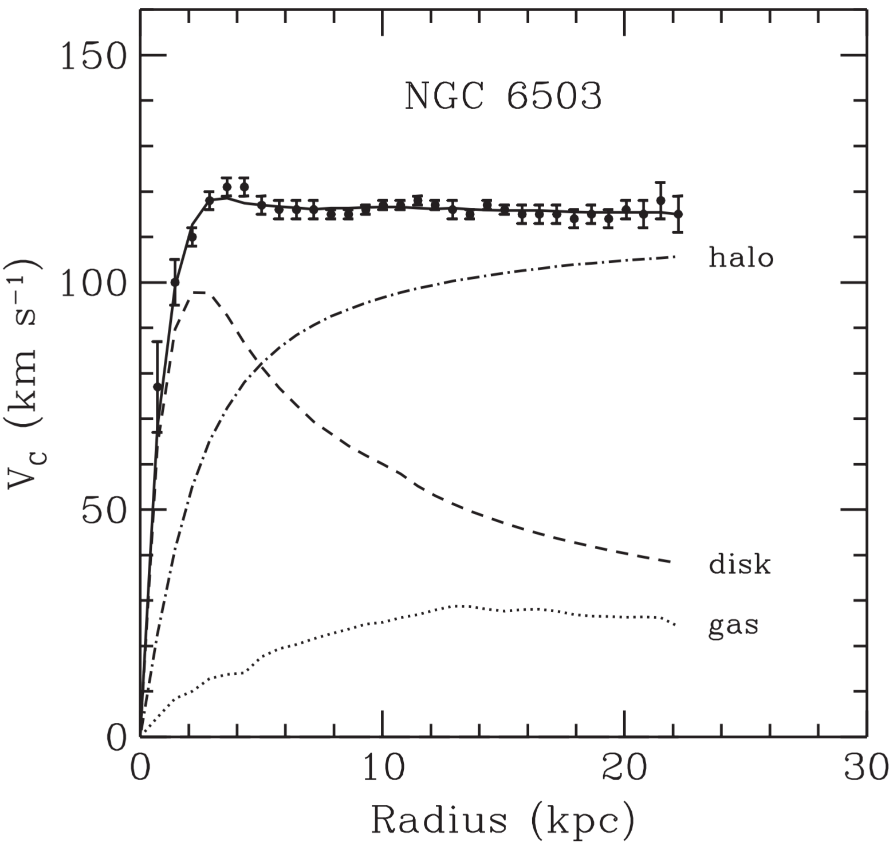

Figure 2.1.: *Rotation curve of the spiral galaxy NGC 6503. The points correspond to the measured data for the circular rotation velocities as a function of distance from the galactic center. It can be seen that the rotational velocity stays constant over long distances. Rotational velocity of the disk of the galaxy and the interstellar gas are expressed by dashed and dotted lines, respectively. The expected Dark Matter halo is expressed by the dod-dashed line [Beg91].*

Today rotation curves are obtained by measuring the Doppler effect of the 21 cm hyperfine transition line of hydrogen [Mul57]. As the extension and the structure of the Dark Matter halo is so far unknown it is difficult to determine the absolute amount of Dark Matter, especially within our Milky Way.

One technique in order to obtain masses of galaxy clusters is an application of the *Virial theorem* for an universal attractive potential $V(r) \propto r^n$, which was already used by Zwicky in 1933. According to Newtonian dynamics gravitational potentials are homogeneous of grade $m = -1$

$$2\langle T\rangle - m\langle V\rangle = 0 \tag{2.4}$$

where $\langle T\rangle$ and $\langle V\rangle$ are the average of kinetic and potential energy in time, respectively [Nol06].

Some theories propose a modification of Newtonian dynamics in order to solve the discrepancy of rotation curves [San02]. However, these *MOND*[2] theories fail to explain gravitational effects on scales of galaxy clusters and beyond.

---

[2] Modified Newtonian Dynamics

2.1.2. Gravitational Lensing

According to Einstein's theory of general relativity matter curves space-time. Therefore photons, which have no rest mass propagate along geodesics and are consequently effected by gravity [Ein36]. This effect can be detected by observing objects which have another massive object such as a galaxy in the line of sight. The gravitational field of the object in between acts as a cosmic lens for the light beams and the source appears brighter. This effect is called *micro lensing*.

As a special case multiple images of the observed object arranged in a ring can be observed. These rings are named *Einstein rings* and the effect is referred to as *strong lensing*.

In case the massive object is not directly in the line of sight, its gravitational effects can lead to *weak lensing*, causing the observed image to be distorted.

By measuring the deflection of light, the mass causing the lensing effect by its gravitational potential can be investigated. The obtained values disagree with the observed masses of luminous matter measurement by x-ray spectroscopy as there is not enough luminous matter in order to account for the observed gravitational effects. This discrepancy could be explained by the presence of Dark Matter.

2.1.3. The Bullet Cluster

The Bullet cluster (1E 0657-558) is the name of two galaxy clusters which collided in the past. In general one expects the stars of each galaxy, which are assumed to be point-like objects only interacting by gravity, to pass each other without collision. The gas of each galaxy interacts electromagnetically and slows down due to friction. As the matter distribution of a galaxy is dominated by its gas, the gravitational center of the total cluster should concentrate at the slowed down gas.

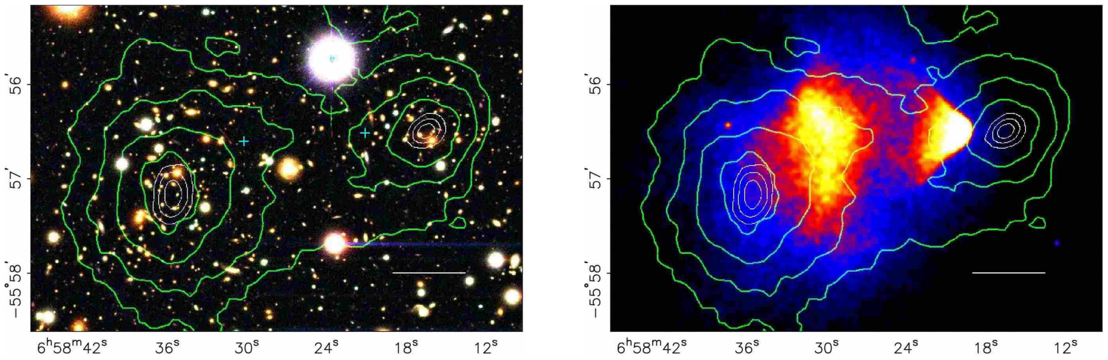

Figure 2.2.: *Image of two colliding clusters 1E0657-558. A distance of 200 kpc is indicated by a white bar. Gravitational potentials of both galaxies determined by weak lensing measurements are shown as green lines. The stars and the slowed down interstellar gas are shown in blue and red, respectively [Clo06].*

Figure 2.2 shows the gravitational potential, indicated by green lines, measured by weak gravitational lensing centered around the stars. The presence of Dark Matter is able to explain this paradox. Dark Matter covers most of the mass of the galaxies and passes the collision without slowing down, as it only interacts weakly [Clo06].

It is worth noting, that this effect cannot be explained by theories of Modified Newtonian Dynamics [Clo06].

2.1.4. The cosmic microwave background radiation

In 1965 PENZIAS and WILSON inadvertently discovered the *cosmic microwave background radiation* (CMB) [Pen65], which had been predicted by GAMOW, ALPHER and HERMAN in connection with Big Bang nucleosynthesis [Gam48] [Alp49]. The CMB is a thermal relic from the *Big Bang*, originating from photons decoupled from baryonic matter in the early universe 380,000 years after the Big Bang.

Before radiation and matter were in thermal equilibrium. Neutral atoms and molecules such as hydrogen or helium could not form due to dissociation by interactions with high energetic photons. Because of the expansion of the universe, temperature and energy density decreased. 380,000 years after the Big Bang at a temperature of $T \approx 3000$ K protons and electrons combined, producing neutral hydrogen[3].

In the neutral medium the mean free path of the photons became large. Photons did not interact with matter due to Thompson scattering any more and decoupled from matter. The universe became transparent.

Because of the expansion of space-time the wavelength of the photons is red-shifted until their wavelength reaches the microwave region observed nowadays. As photons and matter were in thermal equilibrium before decoupling, the temperature of the CMB is highly isotropic with fluctuations on the $\frac{\delta T}{T} \sim 10^{-5}$ scale only, following a black body spectrum of (2.725±0.001) Kelvin [Fix96].

The first precise measurement of the energy distribution of the CMB radiation was performed by the COBE[4] satellite in 1992, confirming a Planck distribution shown in figure 2.3.

Moreover, COBE detected a dipole anisotropy of the order of $\sim 10^{-3}$ caused by the motion of the solar system[5] towards the constellation Crater with $v = 371\,\frac{\mathrm{km}}{\mathrm{s}}$.

As fluctuations in temperature in general correspond to energy density fluctuations which are assumed to be seeds of structure formation in the universe, these anisotropies have been studied in more detail by COBE and especially by its successor, the WMAP[6] satellite, and nowadays by PLANCK.

Figure 2.4 shows a temperature sky map taken by the WMAP satellite.

In order to analyze CMB anisotropies, temperature fluctuations are studied as a function of direction by expanding $T(\theta,\phi)$ as spherical harmonics Y_{lm}, where θ and ϕ are spherical coordinates [Gru05].

$$T(\theta,\phi) = \sum_{l=0}^{\infty} \sum_{m=-l}^{+l} a_{lm} Y_{lm}(\theta,\phi) \tag{2.5}$$

Terms of large l correspond to structures at small angular scales and vice versa. The amplitude of regular variation with angle is defined by the coefficients a_{lm}

$$C_l = \frac{1}{2l+1} \sum_{m=-l}^{l} |a_{lm}|^2 \tag{2.6}$$

The set of C_l as a function of multipole moments l leads to the angular power spectrum shown in figure 2.5, while C_l represents the amount of structure at a certain angular scale.

---

[3] The first ionization energy of hydrogen is at $E = 13.6$ eV, which corresponds to a temperature of $T = 160{,}000\ \mathrm{K} \gg 3000$ K. Recombination at these temperatures was suppressed because of the small baryon to photon ratio $\eta \approx 5 \cdot 10^{-10}$ [Gru05].

[4] Cosmic Background Explorer

[5] The CMB is assumed to be isotropic with respect to the rest frame of the universe [Gru05].

[6] Wilkinson Microwave Anisotropy Probe

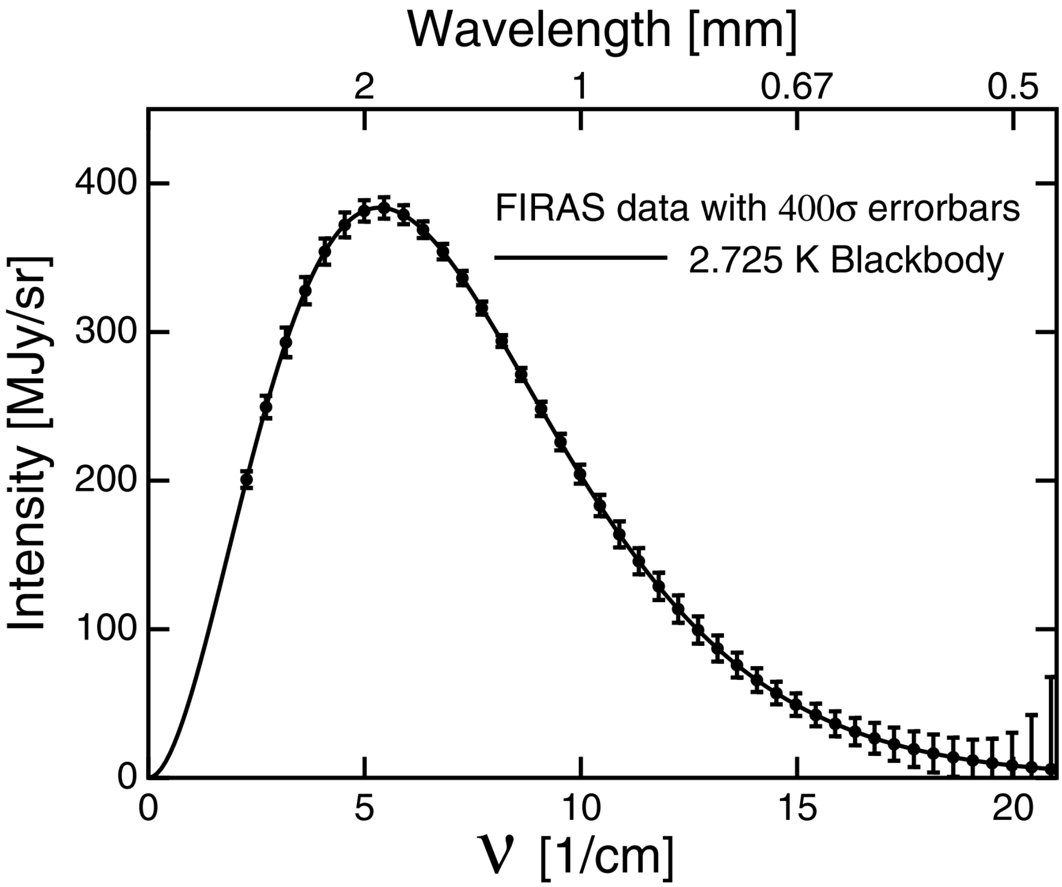

Figure 2.3.: *Spectrum of the CMB measured by COBE in 1992 showing a black body profile at a temperature of 2.725 K according to Planck's law. The error bars are enlarged by a factor of 400 [Fix96].*

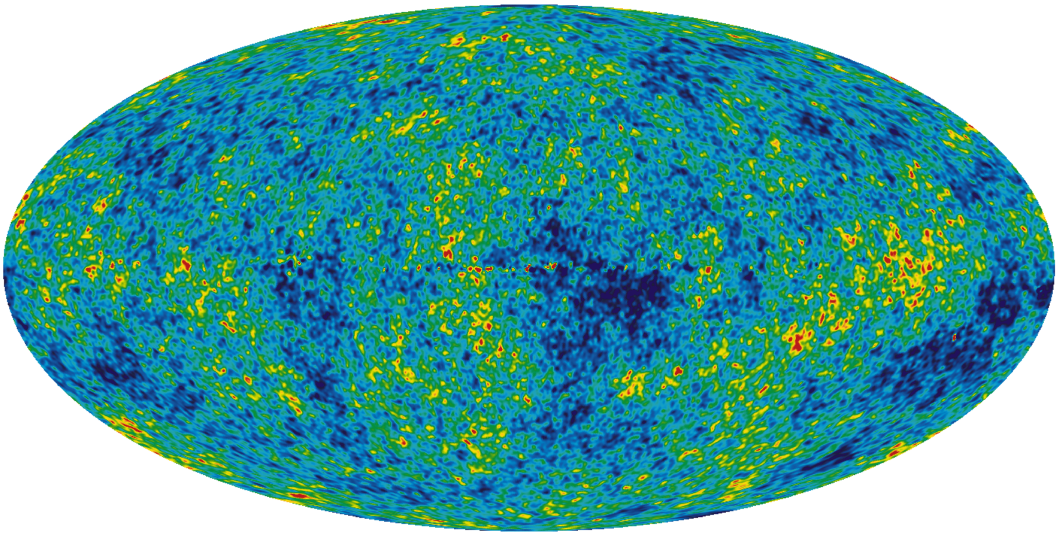

Figure 2.4.: *Foreground-reduced sky map of the infant universe based on five years of WMAP data. The color differences correspond to temperature fluctuations of a range of* ±200 *μK originating of a timescale 380.000 years after the Big Bang [Hin09]. Red colors correspond to hotter regions, while colder regions are indicated in blue colors.*

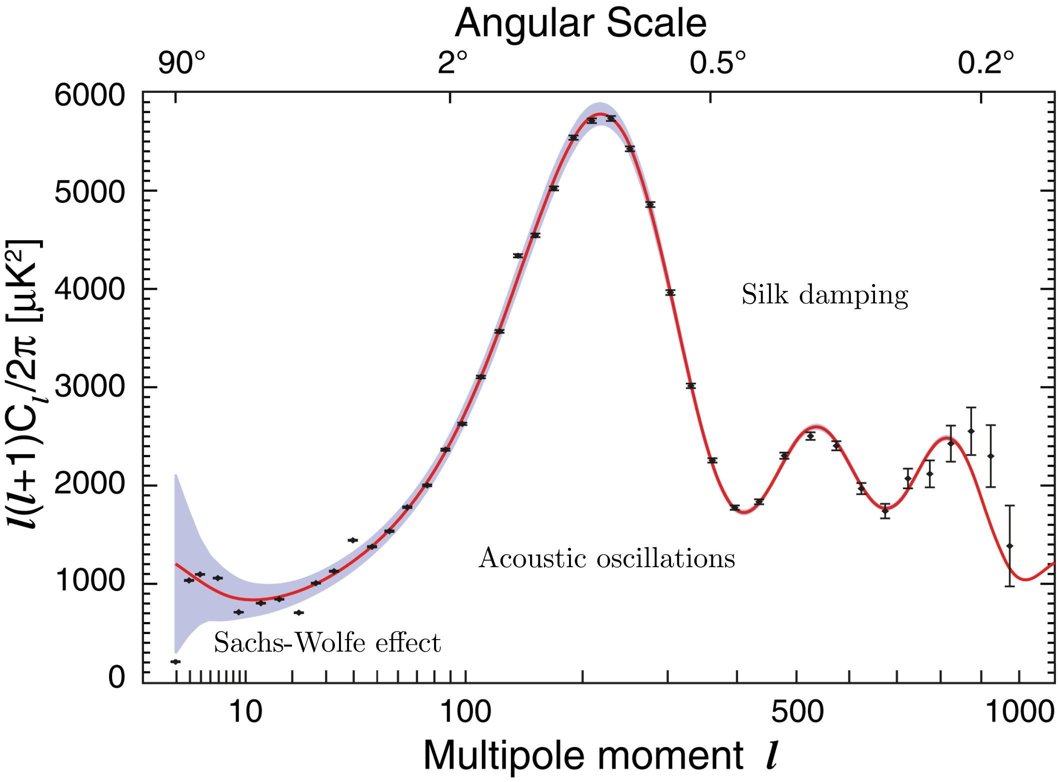

Figure 2.5.: *Temperature fluctuations in terms of multipole moment l and angular scale measured by WMAP with the best-fit by the ΛCDM model. The ratio between the first and the second peak corresponds to the ratio of baryons and the total amount of matter besides Dark Energy. The overall mass density of the universe including Dark Energy can be obtained by considering all fluctuation peaks. At high angular scales the Sachs-Wolfe-Effect is dominating. Acoustic oscillations and Silk damping can be seen at smaller angles [Hin09].*

Acoustic oscillations

Density fluctuations in the early universe cause gravitational potentials where matter is accumulated. Due to the high densities, matter is heated and radiates photons while the plasma expands. Because of the expansion the system cools down, producing less radiation. Therefore gravity becomes dominant over radiation pressure and accretion of matter starts again, leading to longitudinal acoustic oscillations. At the time of recombination the photons decouple from matter and the CMB gives a fingerprint of the previous acoustic oscillations which can be identified with the maxima in the angular power spectrum.

The ratio between the first and the second peak corresponds to the ratio of baryons Ω_B and the total amount of matter $\Omega_M = \Omega_B + \Omega_{DM}$. The overall density of the universe including Dark Energy Ω_Λ can be obtained by considering all fluctuation peaks.

Furthermore, the position of the first acoustic peak is related to the total energy density Ω_{tot}:

$$l \approx \frac{200}{\sqrt{\Omega_{\text{tot}}}} \qquad \text{[Hu02]} \tag{2.7}$$

The overall peak structure of the angular power spectrum depends on many cosmological parameters, among others on the total energy density Ω_{tot}, the energy density of matter Ω_M, baryons Ω_B and vacuum energy Ω_Λ, the Hubble constant H_0 and the baryon to photon ratio η.

Table 2.1 lists the parameters which are of major interest concerning the matter composition in the universe determined by WMAP.

Parameter	Value	Uncertainty
Ω_{tot}	1.02	±0.02
Ω_M	0.27	±0.04
Ω_B	0.044	±0.004
Ω_Λ	0.73	±0.04

Table 2.1.: *Matter composition of the universe* $\Omega = \frac{\varrho}{\varrho_c}$, *where* $\varrho_c = 1.88h^2 \cdot 10^{-29}\frac{g}{cm^3}$ *is the critical density determined by the WMAP experiment after five years of taking data [Cer02].*

Sachs-Wolfe effect

Matter density fluctuation at the time of recombination cause temperature fluctuations of the CMB. On high angular scales fluctuations are predominantly caused by the *Sachs-Wolfe effect*.

Photons passing gravitational potentials, which arise from density fluctuations are blue-shifted while entering the potential and red-shifted while leaving the potential. From the first maximum of the angular power spectrum at $l \approx 200$ one obtains $k = 0$ (flat universe) and $\Omega_{tot} = 1.02 \pm 0.02$.

As the universe is expanding the gravitational potentials are slightly flattened out. Therefore some photons are more blue- than red-shifted [Ho08]. Temperature fluctuations arising from this effect provide a fingerprint of the over-densities at the time of recombination and give rise to a direct evidence for Dark Energy [Scr03].

Silk damping

Maxima of higher orders are suppressed by *Silk damping*[7] [Sil68]. Smaller matter over-densities are suppressed by scattering photons. This leads to damping of density fluctuations on small scales. Evidence of this can be seen in the angular power spectrum as peaks at higher l have a reduced amplitude. The damping scale depends on the amount of baryons in the universe [Dur01].

---

[7] Sometimes referred to as *diffusion damping*.

2.2. Properties of Dark Matter

Most theories require Dark Matter not to absorb, emit or scatter electromagnetic radiation at any wavelength. From the WMAP results discussed in section 2.1.4 it is known that most of the Dark Matter is non-baryonic. However, there might also be some contribution from ordinary matter as well.

Dark Matter is gravitationally self-attractive and clumps with ordinary matter, providing a reasonable theoretical construct for structure formation of the universe [Ost03]. Most theories about structure formation of galaxies and clusters of galaxies require Dark Matter particles to propagate at non-relativistic velocities. Accordingly possible Dark Matter candidates have been subdivided into three classes:

i) **Hot Dark Matter**
Hot Dark Matter (HDM) propagates at ultra-relativistic speed. So far neutrinos are known to contribute to this type of Dark Matter (section 2.3). HDM made of neutrinos travels too fast in order to be gravitationally bound by galaxies or clusters of galaxies. Therefore most HDM scenarios are ruled out due to observations of structure formation [Whi83].

ii) **Warm Dark Matter**
Warm Dark Matter (WDM) travels at relativistic velocities. Therefore WDM retards the beginning of structure formation until it is sufficiently cooled down due to the expansion of the universe to cluster gravitationally. As a consequence structure formation on small-scales is suppressed and a *top-down scenario*[8] is favored, assuming structure formation to be caused by WDM [Aba11].

iii) **Cold Dark Matter**
Dark Matter has to be cold, than is non-relativistic in order to be able to clump due to gravitational forces at the time, when structure formation in the early universe started. Numerical N-body simulations of structure formation agree with most of the observed structures predicted by cold Dark Matter (CDM) [Ost03].

Dark Matter is assumed to be long-lived or stable with respect to the age of the universe [Ost03].

The interaction cross-section between Dark Matter particles itself and with ordinary matter has to be small, as it is assumed to move without collisions.

---

[8] Top-down structure formation in the universe implies that big structures have been created first [Ber04].

2.3. Candidates for Dark Matter

A great number of possible candidates offering the described features have been proposed. Without claiming completeness the most probable ones are discussed.

Neutrinos

Results from neutrino oscillation experiments have shown that neutrinos have a non-zero rest mass and therefore make up a contribution in the form of hot Dark Matter.

An upper limit for the electron anti-neutrino mass was given by the Troitsk and Mainz Neutrino Mass Experiment of

$$m_{\bar{\nu}_e} < 2.1\,\mathrm{eV} \qquad (95\,\%\,\mathrm{C.L.}) \qquad [\mathrm{Lob03}] \tag{2.8}$$

and

$$m_{\bar{\nu}_e} < 2.3\,\mathrm{eV} \qquad (95\,\%\,\mathrm{C.L.}) \qquad [\mathrm{Kra05}], \tag{2.9}$$

respectively.

The mass differences of the three mass eigenstates have to be small in order to agree with observations of atmospheric and solar neutrino deficits[9]. Therefore the upper limits given in equations 2.8 and 2.9 can be applied to all three neutrino flavours. The relic neutrino density is about

$$\Omega_\nu h^2 \lesssim 0.07 \qquad [\mathrm{Ber04}]. \tag{2.10}$$

Therefore neutrinos only make up a small part of the overall Dark Matter distribution. Although neutrinos are too light to be cosmologically significant, sterile neutrinos remain possible. Sterile neutrinos are hypothetical particles similar to neutrinos, but without Standard Model weak interaction short of mixing [Ber04].

MACHO's

Even though most of the Dark Matter contribution is assumed to be non-baryonic, experiments search for non-luminous ordinary matter in form of Massive Astrophysical Compact Halo Objects (MACHO) as well. MACHOs are assumed to be stellar remnants such as white and brown dwarfs, neutron stars or black holes. These objects have been investigated using the technique of gravitational micro lensing previously mentioned in section 2.1.2. It was discovered that at most 20 % of the Dark Matter content is composed of stellar remnants [Fre00].

Axions

Axions are light neutral particles with a mass of $10^{-6} - 10^{-3}$ eV arising from solving the problem of strong CP violation[10].

Axions are assumed not to be in thermal equilibrium in the early universe, as they only consist of marginal weak coupling [Ber04]. Therefore their relic abundance is hard to determine. They are expected to form cold Bose condensates immediately, which permeate the entire universe [Ost03].

As axions are expected to have only a marginal rest mass, a huge number of particles is necessary in order to significantly contribute to the Dark Matter distribution.

Most of the parameter space for axions is already ruled out [Jim11].

---

[9] $\Delta m^2_{sol} \approx 4 \cdot 10^{-5}$ eV^2 and $\Delta m^2_{atm} \approx 3 \cdot 10^{-3}$ eV^2 [Bea02]

[10] The expected mass rage of $10^{-6} - 10^{-3}$ eV arises from the Peccei-Quinn solution for the problem of strong CP violation in strong interaction [Fre00].

WIMP's

Weakly Interacting Massive Particles (WIMP) are well motivated by a supersymmetric extension of the Standard Model of particle physics discussed in section 2.4, giving rise to a natural Dark Matter candidate [Jun96].

WIMPs fulfill all expected features of Dark Matter. In particular, they are classified as cold Dark Matter and consistent with large-scale structure formation observed today [Ost03].

Moreover, WIMPs naturally show the required relic abundance of 20 − 30 %. As they only interact weakly[11], thermal equilibrium appears within 10^{-12} seconds after the Big Bang [Ost03]. Assuming a WIMP mass $m_\chi \in$ [100 GeV ; 10 TeV] annihilation stops at a temperature of $T_f \sim \frac{m_\chi}{20}$, which is consistent to 1 ns after the Big Bang as mentioned before [Jun96]. Because of the expansion of the universe, WIMPs fall out of equilibrium, with a density that is determined by their annihilation cross-section $\sigma_{\mathrm{ann}}^{\mathrm{weak}}$. The thermally averaged cross section of WIMPs at the time of freezing out is $\langle \sigma v \rangle \approx 3{\cdot}10^{-26}\,\frac{\mathrm{cm}^3}{\mathrm{s}}$, leading to a relic Dark Matter abundance consistent with 20 − 30 % [Jun96].

The relic density is

$$\Omega_{\mathrm{DM}} h^2 = \frac{3 \cdot 10^{-27} cm^3}{\langle \sigma_{ann}^{weak} v \rangle} \qquad \text{[Fre06]} \tag{2.11}$$

with

$$h = \frac{H_0}{100\,\frac{\mathrm{km}}{\mathrm{s\ Mpc}}} = 0.72 \pm 0.03 \qquad \text{[Par10]} \tag{2.12}$$

2.4. The Standard Model and supersymmetry (SUSY)

The Standard Model of particle physics describes the constituents of matter by 12 fermions (quarks and leptons) and the electromagnetic, weak and strong interaction mediated between them by 12 gauge bosons (γ, Z^0, $W^\pm$ and g_8). It successfully predicted many experimental observations for many years. Although some problems such as understanding the fundamental difference between bosons and fermions, the hierarchy problem[12] and the unification of forces within a grand unified theory (GUT) at high energy scales ($\sim 10^{16}$ GeV) remain unsolved [Jun96].

In order to address these discrepancies several extensions of the Standard Model have been proposed, among others a new symmetry called *supersymmetry* (SUSY) has been introduced. SUSY creates a super-partner for each particle of the Standard Model called *sparticle*. Each boson is associated with a super-symmetric fermion partner (sfermion) and each fermion is associated with a super-symmetric boson partner (sboson). Figure 2.6 shows all particles from the Standard Model and their corresponding super-partners. As none of these sparticles has been observed in collider experiments so far they have to have higher masses compared to their super-partners [Ber04]. Therefore SUSY must be spontaneously broken at high temperatures in the early universe [Ost03].

As SUSY creates 105 additional free parameters [Jun96], simplifying assumptions have been made, giving rise to a minimal super-symmetric model (MSSM), which creates only 5 new parameters. In most cases the MSSM requires conservation of R-parity, a new multiplicative quantum number related to the baryon and lepton number operators B

---

[11] In this case weakly interacting refers to a low interaction probability. Interactions can be mediated due to the weak force, but do not have to.

[12] The hierarchy problem origins from radiative corrections to the mass of the Higgs boson, causing differences between the electroweak and Planck energy scales [Ber04].

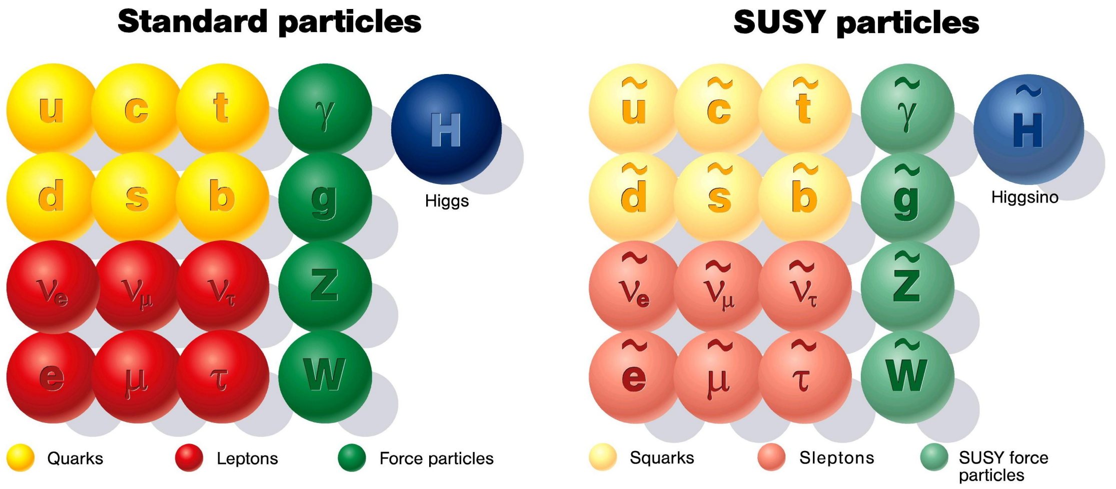

Figure 2.6.: *Standard Model particles (left) and their corresponding super-partners (right) [Des05].*

and L and the spin s. R-parity is needed in order to suppress the proton decay [Smi96].

$$R = (-1)^{3B+L+2s} \tag{2.13}$$

For particles R-parity is $+\mathbf{1}$ and for super-particles $-\mathbf{1}$. As a consequence of R-parity sparticles can only decay into an odd number of sparticles. Therefore the *lightest supersymmetric particle* (LSP) cannot decay and is stable [Jun96]. The LSP gives rise to a natural Dark Matter candidate, namely the *neutralino* χ, which has about the right relic abundance. A likely candidate for the neutralino would be a WIMP.
In the MSSM $\tilde{B}$, $\tilde{W}_3$ and $\tilde{H}^0_{1,2}$ mix into four Majorana mass eigenstates $\tilde{\chi}^0_1$,$\tilde{\chi}^0_2$, $\tilde{\chi}^0_3$ and $\tilde{\chi}^0_4$, the neutralinos. The lightest of these sparticles χ has to be stable as predicted by R-parity.

$$\chi = a\tilde{B} + b\tilde{W}_3 + c\tilde{H}^0_1 + d\tilde{H}^0_2 \tag{2.14}$$

where $a^2 + b^2$ and $c^2 + d^2$ are the gaugino and higgisino fraction, respectively [Ber04].

2.5. Experimental detection

Dark Matter is being investigated by direct and indirect detection methods as well as creation experiments using colliders. Especially the Large Hadron Collider (LHC) aims at creating super-symmetric particles and detecting them by the *missing mass* method in order to constrain supersymmetry.
At the moment WIMPs are the most favored Dark Matter candidates. Therefore both their direct and indirect detection is discussed in detail.

2.5.1. Indirect detection

Neutralinos are assumed to be *Majorana particles*[13] [Jun96]. Indirect detection methods therefore search for products of WIMP annihilation ($e^{\pm}, p, \bar{p}, \gamma, \nu, \bar{\nu}$) by observing high energy cosmic rays.

---

[13] Majorana particles or Majorana fermions are their own anti-particles.

As for annihilation processes a meeting of two WIMPs is required, dense regions inside the Sun [Sil85] or the Earth [Kra89] which accrete WIMPs due to their gravitational potential are favored as probable interaction regions. The annihilation rate R is therefore scaling with the square of the Dark Matter density $R \propto \varrho_\chi^2$ [Ber04]. In contrast to gamma-rays, neutrinos arising from annihilation processes in the sun are able to escape from this dense region. They are distinguishable from solar neutrinos as their energy is expected to be about one third of the WIMP mass and is therefore much higher than the energy of solar neutrinos [Jun96]. The IceCube detector[14] is able to investigate annihilation neutrinos from the sun. 100 GeV neutrinos arising from the sun would be a strong evidence for Dark Matter annihilation processes.

2.5.2. Direct detection

Detecting WIMPs via scattering of atomic nuclei and measuring the induced nuclear recoil signals is the only method in order to detect WIMPs directly.

Two modes of interaction during WIMP scattering have been proposed. On the one hand WIMPs can couple to the spin of a target nucleus (spin-dependent) or on the other hand couple coherently to the nucleus (spin-independent) [Bro10]. The induced nuclear recoil on the target atom gives rise to three measurable signals:

i) **Heat**
WIMP scattering creates phonons within the target material. A marginal change in temperature can be measured by cooling the target down to the milli Kelvin range as the heat capacity c_V varies with T^3 at low temperatures [Kit06].

$$c_V(T) = 3Nk_B \left[3\left(\frac{T}{\Theta_D}\right)^3 \int\limits_0^{\frac{\theta_D}{T}} \frac{x^4 e^x}{(e^x-1)^2}\,dx \right] \quad ; \quad \Theta_D = \frac{\hbar\omega_D}{k_B} \tag{2.15}$$

$$\sim \left(\frac{T}{\Theta_D}\right)^3 \tag{2.16}$$

where the Debye temperature Θ_D and the Debye frequence ω_D depend on the used target material.

ii) **Charge**
WIMP scattering causes ionization of the target nucleus. The created electrons can be measured.

iii) **Light**
WIMP scattering also causes scintillation light, which can be detected with photo sensitive detectors.

Measuring two of these signals simultaneously allows for background discrimination. However, various experiments exist which only use one of these detection channels in order to detect WIMPs.

---

[14] The IceCube Neutrino Observatory is a neutrino telescope located at the south pole.

Interaction rate

The event rate per detector mass and recoil energy can be derived from the cross-section for WIMP-nucleus scattering considering the density of the Dark Matter halo ϱ_χ and its velocity distribution.

$$\frac{dR}{dE} = \frac{\varrho_\chi \sigma F^2(q)}{2m\mu^2} \int\limits_{v>\sqrt{\frac{ME}{2\mu^2}}} \frac{f(v,t)}{v}\, d^3v \qquad \text{[Fre06]} \tag{2.17}$$

where f(v,t) is the WIMP velocity distribution, μ the reduced mass of the wimp-nucleus system and F(q) the nuclear form factor.

The cross-section σ depends on the interaction mode.

$$\sigma = \begin{cases} \frac{A^2\mu^2}{\mu_p^2}\sigma_p \quad \sim A^2 & \text{Spin-independent} \\ \\ \frac{4\mu^2}{\pi}\left|\langle S_p\rangle G_p + \langle S_n\rangle G_n\right|^2 & \text{Spin-dependent} \end{cases} \qquad \text{[Fre06]} \tag{2.18}$$

Therefore spin-independent interactions are enhanced by the atomic number of the target material squared, whereas spin-dependent interactions are addicted to the spin content of the nucleus. The limits on WIMP cross-sections both for spin-dependent and spin-independent interactions as a function of mass are presented in figure 2.9.

2.6. The DAMA/LIBRA case

The DAMA/LIBRA and DAMA/NaI experiments search for an annual modulation signature of Dark Matter due to the motion of the Earth around the Sun which should cause a variation in the interaction rate of Dark Matter particles. The annual modulation signal detected by PMT looking for scintillation light in thallium-doped sodium iodide crystals NaI(Tl) could be interpreted as a Dark Matter signal [Ber08]. So far no background has been found which could explain the annual modulation signal shown in figure 2.7.

The combined results from DAMA/LIBRA and DAMA/NaI comprising a total exposure of 0.82 ton×years allow them to claim a Dark Matter discovery with an 8.2 sigma C.L. in the annual modulation signals, which is presently discussed controversially.

Indeed, the results from the DAMA experiment are in conflict with other experiments such as CDMS or XENON which have not seen a Dark Matter signal although they have a much higher sensitivity. A probable explanation would be that one of the many sources of experimental backgrounds has been underestimated or overlooked and is the direct cause for the observed annual modulation. The claimed Dark Matter region from DAMA as well as the limits claimed by other experiments are visible in figure 2.8.

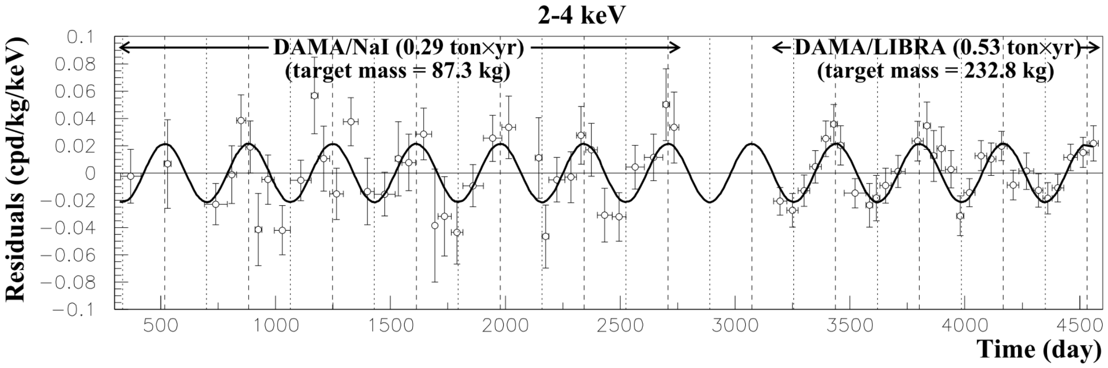

Figure 2.7.: *Model-independent residual rate of single-hit scintillation events in the 2-4 keV energy interval recorded by the DAMA/LIBRA experiment. The superimposed cosinusoidal function shows the expected annual modulation due to the motion of the Earth around the Sun. The dashed and dotted vertical lines indicate the maximum (June 2^{nd}) and the minimum of the signal, respectively [Ber08].*

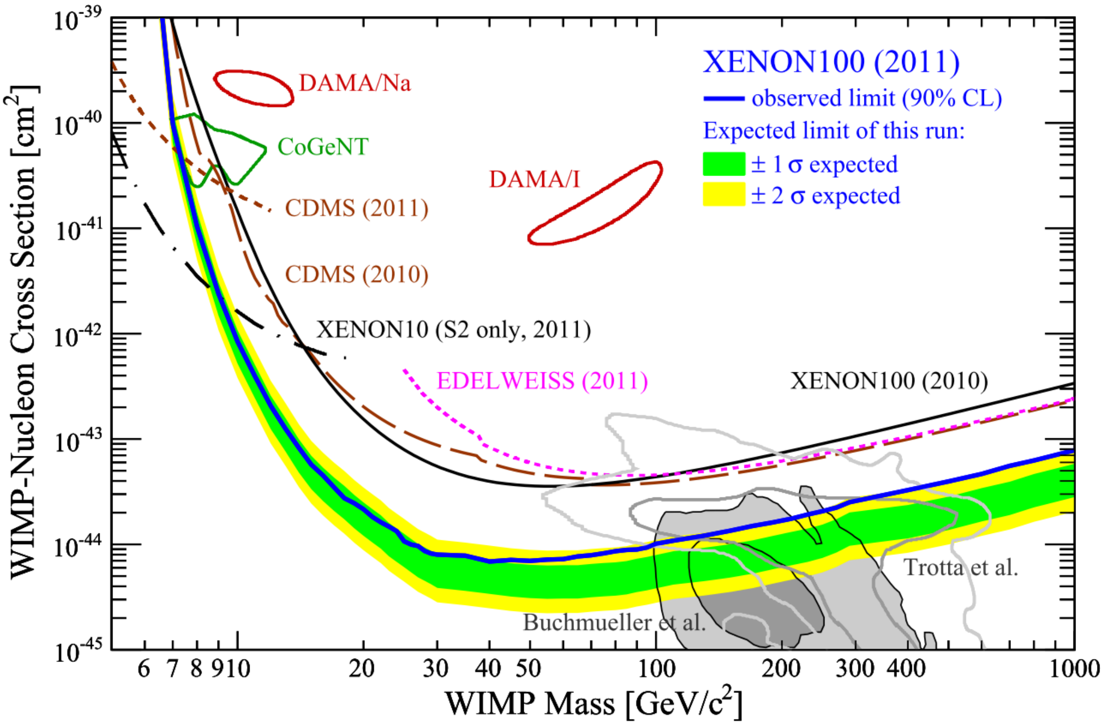

Figure 2.8.: *Limits on spin-independent elastic WIMP-nucleon cross-section as a function of WIMP mass obtained by the XENON10, XENON100, EDELWEISS and CDMS experiments. Moreover, the claimed Dark Matter regions of DAMA and CoGeNT are shown. The regions shaded and contoured in gray show the expected phase space at at 68 % and 95 % C.L. obtained by Buchmueller et al. and Trotta et al., respectively [Apr11a].*

2.7. Conclusion

There is overwhelming evidence for the existence of non-baryonic Dark Matter on galactic and intergalactic scales.

The most powerful arguments for Dark Matter are given by rotation curves of galaxies and the results from WMAP, which unlike theories of modified Newtonian dynamics can explain rotation curves on the scale of both galaxies and galaxy clusters.

Furthermore structure formation of the universe can only be explained by an abundance of Dark Matter of $20-25$ %.

Weakly interacting massive particles are highly favored to be one of the dominant contributions to Dark Matter, however, a detection of WIMPs would not totally rule out other possible candidates [Ost03]. WIMPs naturally arise from supersymmetry, in particular from minimal supersymmetric models. Their properties fit the characteristics of cold Dark Matter claimed by predictions of structure formation in the early universe.

In the past, different experiments like DAMA [Ber08] have claimed Dark Matter detection. However, their results are constrained by other experiments and therefore have to be confirmed independently.

It is possible that Dark Matter is composed of more than one species. Neutrinos, for example, are already known as a contribution to hot Dark Matter. Moreover, Dark Matter on different galactic scales may comprise different origins [Jun96].

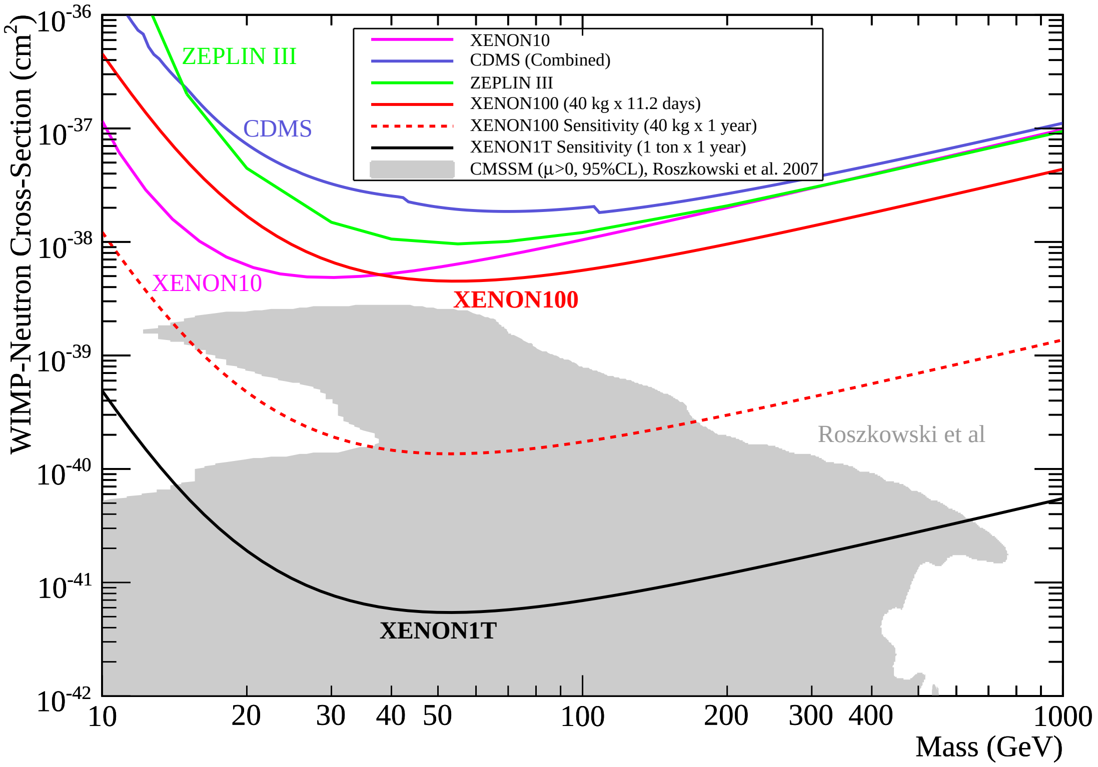

(a) Spin-dependent cross-sections versus WIMP mass

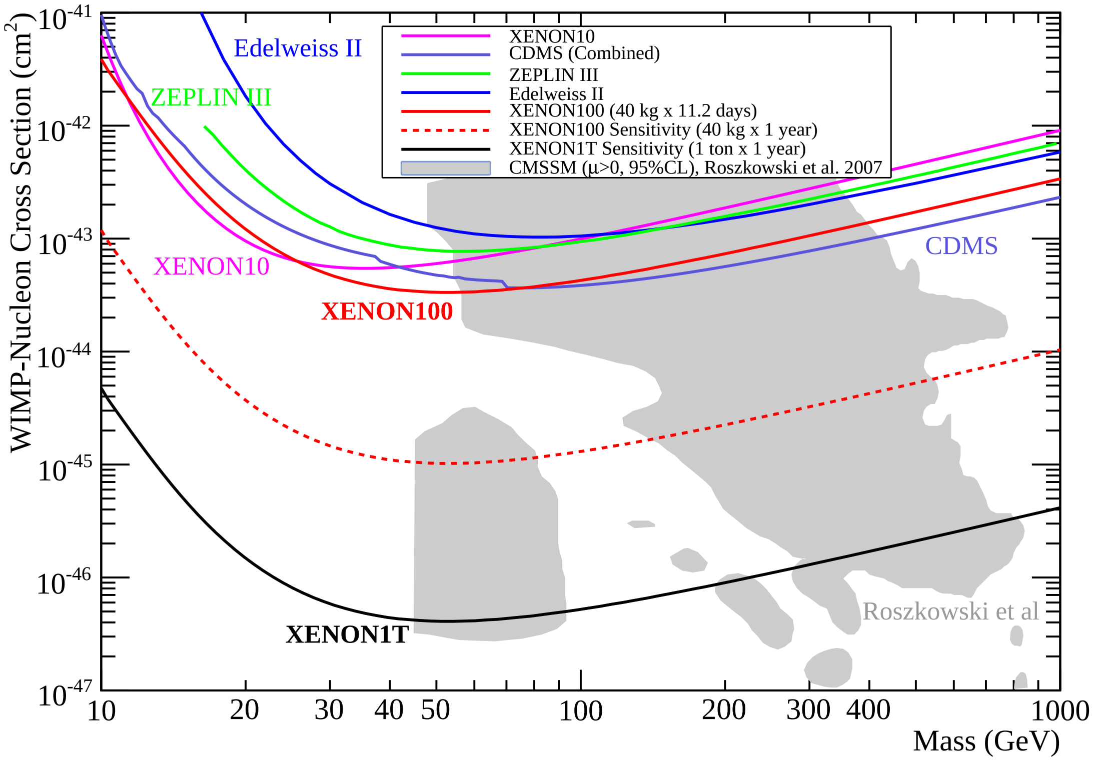

(b) Spin-independent cross-sections versus WIMP mass

Figure 2.9.: *Exclusion limits on WIMP cross-sections versus mass both for spin-dependent and spin-independent interactions obtained by the CDMS, EDELWEISS, XENON and ZEPLIN experiments. The shaded region corresponds to the expected phase space for WIMP Dark Matter predicted by Roszkowski et al. [Apr10a].*

3. The XENON Dark Matter Project

The XENON Dark Matter Project started in 2005 with the XENON10 experiment. Its name refers to the amount of target material of 10 kg of xenon. In 2007 a limit on the cross-section for spin-independent WIMP-nucleus interactions was claimed to

$$\sigma_{SI} = 5.2 \cdot 10^{-44}\ \mathrm{cm}^2 \qquad \text{and} \qquad \sigma_{SI} = 10.4 \cdot 10^{-44}\ \mathrm{cm}^2$$

for WIMPs with a mass of 30 $\frac{\mathrm{GeV}}{c^2}$ and 100$\frac{\mathrm{GeV}}{c^2}$, respectively [Ang08]. At that time this was the first use of a liquid noble gas detector and it provided the best limit in the world. In the following year the next generation detector XENON100 started operation in the underground Laboratori Nazionali del Gran Sasso (LNGS) and in 2011 improved the limit on the spin-independent WIMP-nucleus cross-section to

$$\sigma_{SI} = 7.0 \cdot 10^{-45}\ \mathrm{cm}^2$$

for a WIMP mass of 50 $\frac{\mathrm{GeV}}{c^2}$ at 90 % confidence level, which so far is the most stringent limit on Dark Matter cross-sections in the world [Apr11a].
In this chapter the XENON100 experiment, which is currently running is described in detail, as well as its successor XENON1T. In particular the issues of building a ton scale Dark Matter detector are discussed.

3.1. Liquid xenon detectors

The XENON experiment uses a two phase time projection chamber (TPC) in order to detect WIMPs. The principle of operation is described on the basis of the XENON100 detector, which is currently taking data.
The XENON100 detector is a two phase TPC with 165 kg of liquid xenon. The active target mass comprises about 62 kg [Apr11b].
Taking xenon as a target material has various advantages:

i) **Scalability**
As a liquid, xenon can be scaled at moderate costs easily.

ii) **High atomic number: Z=54**
The spin-independent WIMP cross-section is enhanced by $\sigma_{SI} \sim A^2$. Details have been discussed in chapter 2.

iii) **Even and odd isotopes**
As about 50 % of the xenon isotopes are of odd number, spin-dependent interactions can be studied as well.

iv) **Self-shielding**
Due to its high density in liquid phase of $\varrho_{\mathrm{lq}} = 3\,\frac{\mathrm{g}}{\mathrm{cm}^3}$ and its high atomic number, xenon can be used to shield against external gamma backgrounds, allowing fiducial volume cuts of the target [Apr10d].

v) **Good scintillator**
Scintillation photons of liquid xenon have a wavelength of $\lambda = 178$ nm and can be directly detected by PMTs without shifting the wavelength to an appropriate region.

vi) **Intrinsic purity**
Xenon has no other long-lived radioactive isotopes besides ^{124}Xe and ^{136}Xe, whose half-lives are so long, that they are usually not observed [Ber02].

The double beta decay candidate ^{136}Xe, for example, has a half life of

$$t_{\frac{1}{2}}(2\nu\beta\beta) = [2.11 \pm 0.04 \text{ (stat.)} \pm 0.21 \text{ (sys.)}] \cdot 10^{21}\, y \qquad \text{[Ack11]}.$$

vii) **Background discrimination**
Simultaneous measurements of charge and light signals enable discrimination between nuclear and electron recoil.

Besides all these advantages, the overall interaction rate R between WIMPs and xenon nuclei is substantial small. Compared with other target materials such as germanium or argon, xenon is especially favored at low recoil energies because of its high atomic number. Details of this are shown in figure 3.1.

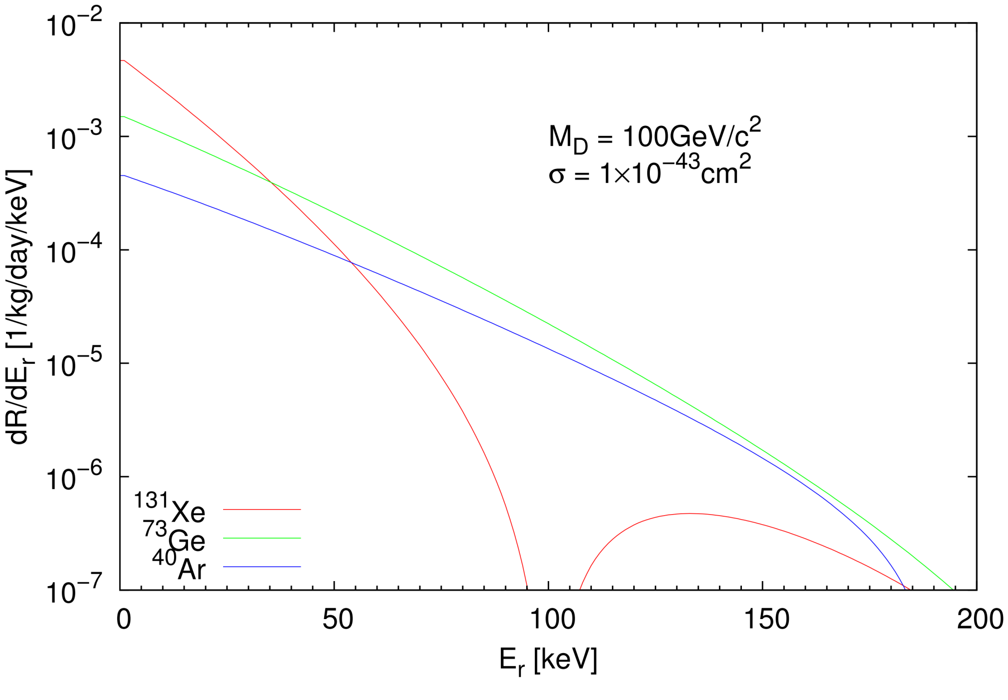

Figure 3.1.: *WIMP scattering rate* $\frac{dR}{dE}$ *as a function of recoil energy* E_r *for different target materials assuming a WIMP mass of* $m_\chi = 100\,\frac{GeV}{c^2}$ *and a scattering cross-section of* $\sigma = 1 \cdot 10^{-43}\, cm^2$ *[Mei11].*

According to the $\sigma \sim \mathrm{A}^2$ enhancement due to coherent scattering the interaction rate increases at low recoil energies, especially for heavy target materials such as xenon. In contrast the interaction rate decreases with increasing recoil energy, as the momentum transfer $q = \sqrt{2M_tE_r}$ causes the de-Broglie wavelength $\lambda = \frac{h}{q}$ of the incoming particles to reach the dimension of the target nucleus. This effect is taken into account by the nuclear form factor $F(q)$ in equation 2.17 which has strong influence on elements with high mass numbers, as the size of the nucleus is larger. Xenon is optimal for WIMP masses around $m_\chi \sim 100\,\frac{\mathrm{GeV}}{c^2}$.

Such low counting rates require a substantial low background. This issue is further discussed after a detailed description of the detection technique in section 3.3.

3.2. The two phase xenon time projection chamber

Interactions between WIMPs and target nuclei cause heat, ionization and scintillation signals, while only the ionization and scintillation signals are investigated in the XENON experiment. A schematic sketch of the detector is visible in figure 3.2.

WIMP detection is done by simultaneous measurements of ionization electrons and direct scintillation light at a wavelength of $\lambda = 178$ nm with a line width of 13 nm [Jor65]. This primary scintillation light, later referred to as a S1 signal, is produced after scattering events in liquid phase. It arises by de-excitation of excited diatomic xenon molecules[1] Xe_2^* into the ground state. This is of crucial importance, as the photons emerging from the excited state of the xenon molecule are not absorbed again by xenon atoms, as their energy does not correspond to the required excitation energy [Ozo05].

Electrons emerging from ionization processes in liquid phase are drifted to the top of the detector by an electric field $\mathcal{E}_\mathrm{d} \approx 1\,\frac{\mathrm{kV}}{\mathrm{cm}}$ between the cathode and the gate grid, which prevents them from recombining with the xenon ions.

At the phase boundary between liquid and gaseous xenon the electrons are extracted into the gaseous phase and accelerated by an electric field[2] $\mathcal{E}_\mathrm{e} \approx 10\frac{\mathrm{kV}}{\mathrm{cm}}$ causing fluorescence light by interactions with the xenon gas, named S2 signals. The number of secondary photons N_γ is proportional to the number of electrons originating from the ionization process and is therefore proportional to the energy deposited in the liquid phase by incoming particles

$$N_\gamma = \alpha N_e \left(\frac{\varepsilon_e}{p} - \beta \right) px \qquad \text{[Apr11e]}, \tag{3.1}$$

where p is the pressure and x the drift length of the electron in gaseous phase which determines the width of the S2 signal. N_e is the number of extracted electrons and N_γ the number of proportional scintillation photons. α and β are material factors corresponding to amplification and threshold of the reduced field from proportional photons, respectively.

The S1 and S2 signals are detected by two arrays of photomultiplier tubes (PMT) arranged at the top and bottom of the detector, fully immersed in liquid and gaseous phase. The two arrays are shown in figure 3.4. The PMTs have a quantum efficiency of about 30 % at a wavelength of 178 nm and an intrinsic radioactivity of about 1 $\frac{\mathrm{mBq}}{\mathrm{PMT}}$ [Apr10b]. Because of the large refractive index of liquid xenon of 1.69 ± 0.02 [Sol04] there is a large amount of total internal reflection at the liquid surface, leading to a detection efficiency of the S1 light signal at the bottom PMT array of about 80 %. This effect is further enhanced by the walls of the TPC, which are made of polytetrafluorethylene (PTFE) providing high reflectivity for VUV[3] scintillation light [Yam04].

---

[1] Xe_2^* is produced both by direct excitation and electron-ion recombination. The detailed process is described in chapter A.1.

[2] The extraction yield for electrons in gaseous phase is close to 100 % for an electric field $\mathcal{E} > 10\,\frac{\mathrm{kV}}{\mathrm{cm}}$ [Apr04].

[3] VUV = vacuum ultraviolet

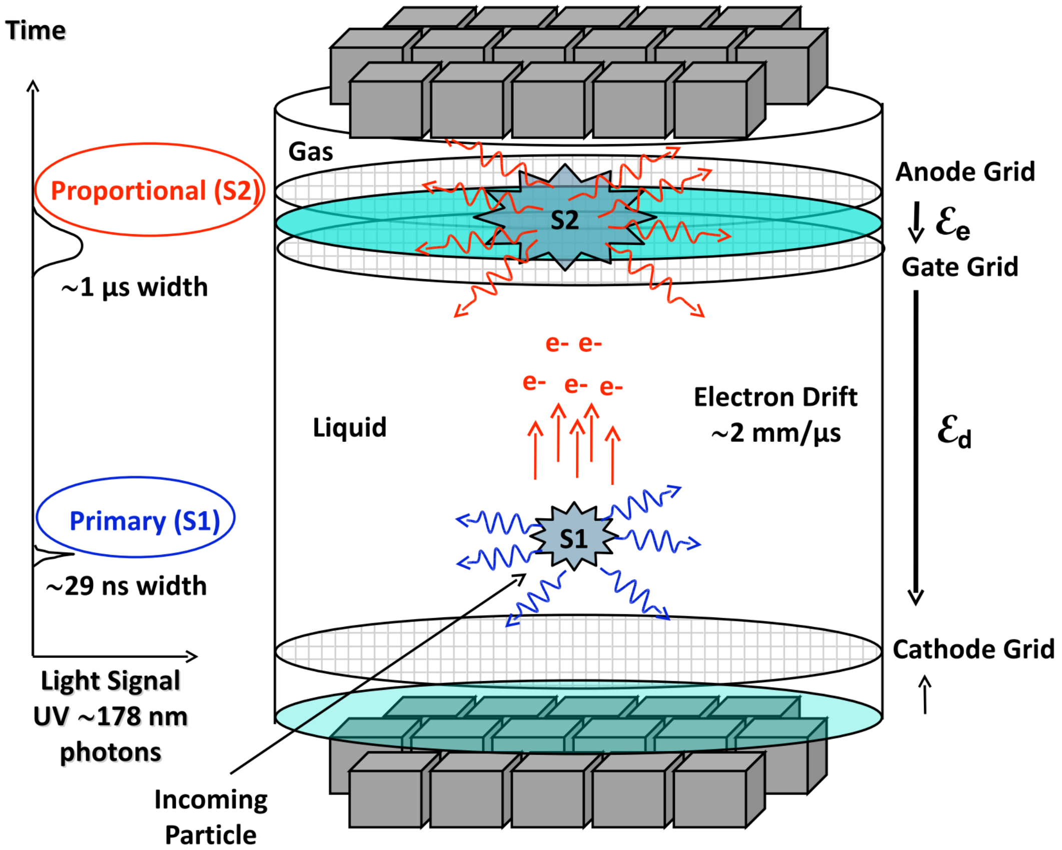

Figure 3.2.: *Schematic principle of the XENON two phase time projection chamber. The TPC has a cylindrical shape with a height of 30.5 cm and a radius of 15.3 cm. Particle interactions in liquid phase cause primary scintillation light (S1 signal) and ionization electrons. The electrons are drifted to the top of the detector where they are extracted into the gaseous phase and accelerated, giving rise to proportional scintillation light (S2 signal). The S1 and S2 signals are simultaneously detected by two arrays of photo multiplier tubes (PMTs) at the top and bottom of the detector [Apr11e].*

3.2.1. Background discrimination

Simultaneous detection of the S1 and S2 signals allows for discrimination between nuclear recoil due to WIMP or neutron interactions and electron recoil due to electron or gamma interactions. This specific discrimination is feasible, as ionization densities from nuclear recoils due to neutron or WIMP interaction differ from the ionization densities arising from electron recoils due to gamma or beta backgrounds (figure 3.3). The different amplitudes in the S2/S1 ratios can therefore be used to discriminate between these two types of recoil events with an efficiency of 99.5 % at 50 % nuclear recoil acceptance [Ang08][Apr11b].

A three dimensional reconstruction of the area of interaction is done by the top array of PMTs which resolves the x-y coordinates with a precision better than 2 mm [Apr10b]. A typical hit pattern is illustrated in figure A.3 in the appendix. As the transverse diffusion coefficient of electrons in liquid xenon at an electric field of 1 $\frac{\text{kV}}{\text{cm}}$ is $D_T(\text{LXe}) = 80\,\frac{\text{cm}^2}{\text{s}}$, electron diffusion is rather small [Apr10d]. Therefore the x-y coordinates of the secondary scintillation light are assumed to be about the same as the x-y coordinates of the interaction vertex in liquid phase. The z coordinate is determined by the drift time

(a) Nuclear recoil signals (WIMP)

(b) Electronic recoil signals (γ and β)

Figure 3.3.: *Schematic sketch of the S1 and S2 waveforms for nuclear (a) and electronic recoil (b). The ratio between the S1 and S2 signals allows for discrimination between nuclear recoil due to WIMP or neutron interactions and electron recoil due to electron or gamma interactions [Apr11b].*

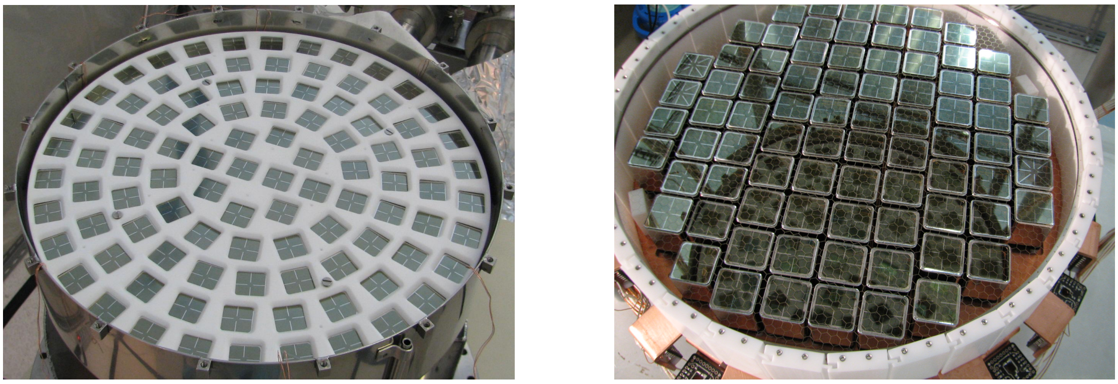

(a) Top array of PMTs in the XENON100 detector

(b) Bottom array of PMTs in the XENON100 detector

Figure 3.4.: *The XENON100 experiment uses Hamamatsu R8520-06-Al PMTs. The PMTs at the top of the detector are arranged in concentric rings in order to offer best reconstruction of the radial interaction position. A typical hit pattern is shown in figure A.3 in the appendix. The PMTs at the bottom of the detector are packed as closely as possible to optimize the light collection, which is necessary in order to get a low energy threshold of the detector [Apr11b].*

of the electrons, measured by the time difference of the S1 and S2 signals. Further discrimination comes from fiducializing the volume in order to reject surface effects and contaminations.

These properties are further exploited as an active veto for muon induced neutrons arising from the surrounding rock material. The liquid inside the TPC is held at a precise level with the help of a diving bell. Therefore the liquid level outside the bell can have any arbitrary height. The XENON100 detector has a 4π coverage of 4 cm thick liquid xenon veto of about 100 kg, which is observed by 64 PMTs operating in anti-coincidence mode [Apr11c].

The entire TPC shown in figure 3.5 is enclosed in a double walled vessel made of SS 316Ti.

3.3. Backgrounds and impurities

3.3.1. Shielding

The Laboratori Nazionali del Gran Sasso (LNGS) offers a shielding of 1400 meters of rock corresponding to 3100 meters of water equivalent reducing the neutron and cosmic muon flux by factors of 10^3 and 10^6, respectively [Bet02][Apr10b].
Remaining neutron background due to muon induced neutrons and (α,n)-reactions from the surrounding rock materials, namely ^{238}U, ^{232}Th, ^{210}Pb as well as gamma background is faced with different shieldings.
The passive shielding from outside to inside comprises a 20 cm water shield, a 20 cm thick combination of lead and low radioactive lead with a minor contamination of ^{210}Pb having an activity of $26 \pm 6 \frac{\mathrm{Bq}}{\mathrm{kg}}$ [Apr11d]. The low radioactive component takes 5 cm of the innermost layer. An additional 20 cm thick layer of polyethylene moderates and absorbs neutrons. Finally, the detector is covered by a 5 cm thick vessel of highly pure oxygen-free, high-conducting copper [Bro10][Apr10b].
Therefore the majority of alpha and beta particles are absorbed before penetrating the detector. Furthermore, all materials used in the detector have been screened for their radioactivity by a 2.2 kg high purity germanium detector in a dedicated ultra low-background screening facility at LNGS [Apr11b].
Moreover, highly pure boil of nitrogen is purged into the inner shielding part with a flow rate of 17 standard liters per minute (SLPM). This is done in order to reduce radon contaminations emerging from uranium and thorium decay chains from the surrounding rock material below $1 \, \frac{\mathrm{Bq}}{\mathrm{m}^3}$ [Apr11b].
Remaining surface effects originating from gamma backgrounds from detector materials such as ^{238}U, ^{232}Th, ^{40}K and ^{60}Co as well as their daughters are addressed by the previously mentioned fiducial volume cuts.

3.3.2. Electronegative Impurities

Electronegative impurities such as oxygen or water dramatically reduce the efficiency of the detector. Oxygen reduces the drift length of electrons in the liquid [Bak76], whereas water absorbs the emitted scintillation photons [Bal05]. Purification in order to reduce these contaminations below the ppb level is continuously done by circulation through a high temperature metal getter. Xenon gas is transmitted over a zirconium surface of 400 °C which forms irreversible chemical bonds with the impurities. A reduction below 1 ppb (oxygen equivalent) corresponds to an absorption length of more than one meter [Apr10d].

3.3.3. Krypton background

Commercially available xenon always consists of a certain fraction of krypton due to its production techniques. Xenon is usually extracted from the air by distillation processes. Air consists on average of a fraction of 1.14 ppm [Wil09] and 90 ppb [Häu06] of krypton and xenon, respectively.
As a consequence of nuclear weapon tests above ground and civil use of nuclear power, especially nuclear reprocessing, the concentration of the krypton isotope ^{85}Kr, which is a product of fission of uranium and thorium, was enhanced to an abundance of $\frac{^{85}\mathrm{Kr}}{\mathrm{Kr}} = (1.5 \pm 0.4) \cdot 10^{-11}$ [Che99].
^{85}Kr makes up one of the major backgrounds of the experiment as it decays via β^-−decay with a half life of $t_{\frac{1}{2}} = 10.76$ years and an energy release of $Q_\beta = 678.1$ keV [Ack11].

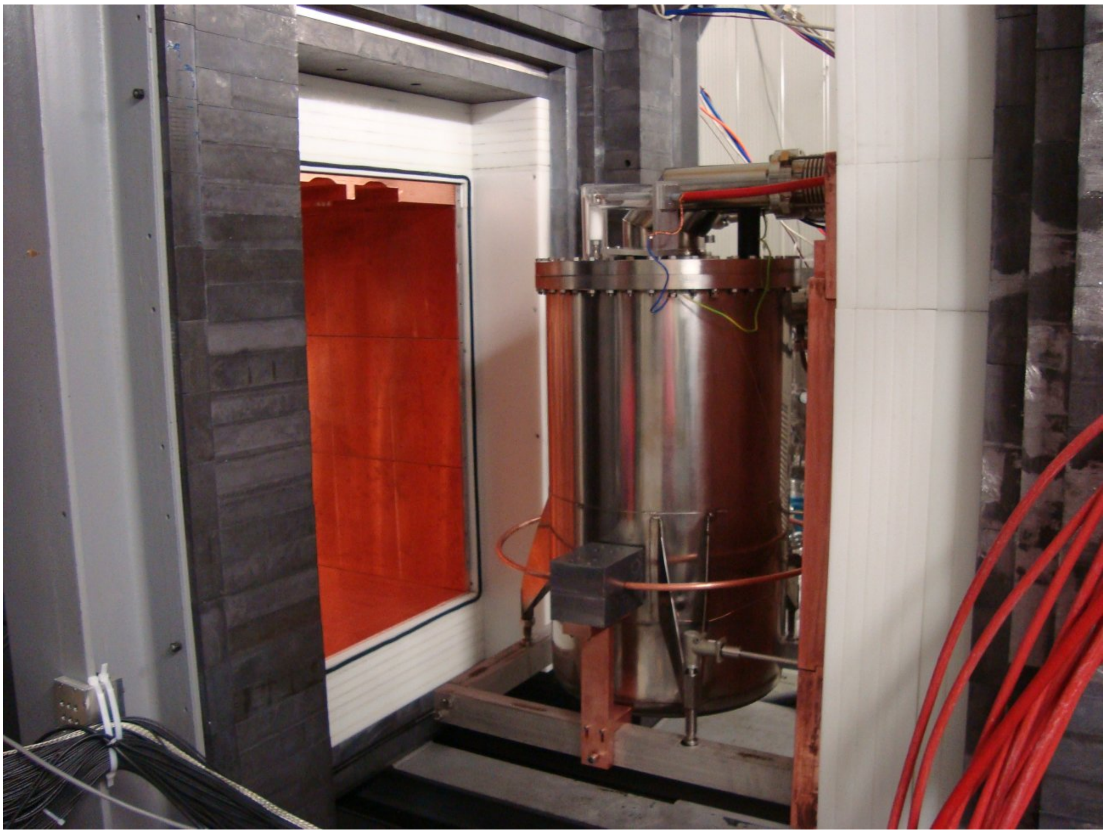

Figure 3.5.: *The XENON100 detector enclosed in the titanium vessel with open shield structure comprising copper, PTFE and lead blocks. The circular copper pipe around the detector enables insertion of calibration sources [Apr10c].*

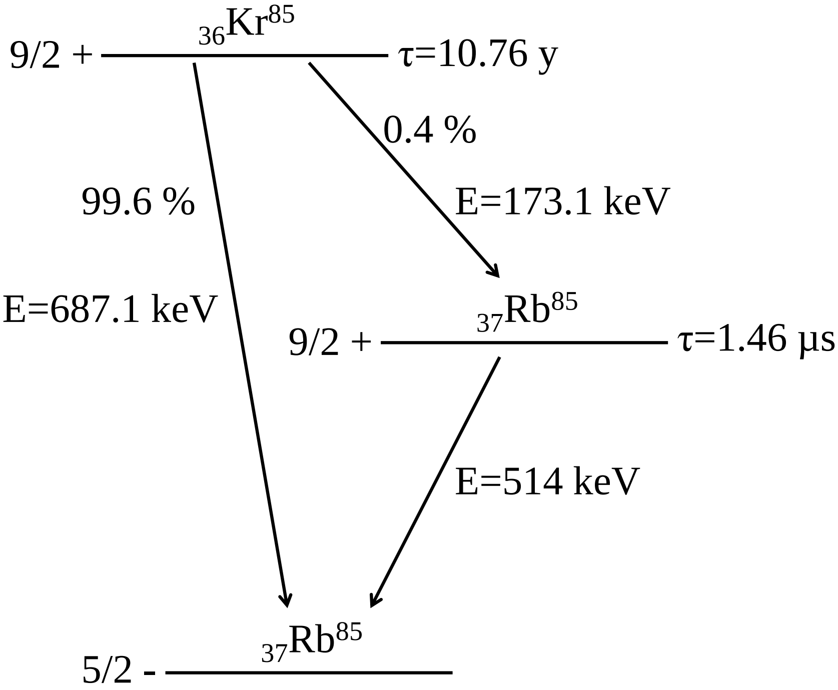

Figure 3.6.: *Decay diagram of* ^{85}*Kr [Apr11b].*

The decay scheme of ^{85}Kr is visible in figure 3.6. As an intrinsic background in the xenon, krypton contaminations cannot be addressed with fiducial volume cuts. Moreover, its half life is too long to just wait until most of the ^{85}Kr is decayed.

Therefore a krypton distillation column was used in XENON100 in order to reduce the total amount of krypton in xenon by a factor 1000 with a flow rate of 1.8 SLPM $= 0.6\frac{\text{kg}}{\text{h}}$. The remaining activity due to ^{85}Kr was measured by beta-gamma delayed coincidence to 33 $\frac{\mu\text{Bq}}{\text{kg}}$ [Apr11e]. The total fraction of krypton in xenon was estimated to be around 140 ppt which corresponds to 4.2 mdru[4]. More details about the applied analysis techniques are discussed in section 4.1.

3.4. Going to the ton scale - XENON1T

XENON100 has begun to probe the predicted phase space by Roszkowski et al. visualized in figure 2.9 in chapter 2. Its successor Xenon1T comprising 2500 kg of xenon with a fiducial target mass of 1000 kg will probe much deeper into the region, with a high likelihood for discovery. XENON1T aims at a projected sensitivity of

$$\sigma_{SI} \lesssim 10^{-46}\ \text{cm}^2 \qquad \text{[Apr10a]} \tag{3.2}$$

by 2015. In order to achieve this goal various research and investigations are done to develop a ton scale Dark Matter detector.

The previously mentioned background due to ^{85}Kr, for example, would become a serious problem if XENON100 is upscaled to XENON1T. The fraction of krypton in xenon has to be reduced beyond the ppt level in order to decrease the entire experimental background down to 0.1 mdru.

3.4.1. Münster's contribution

The XENON collaboration consists of many collaborators all around the world. At Münster research and development of purification methods are done. Since 2010 a prototype of a new gas system comprising a TPC and different gas analysis and purification devices is under development.

In order to satisfy the highest standards of cleanliness the entire system is all-metal sealed, electro-polished and orbital welded. Moreover, the system is bakeable up to 150 °C. The braced leak-rate of $L < 10^{-10}\frac{\text{mbar}\cdot\text{L}}{\text{s}}$ will presumably be achieved after installing a second containment filled with dry nitrogen taking care of known leak-rates of commercially bought components. For example, the *KNF* neoprene membrane pump for gas circulation, which pumps the gaseous xenon through the system has a leak-rate of $L \sim 10^{-7}\frac{\text{mbar}\cdot\text{L}}{\text{s}}$. A schematic sketch of the gas system is shown in figure 3.7.

The TPC is designed for in situ purity monitoring via electron drift length measurements and characterization of the krypton distillation column.

The system is fully automated with pneumatic bellow valves (SS-8BG-VCR-5C) controlled by *LabView*. Xenon handling such as filling the TPC, recirculation and recuperation has been tested and approved with a flow rate up to 30 SLPM [Ros13].

The filling level of the storage bottles made of aluminum is controlled by two independent methods. Firstly, the bottles are suspended at load cells emerged in dewars filled with liquid nitrogen. Considering their buoyant force the filling level can be calculated from the measured weight. Secondly, the inlet of the gas bottles is monitored by the *MKS Mass Flow Controller*.

---

[4] 1 dru $= 1\,\frac{\text{Event}}{\text{kg}\cdot\text{keV}\cdot\text{day}}$

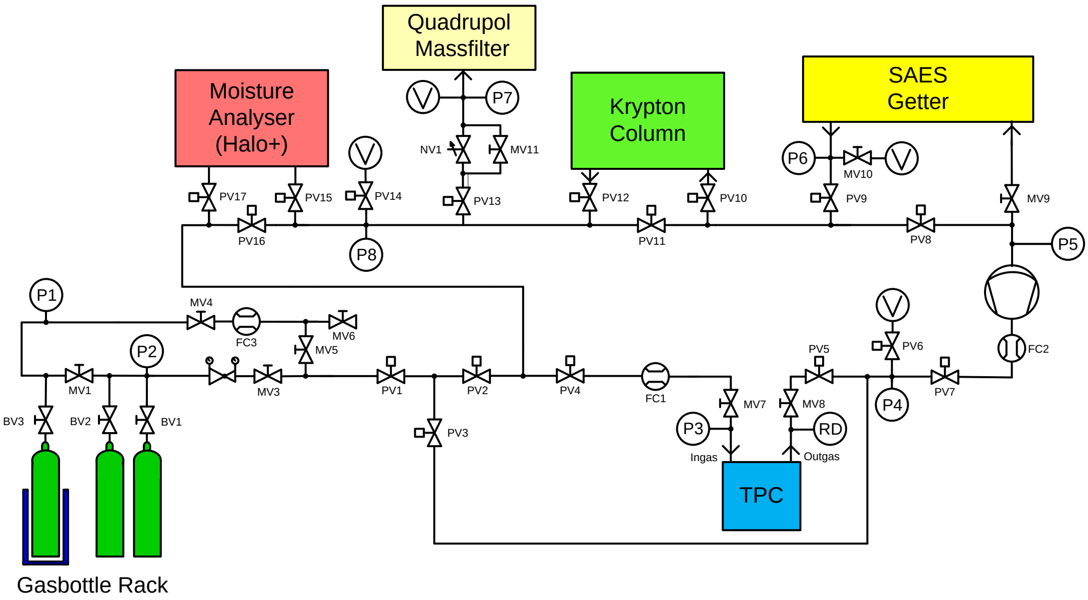

Figure 3.7.: *Prototype of gas system developed at Münster comprising a TPC, a cryogenic krypton distillation column, a getter, a halo monitor and a quadrupole mass filter which is at the moment a stand-alone system and not directly connected to the gas system [Ros13]. A photograph can be found at the end of this section in figure 3.8.*

Electronegative purification

As mentioned previously electronegative impurities such as oxygen or water reduce the efficiency of the detector. The *SAES MonoTorr High Flow PS4 MT50-R Getter* which is operated at Münster's gas system is able to reduce contaminations of O_2, H_2O, CO, CO_2, H_2, N_2 and CH_4 with a flow rate up to 75 SLPM.

The xenon gas is continuously transmitted over a zirconium surface of 400 °C which forms irreversible chemical bonds with the impurities.

Moisture measurement

The amount of moisture[5] in xenon is determined by the *Halo+ Trace Gas Analyzer* (M7103 Series) from Tiger Optics which uses a cavity ring down spectroscopy technique. The wavelength of a diode laser is measured in the IR region where absorption due to water contaminations takes place and is then compared with a wavelength signal at a region where no absorption takes place. In more detailed terms: Not the signal of the laser beam itself, but its decay over time is measured.

Inside an optical resonator (cavity) whose volume is filled with sample gas a laser beam is reflected many times, while a small fraction of the signal is decoupled at each reflection, giving rise to a *ring down signal*. The laser is switched off when the light signal is detected for the first time. Then the signal decays, following first principles of Lambert–Beer's law

$$I = I_0 \cdot e^{-\frac{t}{\tau}} \qquad ; \qquad \tau \sim \mu s \qquad \text{[Tig06]} \tag{3.3}$$

and can be compared with a ring down signal at a region where no absorption takes place.

A precise and stable in situ calibration can be done with the same gas sample by tuning the laser of the absorption peaks and measuring the ring down time again.

---

[5] Concentration of water

The *Halo+* provides a non destructive technique independent of sample pressure which is sensitive to 200 ppt of water in xenon.

The krypton distillation column

Assuming the abundances of the different krypton isotopes do not change during the distillation processes the amount of ^{85}Kr can be reduced by a sequence of cryogenic distillations. To a good approximation this is valid, as distillation is a chemical process only sensitive to properties of a specific element such as melting or boiling points, but not to isotopic deviations.

The existing krypton column of the XENON100 experiment offers a reduction factor for krypton in xenon of about 1000 at a flow rate of 1.8 SLPM = 0.6 $\frac{\text{kg}}{\text{h}}$.

For the XENON1T experiment a new column with higher efficiency has to be designed. The column currently developed at Münster is designed for a feeding flow rate of 3 $\frac{\text{kg}}{\text{h}}$ which corresponds to 500 $\frac{\text{kg}}{\text{week}}$. This high flow rate is necessary in order to purify the entire amount of xenon of about 2500 kg within an adequate time scale.

The overall aim is a reduction of the krypton fraction below the ppt range at a consumption efficiency of 99 %. Assuming a concentration of 10 ppb in commercially available xenon a reduction factor of 100,000 is needed.

Residual gas analyzer

In order to characterize the krypton distillation column the krypton content in the xenon has to be measured before and after processing the gas through the column. The measurement beforehand is necessary for two reasons. Firstly, the reduction factor of the column of 10^5 needs to be verified. Secondly, the initial concentration of krypton within the commercially bought xenon has to be known in order to optimize the purification process. The specified purity of the xenon gas from *AirLiquide* which is used at Münster is shown in table A.3 in the appendix.

Apart from radioactive tracers[6] such as $^{83\text{m}}$Kr the separation efficiency of the distillation column can be investigated with a residual gas analyzer (RGA).

The RGA is at the moment a stand-alone system which is not directly connected to the gas system. The following part of this thesis deals with the applications of a RGA. In particular it describes how trace amounts of krypton in xenon can be detected.

The RGA does not directly measure the content of ^{85}Kr in the xenon, but the concentration of other krypton isotopes. As the natural abundance of ^{85}Kr is known to be

$$\frac{^{85}\text{Kr}}{\text{Kr}} = (1.5 \pm 0.4) \cdot 10^{-11} \qquad \text{[Che99]}, \tag{3.4}$$

its concentration can be inferred from the amount of other krypton isotopes present in the xenon.

Furthermore, the relative isotopic composition between ^{84}Kr and ^{78}Kr provides a dynamic range of 160, which can be used in order to determine the sensitivity for trace amounts of krypton. All abundances for krypton and xenon can be found in table A.4 in the appendix.

Moreover, the RGA can be used in addition in order to measure a full bunch of other gas species including the isotopic composition of the xenon gas itself.

---

[6] $^{83\text{m}}$Kr is short-lived with a half life of 1.83 hours.

Figure 3.8.: *Prototype of gas system schematically shown in figure 3.7. The SAES getter is housed in the gray board which can be seen on the right hand side. Behind the getter inside a black box the Halo+ Trace Gas Analyzer is located. The blue KNF pump for gas circulation is visible centered underneath the gas rack. The pneumatic bellow valves are housed inside the black boxes at the top of the gas rack. The turbo molecular pump is placed precipitately on top of the gas rack in the upper left corner.*

4. Detection methods for krypton

For the XENON experiment it is essential to measure either the fraction of ^{85}Kr in xenon or the total amount of krypton in order to infer back to the amount of ^{85}Kr by its natural abundance.

Noble gases like krypton and xenon are hard to detect, as they do not take part in chemical interactions. Moreover, both their chemical and physical properties are similar, as they are both in the 18th group of the periodic table of elements and consequently have the same electronic structure concerning their outer shell.

Besides measuring directly the amount of ^{85}Kr via low level counting of its decay the total amount of krypton can be investigated by atom traps or mass spectrometry and afterwards extrapolated with respect to the known isotopic ratios.

In the XENON collaboration different techniques have been used in order to detect trace amounts of krypton in xenon. Without claiming completeness the most important ones are introduced briefly.

4.1. Low level counting (LLC)

As mentioned previously in section 3.3.3 the dominant decay mode of ^{85}Kr is beta decay with a Q-value of 687.1 keV. Furthermore, there exists a second decay mode with a branching ratio of 0.454 %, namely

$$^{85}\mathrm{Kr}(\beta, 173\ \mathrm{keV}) \rightarrow {}^{85m}\mathrm{Rb}(\gamma, 514\ \mathrm{keV}) \rightarrow {}^{85}\mathrm{Rb}\,, \tag{4.1}$$

with the intermediate state having a life time of 1.46 μs [Apr11b]. This delayed coincidence signal can be used in order to enhance the sensitivity of a low level counting measurement significantly. An event is identified, whenever a primary signal between 20 keV and 210 keV is followed by a secondary signal between 300 keV and 700 keV, and both signals are measured with a time delay of $0.3\,\mu\mathrm{s} < \Delta t < 5\,\mu\mathrm{s}$.

These cuts enable a direct measurement of ^{85}Kr by delayed coincidences with a signal acceptance of 30 % [Apr11b].

In XENON100 the total krypton fraction in xenon for the commissioning run was determined to $\left(143^{+135}_{-90}\right)$ ppt[1] at 90 % confidence level [Apr11b].

---

[1] 100 ppt of $\frac{\mathrm{Kr}}{\mathrm{Xe}}$ yield to $2 \cdot 10^{-3}$ dru [Apr11c].

4.2. Atom trap trace analysis (ATTA)

Atom trap trace analysis (ATTA) is a laser-based technique enabling detection of single laser-cooled isotopes.

A collimated beam of metastable atoms is guided to a single atom trap with a fluorescence detector.

The beam consisting of krypton atoms is excited to an optically accessible metastable state. Krypton atoms can be trapped for about 40 s in the $^3P_2$ metastable state [Che99]. As the krypton beam has to be slowed down from thermal energy to the milli Kelvin range, additional laser cooling is required. Optical molasses accomplished with laser beams collimate Kr^+ ions and reduce their transverse velocity. Photons from a laser are red-shifted, so that atoms moving towards the laser beam absorb the light due to the Doppler effect. The following emission occurs isotropically and therefore an effective force due to the momentum transfer during the absorption and emission is generated. A Zeeman slower[2] counteracts the Doppler shift, allowing atoms to stay in resonance with the coaxial laser during the cooling process [Bag89].

The atoms are trapped in a magneto optical trap (MOT), which uses a linear magnetic field gradient in order to confine the atoms. Finally, the atoms are detected by their fluorescence light with a CCD camera or an avalanche photo diode.

The XENON100 collaboration is investigating this method at Columbia University. The system is ready to use and testing has started. A schematic drawing of the ATTA setup of the Columbia group is shown in figure 4.1.

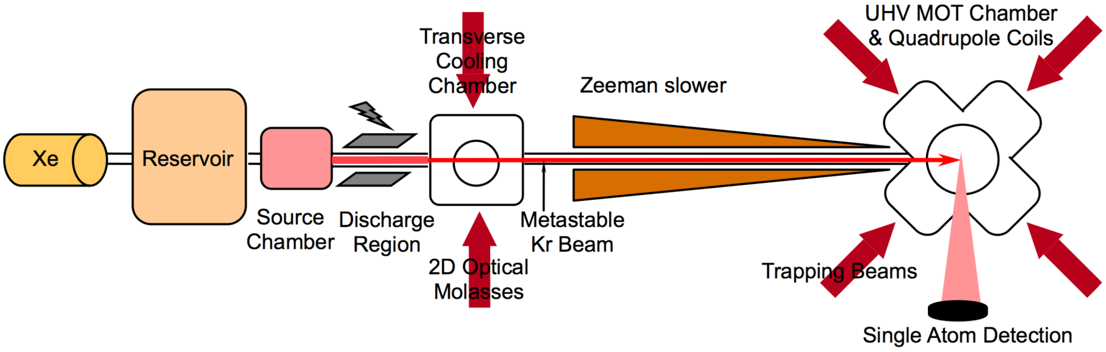

Figure 4.1.: *Schematic drawing of the ATTA system at Columbia University [Apr09].*

4.3. Gas chromatography mass spectrometry (GC-MS)

Krypton contaminations in xenon can be detected by mass spectrometry via their mass to charge ratio. However, big samples cannot be used as the xenon bulk would cause the mass filter to saturate. Therefore the krypton fraction needs to be separated from the xenon.

Gas chromatography can be used to extract components from a mixture exploiting different physical and chemical properties of each component. The most important ones are polarity, melting and boiling points as well as vapor pressure.

An inert carrier gas (mobile phase) transports the sample through the system. The different components linger in the columns (stationary phase) for different lengths of time due to interactions with the column surface or additional material inside the column

---

[2] One dimensional spatially varying magnetic field

[Gro04]. The dwell time until the different components elute from the column mainly depends on polarity and vapor pressure of the sample components.
Because of its higher vapor pressure krypton elutes much faster than xenon and its concentration is therefore enhanced. In an ideal case krypton is completely separated from the sample.
The XENON100 collaboration is investigating the GC-MS method at MPI Heidelberg. The system is operating and has analyzed samples from the run 10 of the XENON100 experiment yielding a concentration of (21.0 ± 0.6) ppt $\frac{\mathrm{Kr}}{\mathrm{Xe}}$.

4.4. Cold trap enhanced mass spectrometry (CT-MS)

In the following chapter a different technique is discussed in detail, namely the combination of a residual gas analyzer and a cold trap exploiting only the difference in vapor pressure of krypton and xenon.

4.5. Summary

All methods for krypton detection described in this chapter are non-destructive. Even if ATTA and GC-MS consume the sample, the required mass is so small that they can still be counted as non-destructive techniques.
LLC enables in-situ measurements during operation measuring the amount of ^{85}Kr directly. A disadvantage of LLC is that the result is not known before the experiment starts.
ATTA has ultra high precision and is the only technique besides LLC capable of measuring ^{85}Kr directly.
GC-MS and CT-MS have the advantage that they produce xenon samples with reduced krypton content within a secondary effect. This highly purified sample can be used for further research and development.

5. Experimental Setup

A cryogenic distillation[1] column for krypton removal from commercially available xenon beyond the ppt-level for the XENON1T experiment is being designed at Münster. In order to characterize and optimize this column a precise measurement of the krypton concentration before and after the rectification process is necessary.

As mentioned in chapter 4 noble gases like krypton and xenon are hard to detect. [Leo10], [Dob11] and [Apr09] have shown that combinations of mass spectrometry with cold traps or rather penning traps are able to address these problems.

The following chapter describes how the concept developed by [Dob11] et al. is adapted and modified in order to analyze trace amount of krypton in xenon.

5.1. Gas composition measurements using a residual gas analyzer (RGA)

A residual gas analyzer (RGA) is a mass spectrometer for monitoring residual gas compositions in a vacuum environment. Often linear quadrupole technology is used because of its robustness and the potential of high out-baking temperatures, which is necessary for ultra high vacuum applications.

Depending on the cleanliness of the vacuum system trace amounts of samples species can be detected. Common RGAs have to be operated under a vacuum of $10^{-4} - 10^{-5}$ mbar for two reasons. Firstly, the different components of the RGA such as ion source or detector may take damage due to high pressures. Secondly, the substance of interest has to be ionized and guided to the detector requiring that the mean free path of the ion is greater than the dimensions of the RGA.

Moreover, a RGA can be operated as a sensitive in-situ helium leak detector. Further information about leak testing is given in section 5.3.

5.2. Detection of trace gas samples using a quadrupole mass filter

In order to detect trace amounts of krypton the technique of linear quadrupole mass spectrometry is used. In the following sections the experimental setup and the *Transpector2 H200M* quadrupole mass filter which is used in this experiment are described in detail.

As schematically shown in figure 5.1 a quadrupole mass filter analyzes the residual gas by ionizing the gas molecules and then passing the ions through a filter that only allows ions with a certain mass to charge ratio to reach a detector.

---

[1] A sequence of distillation steps called *rectification* will be used.

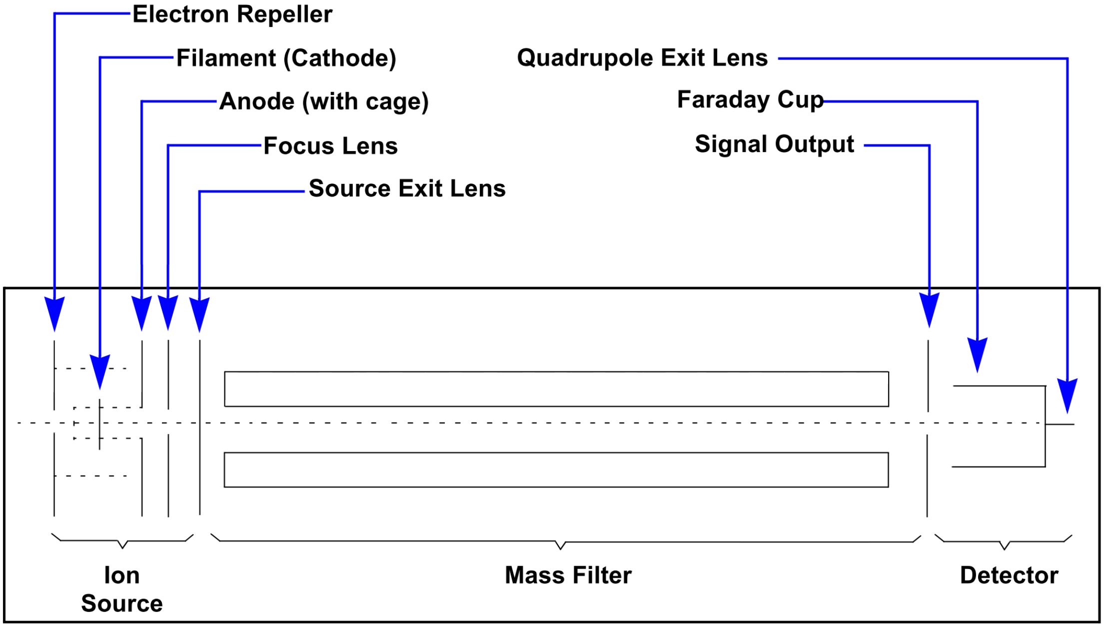

Figure 5.1.: *Schematic sketch of the Transpector2 H200M showing its three major components, namely the ion source, the mass filter and the detector [Inf04].*

Ion source

The Transpector2 uses the electron ionization (EI) technique to produce ions. A DC current heats up a filament made of an iridium wire with thorium-oxide[2], emitting electrons which ionize the gas molecules.

Ionization processes under high vacuum conditions underlie the principles of chemistry of isolated ions in gaseous phase. EI predominantly produces single positively charged radical ions [Gro04]. However, depending on the energy of the emitted electrons and the sample species multiple charged ions may be created as well. In general these ions have a lower abundance than the single charged ones [Mey62].

$$\mathrm{A} + e^- \rightarrow \mathrm{A}^{+\bullet} + 2\,e^- \tag{5.1}$$
$$\mathrm{A} + e^- \rightarrow \mathrm{A}^{2+} + 3\,e^- \tag{5.2}$$
$$\mathrm{A} + e^- \rightarrow \mathrm{A}^{3+\bullet} + 4\,e^- \qquad \text{[Gro04]} \tag{5.3}$$

The multiple charged ions are of vital importance for characterizing and distinguishing different elements.

The thermal emission current density j of the electrons is given by the Richardson-Dushman equation

$$j = -\underbrace{\frac{k_B^2\, m\, e}{2\,\pi^2\,\hbar^3}}_{\mathrm{A}} T^2 \cdot e^{-\frac{\phi}{k_B T}} \qquad \text{[Kit06]}, \tag{5.4}$$

where A is the Richardson constant and $\phi = E_{\mathrm{vac}} - E_{\mathrm{F}}$ the work function given by the difference of the vacuum energy E_{vac} and the Fermi energy E_{F}.

The energy of the emitted electrons is usually around $70 - 100$ eV, which corresponds to a de-Broglie wavelength of $\lambda = \sqrt{\frac{h^2}{2mE}} \approx 1.2 - 1.5$ Å. The ionization cross-section

---

[2] Modern iridium based filaments can be turned on at atmospheric pressure without being destroyed instantly.

for most elements has a maximum at this energy, as it is visualized in figure A.2 in the appendix.

Fragmentation processes of the arising ions due to endothermal bond breaking are not discussed in this thesis, as only single atoms are analyzed.

Inside the Transpector2 quadrupole mass filter an ion cage, which is connected to the anode is mounted centered around the curved filament. An open mesh structure of the cage provides gas flow into the ionizing region. The anode is on positive potential with respect to the electron repeller, which has an open mesh structure as well. The potential of the filament is hold between the potential of the two electrodes. The produced ions are then extracted by a focus lens and form a beam. As the Transpector2 is designed in order to detect positive ions[3] the focusing lens is biased with negative potential with respect to the anode. The source exit lens, which has a negative potential with respect to the anode as well injects the ion beam into the mass filter.

Those ions, which do not pass the beam line hit the exit lens and are neutralized. The emerging current flow at the exit lens is related to the pressure inside the ion source and therefore proportional to the total pressure in the system. The Transpecter2 takes advantage of this by triggering to some current threshold and switching off the operation voltages, preventing damage to the filament and the detector due to overpressure at $p_{\mathrm{max}} \sim 4 \cdot 10^{-5}$ mbar [Inf04].

Analyzing section

An ideal quadrupole mass filter consists of four hyperbolically shaped, alternately charged rods, which are arranged in a square array. A schematic sketch of a quadrupole is visible in figure 5.2.

In practice usually cylindrically shaped rods are used, as they are easier to produce. According to [Day54] and [Inf04] the resulting electric field due to cylindrically shaped rods is a reasonably good approximation in case the ratio of the round rod radius to the quadrupole radius r_0 is equal to 1.148.

An ion inside the quadrupole mass filter will be attracted by those rods which are oppositely charged. Applying a periodic potential to the rods leads to alternating attraction and repulsion of the ion from the rods according to the frequency of the potential.

An analytical solution of an ideal quadrupole with hyperbolical rods is presented in the following.

The force $\vec{F}$ effecting the motion of an ion is scaling linear in distance $\vec{r}$.

$$\vec{F} = -e \cdot \vec{\nabla}\Phi = -c\vec{r} \qquad ; \qquad c = \text{const.} \tag{5.5}$$

As the potential $\Phi(x,y,z,t)$ has only a quadratic dependence on the Cartesian coordinates x,y and z, one obtains

$$\Phi(\vec{r},t) = \Phi_0(t) \cdot (ax^2 + by^2 + cz^2) \tag{5.6}$$

Applying the Laplace Equation $\Delta\Phi = 0$ one obtains $a + b + c = 0$.

One a priori solution to fulfill this case is:

$$a = -b \qquad \text{and} \qquad c = 0$$

---

[3] This fact does not limit the application range as negative krypton ions are unstable, meaning that electron capture is only favored by protonated molecules at low electron energies of < 0.2 eV [Gro04]. Moreover, noble gases like krypton or xenon do not have the ability to tolerate additional electrons by delocalization or hyperconjugation as molecules do.

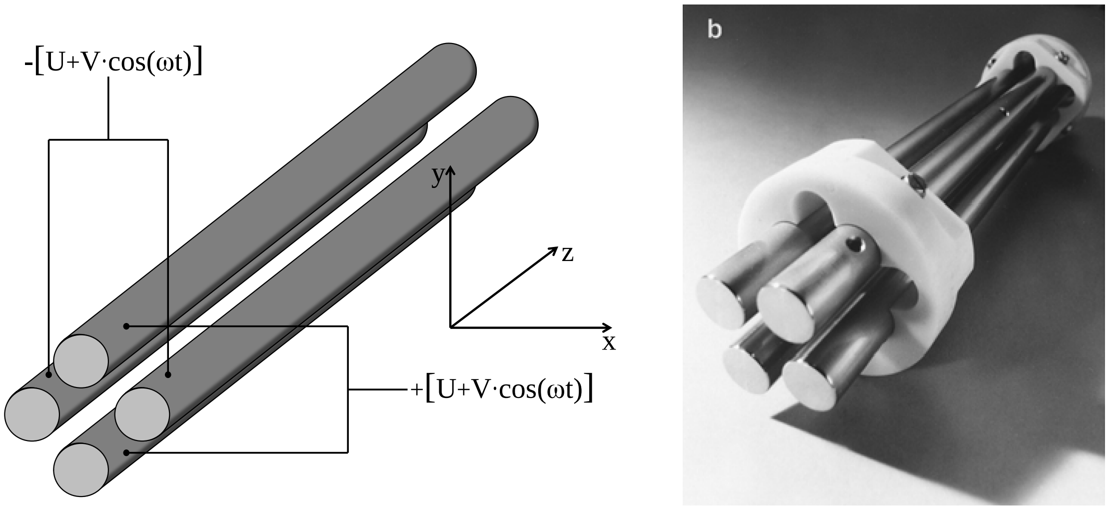

(a) Cross-section through the four rods of a quadrupole mass filter in the x-y plane. Neighboring rods lie on opposite potential, whereas opposite rods lie on equal potential.

(b) Photograph of a quadrupole mass filter [Gro04].

Figure 5.2.: *Schematic sketch of the four rods of a quadrupole mass filter (a) and a corresponding photograph (b). The ions travel through the quadrupole along the z-axis.*

This solution corresponds either to a 2 dimensional field of a quadrupole mass filter or to a linear ion trap [Bla97].
The quadrupole radius r_0 is defined as the smallest distance between the center of the x-y plane and the closest rod surface. Choosing $a = -b = \frac{1}{r_0^2}$ the potential simplifies to

$$\Phi(\vec{r},t) = \Phi_0(t) \cdot \frac{x^2 - y^2}{r_0^2} \tag{5.7}$$

Ions inside the quadrupole will perform harmonic oscillations with exponentially increasing amplitude.
A quadrupole mass filter is operated with a potential Φ_0 composed of a DC voltage (U) and an AC voltage (V) with the frequency ω. Hence the resulting potential is:

$$\Phi_0(\vec{r},t) = [U + V \cdot \cos(\omega t)] \cdot \frac{x^2 - y^2}{r_0^2} \tag{5.8}$$

The differential equation of an ion of mass m inside the potential is given by

$$m\ddot{\vec{r}} + e\vec{\nabla}\Phi(\vec{r},t) = 0 \qquad \text{[Bla97].} \tag{5.9}$$

Accordingly the equation of motion for each dimension is

$$\ddot{x} + \frac{2e}{mr_0^2} \cdot [U + V \cdot \cos(\omega t)] \cdot x = 0 \tag{5.10}$$

$$\ddot{y} + \frac{2e}{mr_0^2} \cdot [U + V \cdot \cos(\omega t)] \cdot y = 0 \tag{5.11}$$

$$\ddot{z} = 0\,. \tag{5.12}$$

As the field is inhomogeneous, the time dependent part of the forces in the x-y plane does not vanish. The ions are always effected by a small force pointing at the direction of lower field strength.

Therefore some ions are able to pass the mass filter without hitting the rods. This is accomplished by oscillations around the z-axis with limiting amplitudes ($< r_0$).
Time integration of equation 5.12 gives $\dot{z} = \text{const}$. Consequently all ions injected into the mass filter travel with a constant velocity in the z direction.
The conditions for the oscillations in the x-y plane are described by Mathieu's differential equations [Gro04]

$$\frac{d^2x}{d\xi^2} + [a_x + 2q_x \cdot \cos(2\xi)] \cdot x = 0 \tag{5.13}$$

$$\frac{d^2y}{d\xi^2} - [a_y + 2q_y \cdot \cos(2\xi)] \cdot y = 0 \tag{5.14}$$

which can be obtained from equations 5.10 and 5.11 with the dimensionless transformation variables

$$a_x = -a_y = \frac{8eU}{mr_0^2\omega^2} \quad , \quad q_x = -q_y = \frac{4eV}{mr_0^2\omega^2} \quad \text{and} \quad \omega t = 2\xi \,. \tag{5.15}$$

Both equations 5.13 and 5.14 follow the same differential equation and can therefore be combined into the *normal form* of Mathieu's equations [McL47]:

$$\frac{d^2u}{d\xi^2} + [a_u - 2q_u \cdot \cos(2\xi)] \cdot u = 0 \quad ; \quad u = x,y \tag{5.16}$$

Trajectories inside the mass filter

Depending on the values of U, V and ω, stable and unstable trajectories for the motion of ions with certain $\frac{m}{z}$ values exist.

i) **Stable trajectory**
Ions oscillate with limited amplitude in the x-y plane and pass the mass filter without hitting the rods.

$$\lim_{\xi \to \infty} u(\xi) < r_0$$

ii) **Unstable trajectory**
Ions oscillate in the x-y plane with exponentially increasing amplitude, hitting the rods.

$$\lim_{\xi \to \infty} u(\xi) \geq r_0$$

A clear description of this stability is be given by considering the alternating electrical field. Ions inside the mass filter are alternatively focused and de-focused both in the x- and the y-direction. For certain frequencies and $\frac{m}{z}$ values this leads to the effect of *strong focusing* and therefore to stable ion trajectories.
The Mathieu functions can be interpreted as lines between stable and unstable regions. Figure 5.3 shows a stability diagram where these lines are plotted in the a-q plane.
The stability of a path of a given ion is defined by the magnitude of the AC voltage V and the ratio of the DC and AC voltage $\frac{U}{V}$.
The stability digram of a 2-dim quadrupole field is given by the transformation variables a and q, which correspond to the electric field constant and varying in time, respectively, where

$$\frac{a}{4} = \frac{eU}{\frac{mv^2}{2}} = \frac{eU}{\frac{mr_0^2\omega^2}{2}} \tag{5.17}$$

is the ratio of the potential Energy eU and kinetic energy $\frac{mv^2}{2}$ in the DC field [Bla97]. Consequently, regions exist where both x- and y-trajectories are stable. These stable regions can be found in figure 5.3 where the stable areas of both x- and y-components overlap. The regions of stability correspond to the overlap of the parameters a and q.

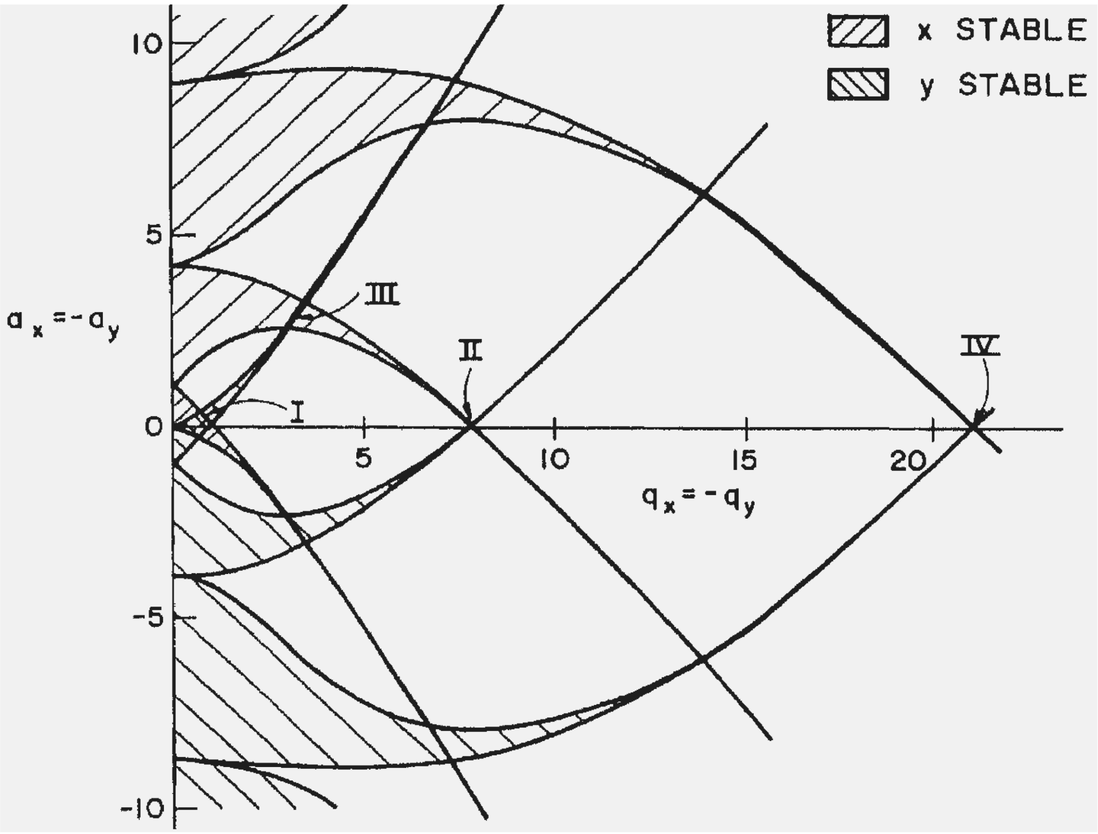

Figure 5.3.: *Stability diagram of a linear quadrupole mass filter. Stable regions (labeled with I-IV) can be found where stable x and y-parameters overlap [Gro04].*

For practical applications region I in figure 5.3 is of major interest and is therefore shown in more detail in figure 5.4. As already mentioned ion trajectories are stable in the case of both (a_x,q_x) and (a_y,q_y) are inside the stability region. The peak of region I can be found at

$$2\frac{U}{V} = \frac{0.237}{0.706} = 0.336 \tag{5.18}$$

which corresponds to the point of highest mass resolution [Gro04].

At a given value of U and V at constant r_0 and ω all ions of mass m are on a *load line* which is fully defined by the ratio of $\frac{U}{V}$.

In addition, reducing U while V stays constant allows a bigger $\frac{m}{z}$ range (Δq) to pass the mass filter.

By varying both U and V while keeping their ratio constant, ions of different $\frac{m}{z}$ values are transmitted through the mass filter (figure 5.5). This is how a scan over the entire mass range is done.

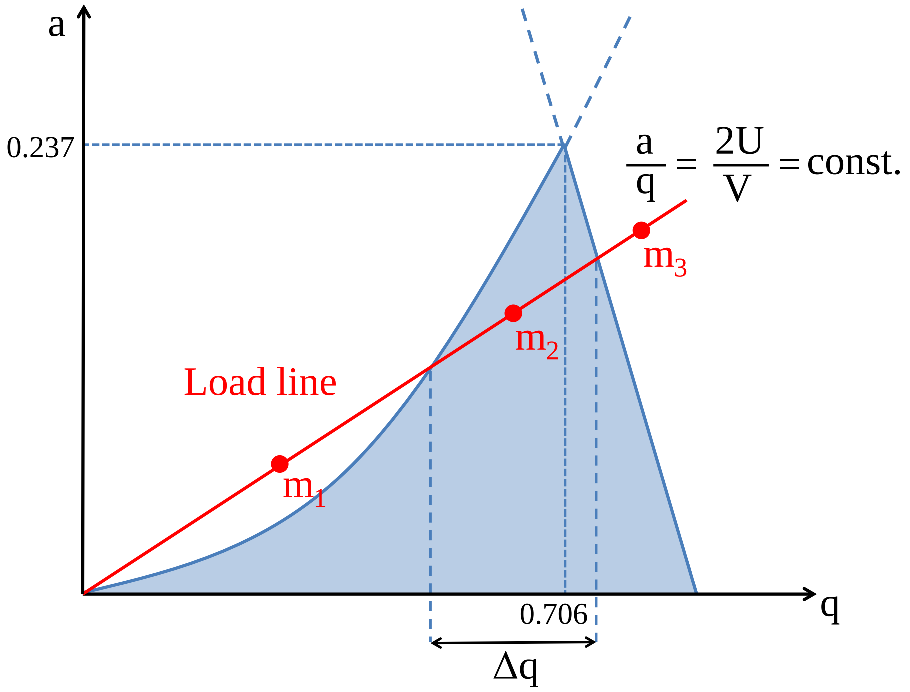

Figure 5.4.: *Stability region I of a linear quadrupole mass filter. The picture shows an enlargement of region I presented in figure 5.3. The masses m_1 and m_3 do not pass the mass filter as they lie outside the stability region, which is indicated in blue colors. In contrast m_2 with $m_1 > m_2 > m_3$ has a stable trajectory through the mass filter. An increase of the slope of the load line causes less masses to pass, but increases the resolution. Vice versa a decrease in the slope allows a larger mass range (Δq) to pass, but causes less resolution. Maximum resolution is achieved at the intercept of the load line with the apex of the blue colored triangle (0.706, 0.237). At $a = 0$ the resolution has a minimum and the mass filter becomes an ion guide transmitting all masses.*

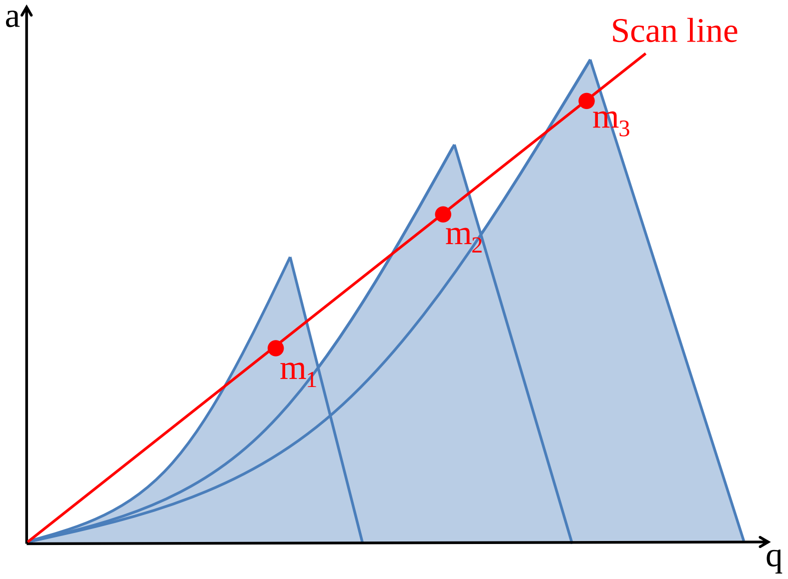

Figure 5.5.: *Stability regions of different masses $m_1 > m_2 > m_3$ lying on the same scan line for $\frac{U}{V} = const.$*

Detector

The detector is a combination of a Faraday Cup (FC) and a Channel Electron Multiplier (EM), which operates as an in situ preamplifier.

At the end of the detector with respect to the beam axis of the ions a quadrupole exit lens focuses the transmitted ions on the detector surface. Ions hit the metal surface of the detector, which is at ground potential and transfer a measurable current [Inf04].

By only scanning certain mass regions, the Transpector2 can be operated temporarily beyond the maximum specified pressure of $1.3 \cdot 10^{-5}$ mbar as long as the mean free path of the ions is larger than the mass filters dimensions. This is valid as long as the scanned region only contains sub-dominant contributions of the sample, as otherwise the EM would be exposed to high current values.

Units and conventions

There is no general convention about the unit of the mass to charge ratio $\frac{m}{z}$. In former times the unit Thompson $[\frac{m}{z}] = \mathrm{Th}$ was defined, which is used in the following.

In mass spectrometry the measured signals at different $\frac{m}{z}$ values are described equivalently as intensities I or rather currents I, depending on the particular application. In both cases the unit is ampere. In the following the convention of referring to intensities in order to describe mass spectra and their derivatives is used, whereas calculations will refer to currents.

5.3. Vacuum requirements

The sensitivity of the system is limited by the quality of the vacuum of the experimental setup. Therefore much effort has been spent on preparing and especially cleaning all components of the system.

All components are made of 316L stainless steal and have been cleaned within an ultrasonic bath. All connection surfaces (mainly *CONFLAT*) have additionally been cleaned with ethanol before being metal-sealed with oxygen-free, high-conducting copper rings.

The vacuum was allocated by an oil-free turbo molecular pump (Leybold Turbo Vac MAG W 300 P) with magnetic bearing, supported by a pre-vacuum of $\sim 10^{-2}$ mbar produced by an oil-free scroll pump (Scroll Vac 5D).

The entire system was helium leak-tested by exposing the system, in particular the sealings, to helium gas in order to investigate their integrity. Helium is well suited for leak testing, as it is nonhazardous, inert and has a high mobility and diffusion coefficient. Moreover, it has a low absorption rate concerning the surfaces of the setup and a low abundance in air of 5.24 ppm [Jou04]. The leak rate of the system was measured by Leybold PhoeniXL^{300}dry, a mass spectrometer fixed at $\frac{m}{z} = 4$ Th, operating in counter current mode and the RGA itself used as an in-situ detector, yielding a leak-rate below $10^{-10}\ \frac{\mathrm{mbar \cdot L}}{\mathrm{s}}$.

Subsequently the system was out-baked at 200 °C in order to minimize out gassing from the surfaces and in order to remove condensed water. The temperature was chosen as high as possible in order to optimize this cleaning step.

The desorption rate j of atoms and molecules from the inner surfaces of the vacuum devices is given by [Jou04]

$$j_{\mathrm{des}} = \frac{dN}{dt} = -\nu_0 N \cdot \exp\left(-\frac{E_{\mathrm{des}}}{RT}\right) \qquad ; \qquad \nu_0 = \frac{1}{\tau_0} = 10^{13}\ \mathrm{s}^{-1} \tag{5.19}$$

where ν_0 is the oscillation frequency of particles on the inner surface which own enough kinetic energy E_{kin} to overcome the binding energy E_{des}.
Their mean dwell time τ is given by

$$\tau = \tau_0 \cdot \exp\left(\frac{E_{\text{des}}}{RT}\right) . \tag{5.20}$$

The desorption rate is significantly enhanced by an increase in temperature T. Moreover, the out-baking process reduces the amount of impurities which have diffused into stainless steel components, which outgas during operation.
The out-baking process was optimized by a second turbo molecular pump which was identical in construction with the one previously described.
After baking the system was helium leak-tested below $10^{-10}\,\frac{\text{mbar}\cdot\text{L}}{\text{s}}$ again and reached a pressure range inside the main chamber of $10^{-10} - 10^{-9}$ mbar.

5.4. Sensitivity increase using a cold trap

While detecting trace impurities with a quadrupole mass filter, one crucial problem arises. Because of the low concentration of the component of interest, larger samples are needed in order to enrich the total number of detectable atoms and molecules. However, the Transpector2 mass filter has to be operated under vacuum conditions, as it must not saturate. The limits are given by the ion source $p_{\text{max}}^{\text{ion}} = 6.6 \cdot 10^{-4}$ mbar and the channeltron electron multiplier $p_{\text{max}}^{\text{EM}} = 1.3 \cdot 10^{-5}$ mbar. In order to detect krypton impurities at the ppb level its concentration has to be enhanced.
A cold trap composed of a spring made of a copper tube and a Dewar vessel filled with liquid nitrogen takes care of this problem. Its task is to freeze out the xenon gas while leaving the krypton unaffected. Consequently the concentration of krypton is enhanced and the pressure in the main chamber, which is dominated by the xenon partial pressure, is decreased. Hence the flow rate of sample gas can be increased, leading to a higher detectable amount of krypton in the main chamber. In the following paragraph the thermodynamical processes inside the cold trap are discussed in more detail.

Vapor pressure

Considering only the melting points of both krypton and xenon and the boiling point of nitrogen, both components should freeze out inside the cold trap, as it is visible in table 5.1.

Gas	Bp (K)	Mp (K)	$p_{\text{vapor}}^{T=LN_2}$ (mbar)
N_2	77.4	63.1	10^3
Kr	120.0	116.0	≈ 2
Xe	165.1	161.4	$2.4 \cdot 10^{-3}$
Ar	87.3	83.8	≈ 250
O_2	90.2	54.8	$10^2 - 10^3$
CH_4	111.7	90.1	≈ 10

Table 5.1.: *Selection of melting and boiling points as well as vapor pressures at T=77.3 K. [Jou04] [Leo10] [Pol64]*

As the cold trap is operated under high vacuum conditions, the different vapor pressures at $T = 77.3$ K of the components of the gas mixture are of vital importance, too.

Vapor pressure p_{vapor} is defined as the pressure at which both vapor and liquid phase of a component are in thermodynamic equilibrium. It has a non-linear dependence on temperature T according to the Clausius-Clapeyron relation [Nol06]

$$\frac{dp}{dT} = \frac{\Delta H_\nu}{\Delta V_\nu \cdot T} \tag{5.21}$$

whereas ΔH_ν and ΔV_ν are the enthalpy of vaporization per mole and the volume change due to phase transition, respectively.

According to table 5.1 vapor pressures of krypton and xenon at temperatures of liquid nitrogen are

$$p_{\text{vapor}}^{\text{T=LN}_2}(\text{Kr}) \approx 2\,\text{mbar} \tag{5.22}$$

and

$$p_{\text{vapor}}^{\text{T=LN}_2}(\text{Xe}) = 2.4 \cdot 10^{-3}\,\text{mbar}. \tag{5.23}$$

The overall behavior of vapor pressure according to temperature both for krypton and xenon is shown in figure 5.6.

The difference in vapor pressure enhances the krypton concentration by about three orders of magnitude.

Moreover, the flow rate through the input leak valve is important. Increasing the flow rate does not effect the xenon partial pressure, which stays constant at $2.4 \cdot 10^{-3}$ mbar while the krypton throughput increases, as long as the cold trap is able to freeze up the xenon. This is guaranteed as long as the input pressure between the leak-valve and the cold trap ($p_{\text{in}}^{\text{ITR}} \sim 10^{-1}$ mbar) does not fall below the xenon vapor pressure.

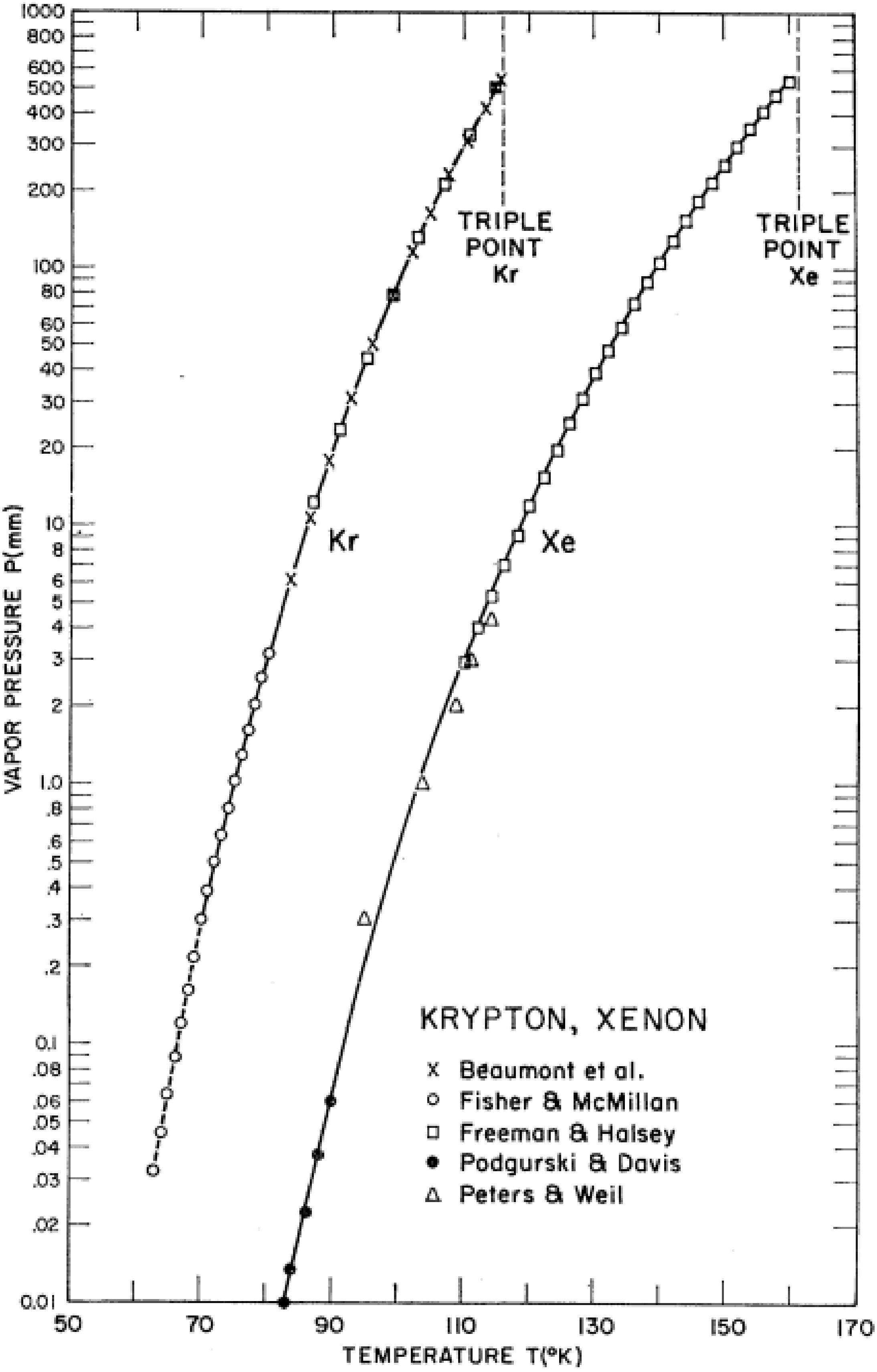

Figure 5.6.: *Vapor pressures of krypton and xenon related to absolute temperature [Pol64].*

5.5. Design of the experimental setup

Taking the mass spectrometry setup described in the bachelor thesis of Andreas Sprenger [Spr09] as a starting point, several components on the system were modified or rather included in addition.

First of all, a second quadrupole mass filter (Transpector2 H200M) which has been described previously was mounted at the main chamber, as the existing mass filter (QuadruVac PGA 100) was not able to measure up to 200 atomic mass units (amu), but only up to 100 amu.

The Transpector2 has a sensitivity of $7.6 \cdot 10^{-5}\,\frac{\mathrm{amps}}{\mathrm{mbar}}$, which can be enhanced by an electron multiplier to $380\,\frac{\mathrm{amps}}{\mathrm{mbar}}$. The resolution $R = \frac{m}{\Delta m}$ is better than 1 amu at 10 % peak height over the entire mass range. This leads to a theoretical minimum detectable partial pressure of $6.6 \cdot 10^{-15}$ mbar [Inf04].

The largest modification was the installation of a cold trap made of a spring of copper and a Dewar vessel filled with liquid nitrogen between the main chamber and the input leak-valve. The copper spring consists of multiple coils which are fully emerged in liquid nitrogen at a constant height. Thus the efficiency of freezing out the xenon is secured and constant over the entire measurement period.

The major components of the experimental setup are shown in figure 5.7.

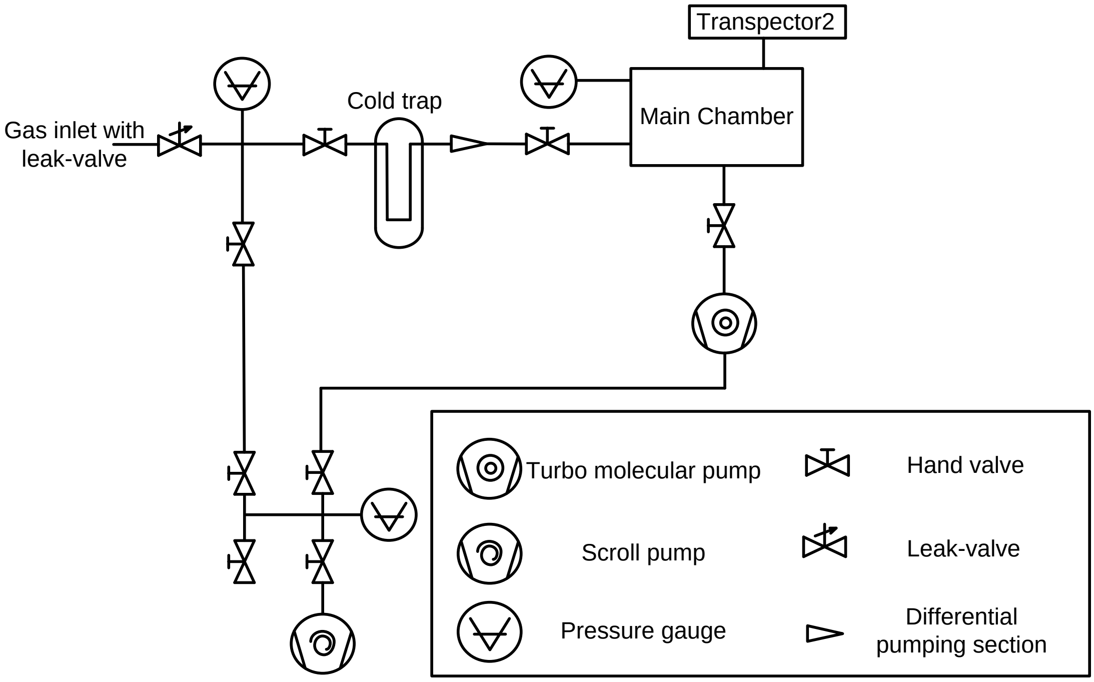

Figure 5.7.: *Schematic drawing of the experimental setup. The sample gas is introduced through a leak-valve and passed towards the cold trap. A low conducting differential pumping section limits the flow into the main chamber where the quadrupole mass filter analyzes the sample composition. Pressures are measured both between the leak-valve and the cold trap (p_{in}^{ITR}) and inside the main chamber (p_{MC}). A photograph of the setup is shown in figure 5.9 at the end of this chapter.*

Xenon samples comprising contaminations of krypton are inserted through a leak-valve (Leybold UHV All-metal variable leak-valve 28990) with a conductivity[4] of $C_{\mathrm{LV}} \sim 10^{-3}\,\frac{\mathrm{L}}{\mathrm{s}}$ and transmitted to the cold trap. The pressure behind the leak-valve $p_{\mathrm{in}}^{\mathrm{ITR}}$ is measured by the IONIVAC ITR 200 S pressure sensor. Inside the cold trap the concentration of krypton in the mixture is enhanced. The following differential low conducting pumping section limits the flow into the main chamber in order to prevent saturation of the mass filter, which analyzes the gas. The pressure inside the main chamber p_{MC} is measured by the IONIVAC IE 514 pressure sensor and in addition by the Transpector2 mass filter itself.

The differential low conducting pumping section (DPS)

The differential low conducting pumping section (DPS) reduces the gas flow into the main chamber. The interplay between the turbo molecular pump and the DPS determines the gas flow through the system. The molecular conductance C of a pipe with length l and diameter d is given by [Jou04]

$$C_{\mathrm{DPS}} = \frac{\pi}{16} \cdot \bar{c} \cdot d^2 \cdot \frac{14 + 4\frac{l}{d}}{14 + 18\frac{l}{d} + 3\left(\frac{l}{d}\right)^2} \tag{5.24}$$

where

$$\bar{c} = \sqrt{\frac{8 \cdot R \cdot T}{\pi \cdot M}} \tag{5.25}$$

is the mean particle velocity.
For xenon and krypton gas with $\mathrm{M_{Xe}}$=131.293 $\frac{\mathrm{g}}{\mathrm{mol}}$ and $\mathrm{M_{Kr}}$=83.798 $\frac{\mathrm{g}}{\mathrm{mol}}$ this leads to a conductance of

$$C_{\mathrm{DPS}}(\mathrm{Xe}) = 7.67 \cdot 10^{-3}\,\frac{\mathrm{L}}{\mathrm{s}} \tag{5.26}$$

and

$$C_{\mathrm{DPS}}(\mathrm{Kr}) = 9.60 \cdot 10^{-3}\,\frac{\mathrm{L}}{\mathrm{s}} \tag{5.27}$$

at the differential low conducting pumping section at $T = 293.15$ K.
Hence the DPS reduces the flow into the main chamber by about two orders of magnitude. For a detailed calculation of the conductivities see chapter A.2 in the appendix.

Proof of molecular flow at the differential pumping section

The type of flow is determined by the Knudsen number Kn, which is defined as

$$Kn = \frac{\lambda}{d} \tag{5.28}$$

where λ describes the mean free path and d a representative physical length scale of the DPS. For this special case the length corresponds to the diameter of the pipe, which is 1 mm at the smallest cross section. Table 5.2 lists the correlation between the Knudsen number and the specific type of flow.

---

[4] The conductivity is estimated according to $q_{\mathrm{pV}} = C \cdot (p_1 - p_2)$ by considering the flow rate normalization presented in chapter 7 without knowing the exact geometry of the leak-valve.

Type of flow	Knudsen number
Free molecular flow	$0.5 \leq Kn$
Intermediate flow	$0.01 \leq Kn \leq 0.5$
Continuum flow	$Kn \leq 0.01$

Table 5.2.: *Correlation between Knudsen number and the type of flow [Jou04].*

The mean free path is given by

$$\lambda = \frac{k_B \cdot T}{\sqrt{2} \cdot \pi \cdot p_{\text{ct}}^{\text{out}} \cdot d_{\text{Molecule}}^2} \tag{5.29}$$

where the particles hard shell diameter d_{Molecule} is assumed to be two times the van der Waals radius r_W [Bon64]

$$r_W(\text{Xe}) = 216\,\text{pm} \quad ; \quad r_W(\text{Kr}) = 202\,\text{pm} \quad ; \quad r_W(\text{He}) = 140\,\text{pm} \tag{5.30}$$

and $p_{\text{ct}}^{\text{out}}$ describes the pressure behind the cold trap, but before the DPS.
The results for the calculated Knudsen numbers Kn are shown in table 5.3. Two cases have been estimated:

i) $p_{\text{ct}}^{\text{out}} = p_{\text{in}}^{\text{ITR}} \sim 10^{-1}$ mbar
The upper part of table 5.3 shows the results for the input pressure between the leak-valve and the cold trap measured by the IONIVAC ITR 200 S pressure sensor normalized to xenon standards. Even under the assumption of an insufficient working cold trap, that is the pressure before the cold trap is the same as behind, the assumption of molecular flow within the DPS used in equation 5.24 is still valid.

ii) $p_{\text{ct}}^{\text{out}} = p_{\text{vapor}}^{\text{Xe}} = 2.4 \cdot 10^{-3}$ mbar
The lower part of table 5.3 shows the results under the assumption of an efficiently working cold trap capable of freezing the overall amount of xenon gas according to the prevailing thermodynamic conditions.

Pressure $p_{\text{ct}}^{\text{out}}$	Element	Mean free path λ	Knudsen number Kn
$1.0 \cdot 10^{-1}$ mbar	Xe	$5.0 \cdot 10^{-4}$ m	0.5
	Kr	$5.7 \cdot 10^{-4}$ m	0.6
	He	$1.2 \cdot 10^{-3}$ m	1.2
$2.4 \cdot 10^{-3}$ mbar	Xe	$2.1 \cdot 10^{-2}$ m	21
	Kr	$2.4 \cdot 10^{-2}$ m	24
	He	$5.0 \cdot 10^{-2}$ m	50

Table 5.3.: *Mean free path λ and corresponding Knudsen numbers Kn for different gas species and input pressures.*

The molecular conductance C of the DPS is related to the pumping speed S of the turbo molecular pump listed in table A.5 by considering both the flow q_{pV} through the DPS and the ambient pressures.

$$q_{pV} = p_{\text{MC}} \cdot S \qquad \text{and} \qquad q_{pV} = C \cdot \underbrace{(p_{\text{ct}}^{\text{out}} - p_{\text{MC}})}_{\approx p_{\text{ct}}^{\text{out}}} \tag{5.31}$$

where p_{MC} is the pressure inside the main chamber near the quadrupole mass filter obtained by the IONIVAC IE 514 pressure sensor and $p_{\text{ct}}^{\text{out}}$ the pressure of the outlet of the cold trap before the DPS.
Assuming an average molecular conductivity of $C \sim 10^{-2}\,\frac{\text{L}}{\text{s}}$ and a mean pressure inside the main chamber of $p_{\text{MC}} = 3 \cdot 10^{-7}$ mbar one obtains

$$p_{\text{ct}}^{\text{out}} = \frac{S \cdot p_{\text{MC}} \cdot k_{\text{Xe}}}{C} \qquad ; \qquad k_{\text{Xe}} = 0.33 \tag{5.32}$$

$$\approx \frac{300\,\frac{L}{s} \cdot 3 \cdot 10^{-7}\,\text{mbar} \cdot 0.33}{10^{-2}\,\frac{L}{s}} \tag{5.33}$$

$$\approx 3.0 \cdot 10^{-3}\,\text{mbar} \tag{5.34}$$

for the pressure between cold trap and DPS, where k_{Xe} is a correction factor taking the dependence on the sort of gas into account. The estimated value of

$$p_{\text{in}}^{\text{ITR}} > 3.0 \cdot 10^{-3}\,\text{mbar} \gtrsim p_{\text{vapor}}^{\text{Xe}} \tag{5.35}$$

lies slightly above to the xenon vapor pressure, as expected.
From the values of the Knudsen number Kn it can be concluded that there is only free molecular flow at the DPS.

5.6. Sample preparation

In order to produce known concentrations of krypton in xenon for calibration purposes a dedicated mixing chamber with three volumes has been orbitally welded with Orbitec Tigtronic Basic[3] and OSK 21G. A schematic sketch of the mixing chamber is visible in figure 5.8. It consists of two equal sized volumes and one which has a three to four times bigger volume separated by high pressure bellow valves (SS-8BG-VCR). This bigger volume is needed in order to dilute krypton efficiently by dividing and expanding gas into the different volumes. The mixing chamber also comprises a pressure gauge which works independent of the sort of gas (MKS Baratron 121 A). This Baratron is able to measure the pressures in the range from 10 bar to 1 mbar with an accuracy of 0.5 %. Firstly, the Baratron is used to determine the exact volume ratios of the mixing chamber and secondly, it offers the opportunity to monitor the pressure and the flow rate during the measurements.
The Baraton pressure sensor directly measures the pressure p by the force per unit area

$$p = \frac{F}{A} = \frac{1}{A} \cdot \sum_i \dot{p}_i \quad . \tag{5.36}$$

In comparison to this technique, other pressure gauges (IONIVAC etc.) measure the conductivity C, which is proportional to the number of particles N_i per volume element

$$C \sim \frac{1}{V} \cdot \sum_i N_i \quad . \tag{5.37}$$

Therefore the Baratron does not depend on the type of gas, while other sensors do.

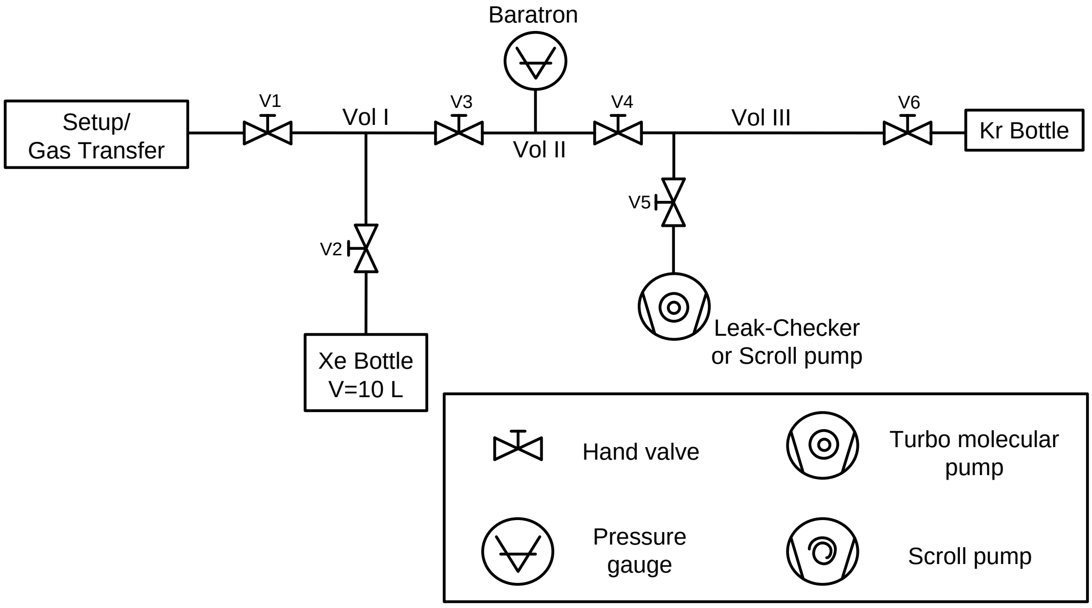

Figure 5.8.: *Schematic sketch of the dedicated mixing chamber. Volumes I and II are of equal size, while volume III is about 3.7 times larger. The pressure is recorded by a Baratron pressure sensor connected to volume II.*

Xenon doping

Artificial xenon doping within the dedicated mixing chamber shown in figure 5.8 is performed as follows: Xenon gas with a known pressure of 2 bar is inserted from a 10 L reservoir into volume I. Krypton is inserted into volume II and III with a pressure of about 500 mbar. Afterwards volume III is pumped down to $\sim 10^{-3}$ mbar while the valve to volume II is closed. Then krypton is expanded from volume II into volume III. Volume III is evacuated again and the volume divisions are repeated until the krypton pressure exceeds the threshold of the Baratron range of 1 mbar. In the next step xenon from volume I and krypton from volume II are mixed and afterwards transmitted into the system through the leak-valve which is connected to the outer valve of volume I. Volumes I and II and the connection to the leak valve have a combined volume of about 60 $\text{cm}^3 = 0.06$ L.

By this method dilutions of the order of $\frac{1}{1000}$ can be produced. In order to achieve lower concentrations some of the mixed gas which has been transmitted to the setup has to be kept. At a pressure recording of the Baratron of $50-100$ mbar the valve separating volume I and II must be closed. The remaining mixture of krypton and xenon in volume II is then several times expanded into the evacuated volume III, in the same way previously described. It is assumed that the partial pressure of krypton scales accordingly to the total pressure, which is reduced due to the expansions between volume II and III.

The mixture residing in volume II can then again be mixed the pure xenon filled in volume I. Hence the concentration is given by the partial pressure of krypton divided by the total pressure in the two volumes.

All of these dividing and mixing processes are monitored by the Baratron, which is mounted at the centered volume.

The total setup during operation can be seen in figure 5.9.

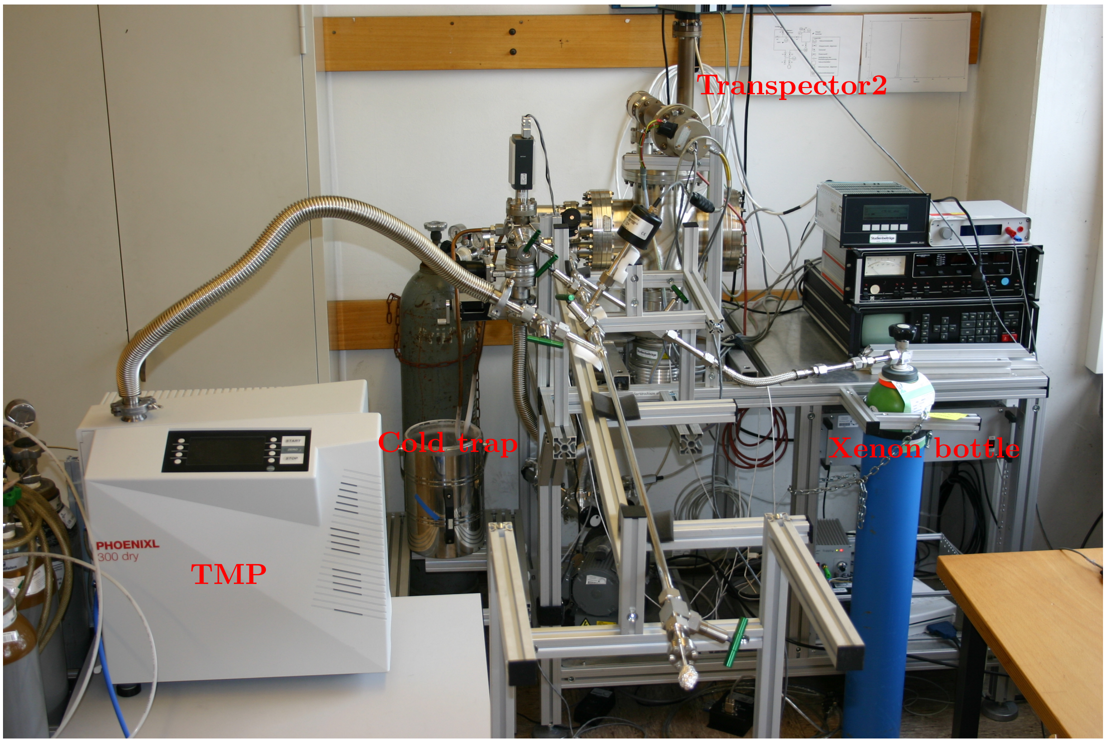

Figure 5.9.: *Photo of the setup taken during operation. The dedicated mixing chamber can be seen in the foreground. On the left and right hand side are the turbo molecular pump (TMP) and the storage bottle with xenon gas, respectively. The main setup comprising the cold trap, the vacuum chamber and the quadrupole mass filter (Transpector2) is visible in the background.*

6. Calibration

In this and the following two chapters the results from the krypton in xenon measurements are presented.
First of all, results from calibration are discussed, starting with a precise determination of the volume ratios of the dedicated mixing chamber and the corresponding dilution ratios, which are of crucial importance for mixing known amounts of krypton into the xenon.
Moreover, some uncertainties of the Transpector2 such as mass drift are analyzed.

6.1. Determination of the dilution ratios of the mixing chamber

A precise determination of the volume ratios of the dedicated mixing chamber has been done at the beginning of the experiment. The calibration was performed with nitrogen gas similar to the previously described mixing method according to the principle of *statistical expansion* [Knu10].
The following three assumptions have to be satisfied in order to use the method of statistical expansion [Jou04]:

i) The starting pressure has to be at least two orders of magnitude higher than the pressure of the residual gas.
This assumption is fulfilled, as the ratio is at least of the order of 10^2. Nevertheless, the corresponding approximation in equation 6.5 accounts for this effect with an uncertainty of the order of a percent.

ii) Out-gassing of the mixing chamber must not cause a significant rise in pressure within the time of operation.
As the calibration only affects medium vacuum, this effect can be neglected.

iii) Surfaces of the mixing chamber must not absorb significant amounts of calibration gas.
This effect becomes dominant for nitrogen gas at a pressure of 10^{-8} mbar, which is by far not reached during the calibration.

Statistical expansion principle

The mixing chamber is evacuated down to $p \sim 10^{-2}$ mbar. Afterwards one volume is filled with nitrogen. The gas is then expanded into one of the evacuated volumes by opening the valve in between and the change in pressure is recorded by the Baratron. Afterwards the volumes of the mixing chamber are evacuated again and the volume division is repeated. The use of nitrogen instead of krypton or xenon gas does not effect the calibration, as the dilution does not depend on the sort of gas and above all the Baratron measures the pressure independently of the sort of gas.
Without loss of generality only volume I and II are considered for the derivation of the dilution factors of the dedicated mixing chamber.

Applying the ideal gas law[1] to the volumes of the mixing chamber one obtains

$$V_{\mathrm{I}} = \frac{N_{\mathrm{I}} k_B T}{p_{\mathrm{I}}} \quad ; \quad V_{\mathrm{II}} = \frac{N_{\mathrm{II}} k_B T}{p_{\mathrm{II}}} \tag{6.1}$$

for two different volumes I and II and

$$V_{\mathrm{I+II}} = \frac{(N_{\mathrm{I}} + N_{\mathrm{II}}) \cdot k_B T}{p_{\mathrm{I+II}}} \tag{6.2}$$

for the combined volume I+II, where $p_{\mathrm{I+II}}$ is the pressure both in volume I and II after the expansion.

The dilution ratio due to expansion from one volume into the other one is given by the *expansion ratio*:

$$\frac{V_{\mathrm{I}}}{V_{\mathrm{I+II}}} = \frac{\frac{N_{\mathrm{I}} k_B T}{p_{\mathrm{I}}}}{\frac{(N_{\mathrm{I}}+N_{\mathrm{II}}) \cdot k_B T}{p_{\mathrm{I+II}}}} \tag{6.3}$$

$$= \frac{N_{\mathrm{I}} k_B T}{p_{\mathrm{I}}} \cdot \frac{p_{\mathrm{I+II}}}{(N_{\mathrm{I}+} N_{\mathrm{II}}) \cdot k_B T} \tag{6.4}$$

$$= \frac{N_{\mathrm{I}}}{N_{\mathrm{I}} + N_{II}} \cdot \frac{p_{\mathrm{I+II}}}{p_I} \quad ; \quad N_{\mathrm{I}} \gg N_{\mathrm{II}} \tag{6.5}$$

$$\approx \frac{p_{\mathrm{I+II}}}{p_{\mathrm{I}}} \tag{6.6}$$

The approximation $N_{\mathrm{I}} \gg N_{\mathrm{II}}$ in the worst case[2] introduces an error of the order of a percent due to the residual gas in volume II, depending on the duration of pumping period and the applied pump.

The uncertainty of the Baratron was conservatively assumed to be ±5 mbar instead of 0.5 % of the reading to take into account both temperature and display fluctuations as well as the previously mentioned approximation.

The results of the volume ratio calibration are visible in table 6.1 as well as in figures 6.1 and 6.2. The pressure of the volume of interest can be seen on the x-axis. On the y-axis the resulting pressure after expansion of the gas into the evacuated adjoined volume is shown.

Dilution Ratio	Dilution factor
I / II	0.505 ± 0.001
II / I	0.490 ± 0.001
II / III	0.268 ± 0.001
III / II	0.730 ± 0.001

Table 6.1.: *Calibration results from the dedicated mixing chamber for the dilution ratios of adjoint volumes.*

Because of the design of the mixing chamber and the position of the turbo molecular pump, the dilution factor of volume II/I was not determined with the same statistics as

---

[1] According to [Jou04] the ideal gas law is valid up to pressures $p \lesssim 300$ kPa = 3 bar for noble gases and nitrogen.

[2] $\frac{\text{final pressure of Scroll Vac}}{p_{\min}\text{ before expansion}} = \frac{5 \cdot 10^{-2}\ \text{mbar}}{2\ \text{mbar}} \sim \mathcal{O}\left(\frac{1}{100}\right)$

the other ratios. As the sum of the two corresponding dilution ratios should equal **1**, the quality of this calibration can be estimated.

$$\frac{V_{\mathrm{I}}}{V_{\mathrm{I+II}}} + \frac{V_{\mathrm{II}}}{V_{\mathrm{I+II}}} = 1 \tag{6.7}$$

$$0.505 \pm 9.6 \cdot 10^{-4} + 0.490 \pm 1.0 \cdot 10^{-3} = 0.995 \pm 1.37 \cdot 10^{-3} \approx 1$$

$$0.268 \pm 8.8 \cdot 10^{-4} + 0.730 \pm 1.4 \cdot 10^{-3} = 0.998 \pm 1.65 \cdot 10^{-3} \approx 1$$

As the sum of the dilution factors does not exactly match up to unity within the error bars, some so far unknown systematic uncertainties might be present. For example opening and closing the valve between the mixing volumes might have an effect due to the blocked volume in the per mill range. Moreover, higher statistics of the dilution factor for expanding from volume II into volume I could solve the discrepancy.

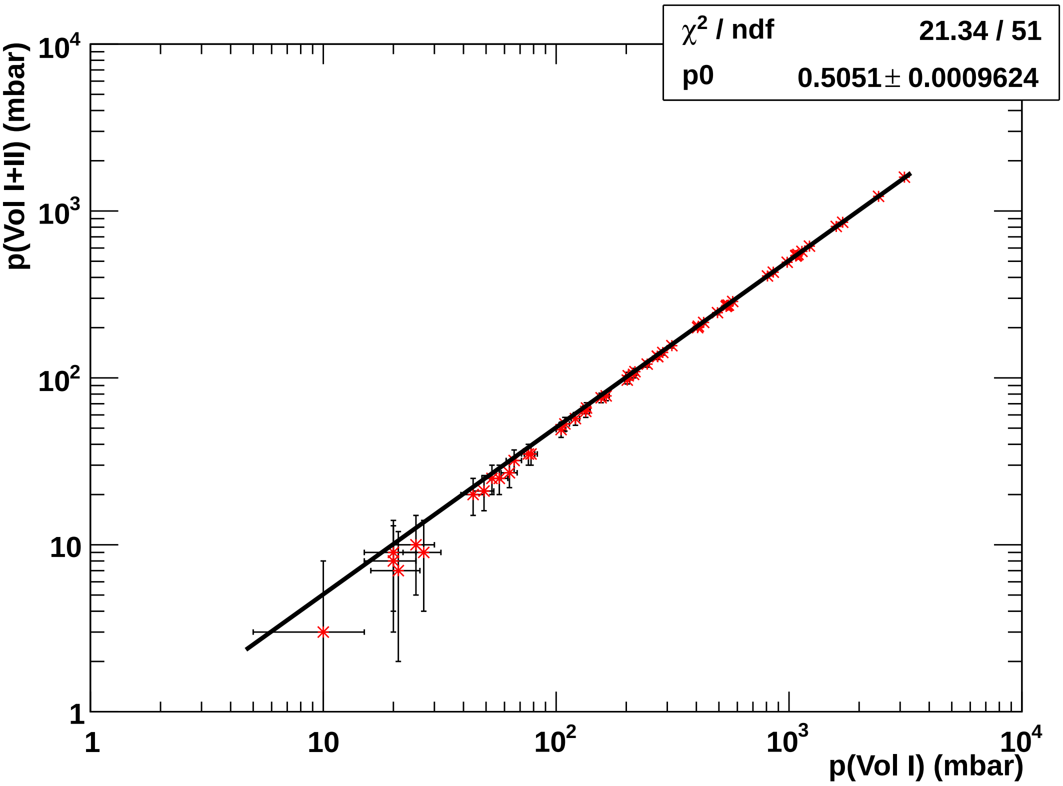

(a) Dilution ratio of expansion from volume I into volume II.

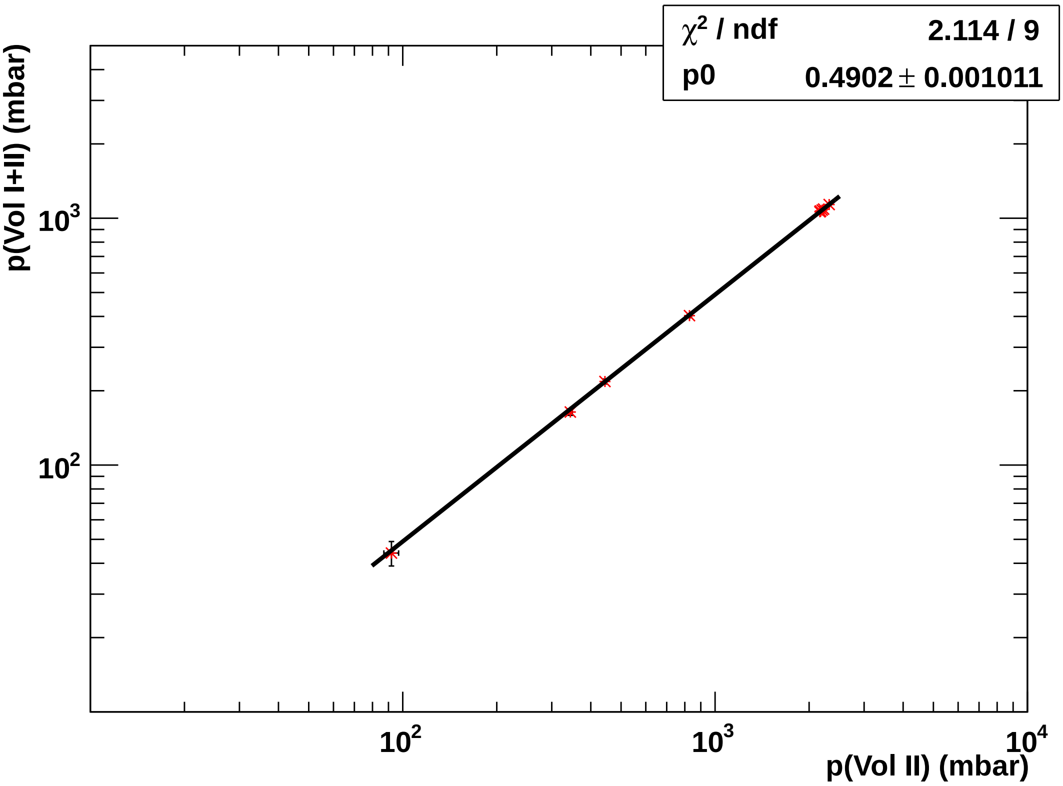

(b) Dilution ratio of expansion from volume II into volume I.

Figure 6.1.: *Dilution ratio calibration of the dedicated mixing chamber concerning volumes I and II. The x- and y-axes indicate the pressure recorded by the Baratron before and after the expansion, respectively. Some error bars protrude from the plot as they approach zero at low pressures.*

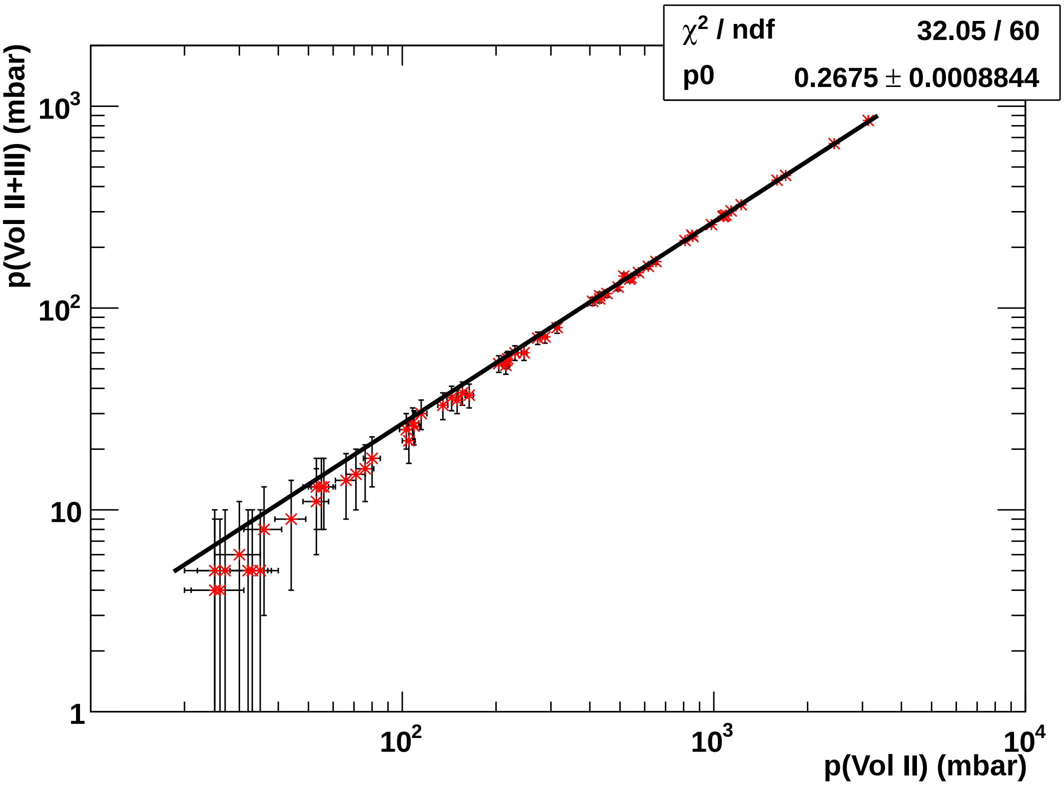

(a) Dilution ratio of expansion from volume II into volume III.

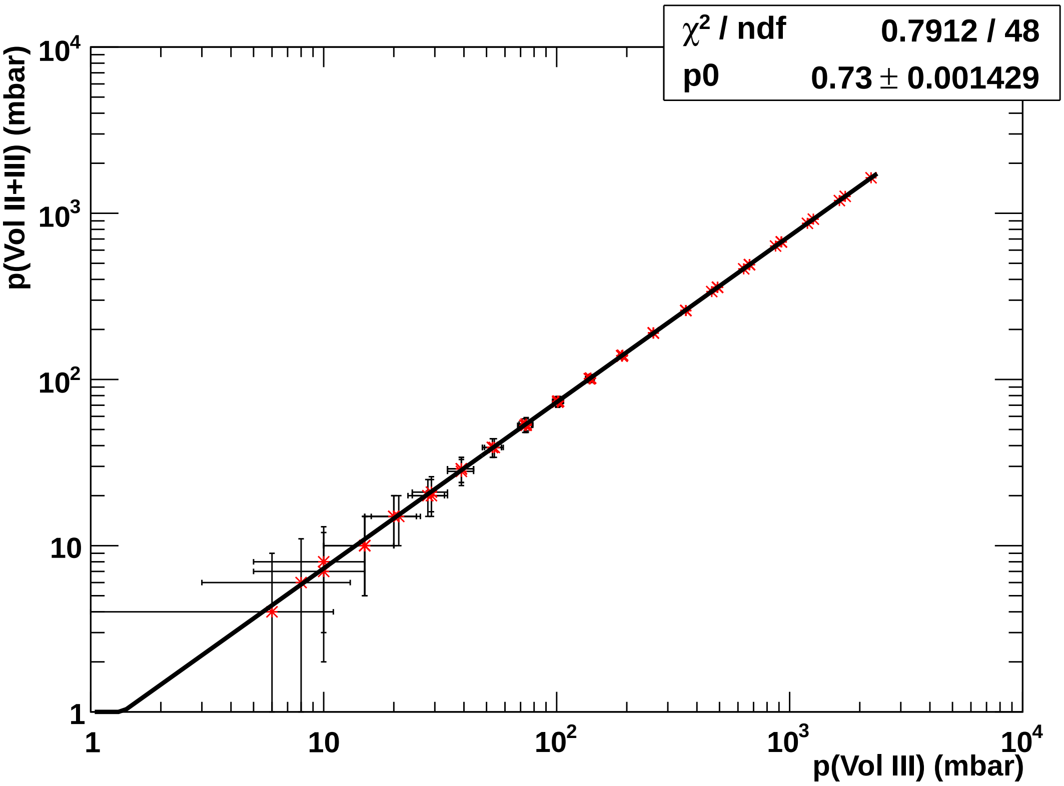

(b) Dilution ratio of expansion from volume III into volume II.

Figure 6.2.: *Dilution ratio calibration of the dedicated mixing chamber concerning volumes II and III. The x- and y-axes indicate the pressure recorded by the Baratron before and after the expansion, respectively. Some error bars protrude from the plot as they approach zero at low pressures.*

6.2. Determination of peak width and position

One of the known uncertainties of a quadruple mass filter is a peak shift in the mass spectrum on the $\frac{m}{z}$ axis. This possible shift is investigated by considering the base peaks of all measurements, namely the intensity of ^{84}Kr by averaging over the measured currents at the signal region after a measuring time of $t \in [150; 200]$ seconds. Exploring the other krypton peaks as well, does not lead to additional information, as these would exhibit the same shift, if present.

As the peaks in a mass spectrum have a Gaussian distribution it is appropriate to determine the mean value of a Gaussian fit of the measured currents, which are recorded with five data points per atomic mass unit (amu). The investigated derivations of $\frac{m}{z} = 84$ Th from these values are shown in table 6.2 and figure 6.3.

Run Number	$c\left(\frac{\text{Kr}}{\text{Xe}}\right)$	Base peak mean $\left(\frac{m}{z}\right)$	Peak width (amu)
5-01	$1.70 \cdot 10^{-5}$	84.03 ± 0.05	0.25 ± 0.04
5-02	$2.50 \cdot 10^{-6}$	84.02 ± 0.05	0.25 ± 0.04
5-03	$3.35 \cdot 10^{-7}$	84.02 ± 0.05	0.25 ± 0.04
5-04	$4.40 \cdot 10^{-8}$	84.04 ± 0.05	0.25 ± 0.05
5-06	$3.06 \cdot 10^{-5}$	83.99 ± 0.05	0.25 ± 0.04
5-07	$4.14 \cdot 10^{-6}$	83.99 ± 0.06	0.25 ± 0.04
5-08	$5.53 \cdot 10^{-7}$	84.02 ± 0.05	0.26 ± 0.04
5-09	$7.35 \cdot 10^{-8}$	84.02 ± 0.05	0.25 ± 0.04
5-10	$3.48 \cdot 10^{-8}$	84.03 ± 0.04	0.22 ± 0.03
5-11	$1.73 \cdot 10^{-8}$	84.01 ± 0.04	0.28 ± 0.04
6-01	$8.81 \cdot 10^{-6}$	83.95 ± 0.05	0.25 ± 0.05
6-02	$1.14 \cdot 10^{-6}$	84.00 ± 0.06	0.26 ± 0.04
6-03	$1.51 \cdot 10^{-7}$	84.02 ± 0.06	0.26 ± 0.05
6-04	$1.99 \cdot 10^{-8}$	84.08 ± 0.06	0.39 ± 0.08
7-01	$9.02 \cdot 10^{-6}$	84.01 ± 0.06	0.27 ± 0.05
7-03	$1.54 \cdot 10^{-7}$	84.00 ± 0.06	0.28 ± 0.05
7-04	$2.03 \cdot 10^{-8}$	84.03 ± 0.05	0.28 ± 0.05
7-05	Pure xenon	84.09 ± 0.05	0.27 ± 0.05
7-06	Pure xenon	83.95 ± 0.05	0.29 ± 0.05
7-07	Pure xenon	84.01 ± 0.09	0.28 ± 0.05
7-08	Pure xenon	84.00 ± 0.05	0.30 ± 0.05
7-09	Pure xenon	84.00 ± 0.05	0.30 ± 0.05
7-11	Pure xenon	84.11 ± 0.05	0.23 ± 0.04

Table 6.2.: *Position and width of all base peaks determined by a Gaussian distribution of five parts per atomic mass unit (amu). All graphs can be found in the appendix under section A.7. Runs 1 to 4, which are not listed, have been done in order to optimize the experiment. Run 5 to 7 have been accomplished under the same experimental conditions while run 6 and 7 are discussed in detail in the next chapter.*

It can be seen that the base peaks on average are not shifted during the entire experiment within the error bars. The two counts beyond $\frac{m}{z} = 84.1$ Th are acceptable as the next recorded atomic mass unit is at $\frac{m}{z} = 84.2$ Th.

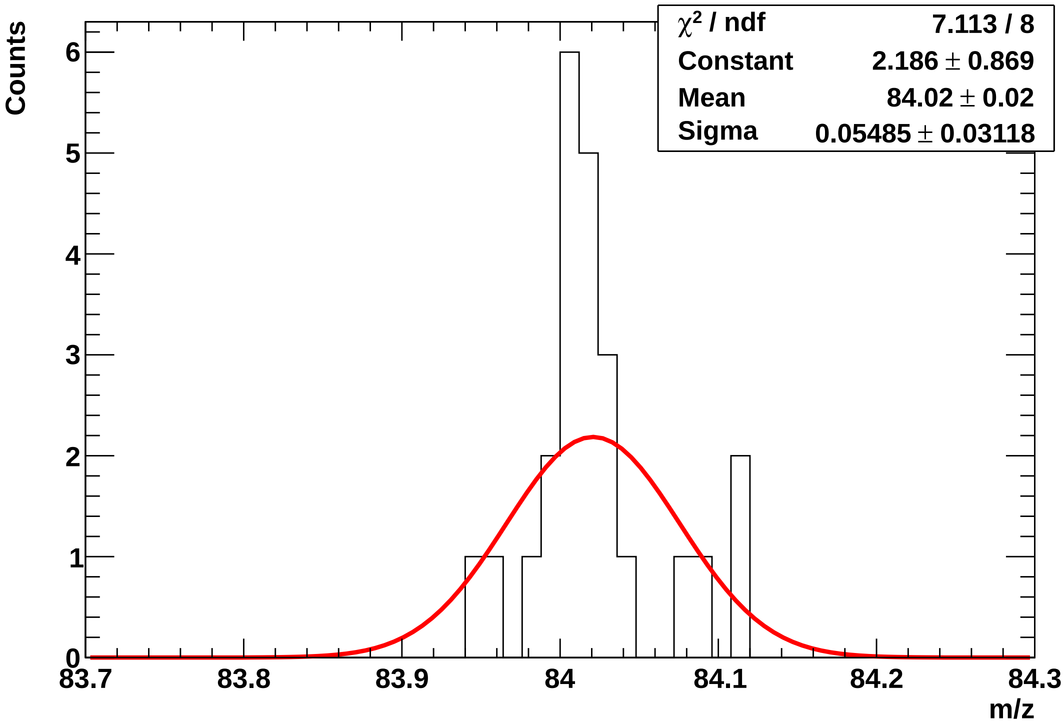

Figure 6.3.: *Histogram of all base peak means listed in table 6.2. The greatest shift of* +0.1 *atomic mass units is far away from the next recorded data point at 84.2 amu.*

6.3. Determination of optimal peak integration

Although five measurement points are taken per atomic mass unit it is possible to consider only three parts per atomic mass unit (ppamu) for each peak integration. This becomes important in further analysis as five ppamu lead to higher statistics, but entail the disadvantage of possible leakage of neighboring peaks and, consequently, a smaller signal to background ratio. In order to obtain the optimum number of points for the integration of the measured currents the signal to background ratio for three and five ppamu is calculated within the signal region. The measured currents at $\frac{m}{z} = 85$ Th are associated with the background[3].

Using $\frac{m}{z} = 85$ Th as a background signal, the signal to background ratios for all krypton isotopes have been estimated. The obtained ratios strongly depend both on the artificially doped krypton concentration and on the natural abundance of each specific krypton isotope. In order to minimize these dependences the ratio of the corresponding signal to background ratios of three and five ppamu is analyzed. The results of the signal to background ratios for three and five ppamu are summarized in figure 6.4.

The peaks around the ratios of 4.5, 9 and 10.5 in figure 6.4(a) correspond to high levels of doping at the ppm level which cause a high signal to background ratio.

As signal to background ratios at the ppm level are of minor interest, figure 6.4(b) shows the ratios of the signal to background ratios within the interval [0;3] for three and five ppamu in more detail. It can be seen that the mean of the distribution is shifted to values greater than **1**. Therefore the signal to background ratio favors an integration over three parts per atomic mass units instead of five.

6.4. Estimation of krypton background

The Krypton ratio in ambient air is 1.14 ppm [Wil09]. In a vacuum of $\sim 10^{-9}$ mbar the krypton background is consequently less than $1.14 \cdot 10^{-15}$.

This fraction is orders of magnitude below the detection limit of the quadrupole mass filter and can therefore be neglected.

---

[3] To a good approximation $\frac{m}{z} = 85$ Th can be used as a background reference, as the natural abundance of $\frac{^{\mathrm{nat}}\mathrm{Kr}}{^{85}\mathrm{Kr}} \sim 1.5 \cdot 10^{-11}$ only accounts for a marginal signal which is below the sensitivity of the applied technique. Further details are discussed in section 7.3.

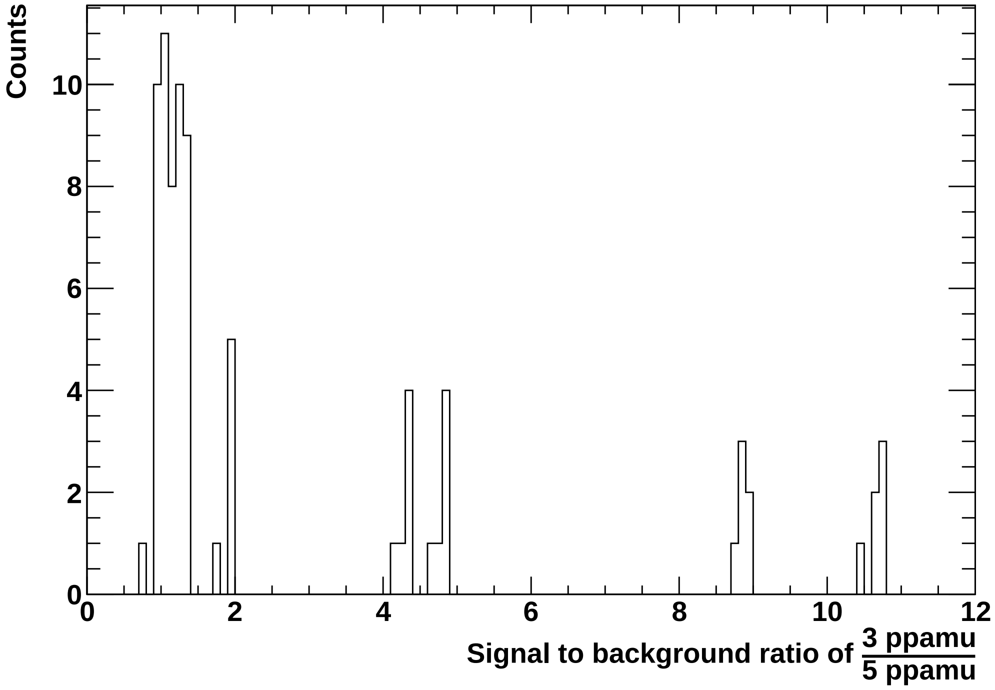

(a) Signal to background ratios of three and five parts per atomic mass unit. In order to compare these two integration intervals the ratios of $\frac{3\mathrm{ppamu}}{5\mathrm{ppamu}}$ are shown. The peaks at values greater than **4** correspond to high doping concentrations at the ppm level.

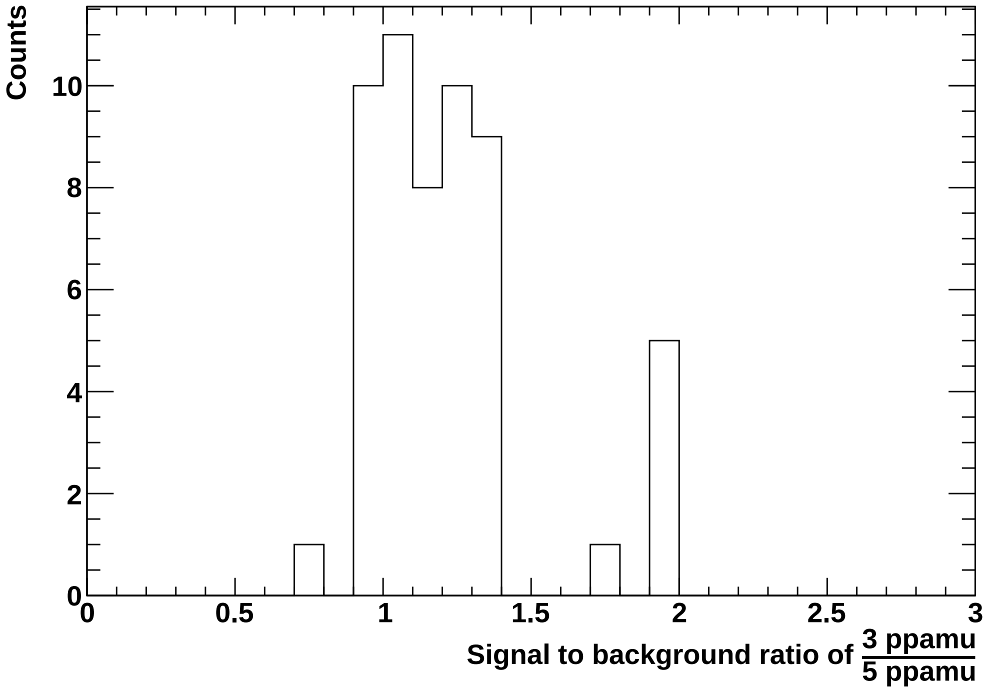

(b) Fraction of signal to background ratios of $\frac{3\mathrm{ppamu}}{5\mathrm{ppamu}}$ within the interval [0;3]. The distribution is shifted to values greater than **1**, favoring an integration over three parts per atomic mass unit.

Figure 6.4.: *Determination of optimal peak integration by comparing the signal to background ratios at three and five parts per atomic mass unit. Figure (b) shows the interval [0;3] of figure (a) in more detail.*

7. Experimental results from the CT-MS measurements

In this section the described technique of CT-MS is used in order to determine trace krypton concentrations in xenon.

Determination of the sensitivity of the setup takes advantage of the relative isotopic abundance of the different krypton isotopes shown in table A.4.

Furthermore, limits on the fraction of krypton in commercially bought xenon from *Air Liquide* are given.

In order to determine the fraction of ^{85}Kr in xenon the signal from ^{84}Kr is measured and projected with respect to the isotopic ratio given in equation 3.4.

7.1. Time evolution of krypton signals

Each measurement starts with supplying liquid nitrogen to the cold trap and setting the quadrupole mass filter to the scanning range of $\frac{m}{z} \in [77; 87]$ Th. This particular scan window offers the opportunity of both recording all krypton isotopes existing in nature and taking benefit of a fast sampling rate, as $\frac{m}{z}$ regions of minor interest are neglected. Furthermore, the reduction to a $\frac{m}{z}$ range where only trace amounts of detectable atoms and molecules are expected provides an additional enhancement of the measuring technique. As only a small number of ions passes the mass filter, the current measured by the detector is substantially low. Therefore the detector and the preamplifier are to some extend protected from damage due to over pressure. The maximum operating pressure is consequently limited by the maximum pressure range of the filament of the ion source filament and the mean free path of the ions which pass the quadrupole mass filter.

Unless otherwise indicated, all samples are introduced after a measuring period of 100 seconds in order to compare the arising krypton signal with the background which is recorded beforehand.

The samples are introduced through a leak-valve. In order to maintain the same conductivity and therefore the same flow rate in each measurement an additional bellow hand valve (SS-8BG-VCR) separating the leak-valve from the dedicated mixing chamber is placed in between. Hence the position of the leak valve is not changed at all. The hand valve is opened at $t = 100$ s.

After a small time delay of $20 - 50$ seconds the signals of the different krypton isotopes start to show up.

The current signals of the krypton isotopes recorded by the quadrupole mass filter are integrated over three parts per atomic mass unit as proposed in chapter 6.3 and plotted versus time. In figures 7.1 to 7.4 the time evolution of the isotopic pattern of krypton for different artificially doped krypton concentrations is shown.

After a small time delay the krypton signals arise sharply, and then decrease continually. This reduction of the signal is caused by a decreasing input flow rate. As only a finite amount of sample gas is used, the flow rate decreases according to the pressure in the sample volume. The “knee” at the end after about 100 seconds of measuring time ($t \sim 200$ s) is due to closing the hand-valve again.

The different measured current values correspond to the isotopic fractions of krypton and are further discussed in section 7.1.2. Krypton concentrations at the ppm level have an extra bump before the signal decrease initiates. The origin of this bump is so far unknown.

The pressure inside the main chamber measured both by the quadrupole mass filter and the IONVAC pressure gauge rises almost instantaneously after opening the leak-valve without showing a time delay. This is unexpected, as krypton propagates faster through the system than xenon, as discussed in chapter 5.5. A possible explanation might be that some part of the xenon bulk passes the cold trap unattached at the beginning of the measurement. This cannot be proven by the mass filter as firstly, only the mass range of krypton is observed and secondly, an observation of the mass range of xenon likely causes currents beyond the current limit of the detector.

Another reason might be the presence of an additional contamination in the xenon, which has a lower boiling/melting point or rather a higher vapor pressure at 77 kelvin. This case will be discussed in more detail in chapter 8.3.

The cold trap is emptied by removing the liquid nitrogen after each measurement and the entire system is pumped until no xenon signal is recored at the quadrupole mass filter. This guarantees that no residual krypton contaminates the following measurement. On average one full measuring cycle comprising four to five different measurements can be performed per day.

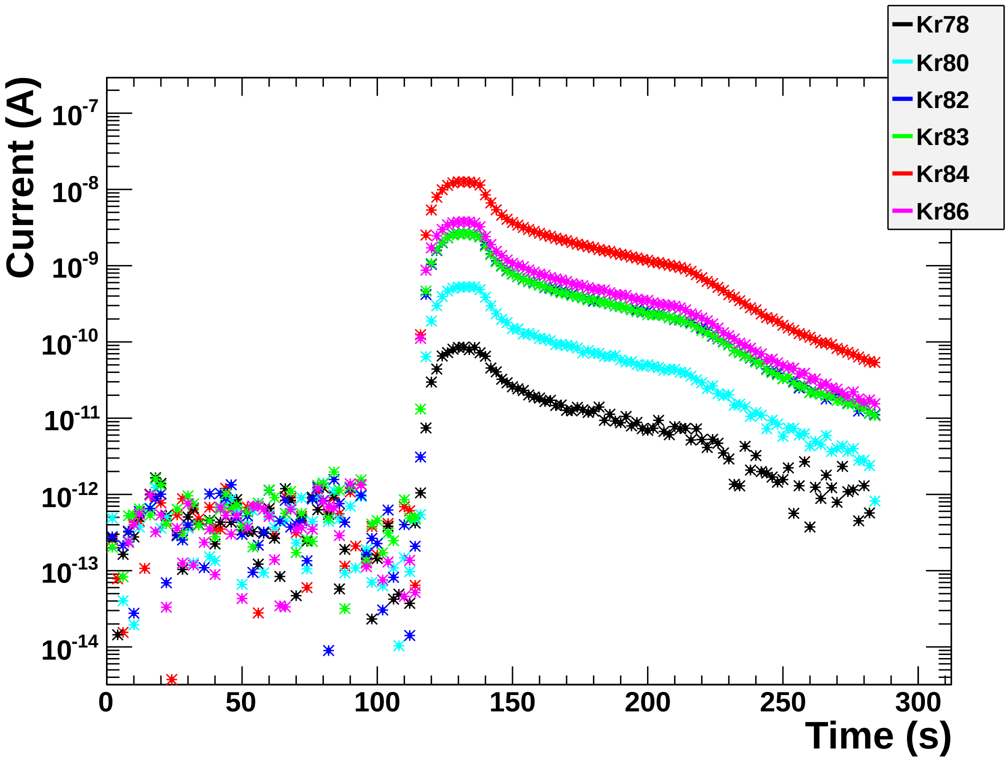

Figure 7.1.: *Time evolution of krypton isotopes at* (8800 ± 282) *ppb* $\frac{Kr}{Xe}$ *(Run 6-01).*

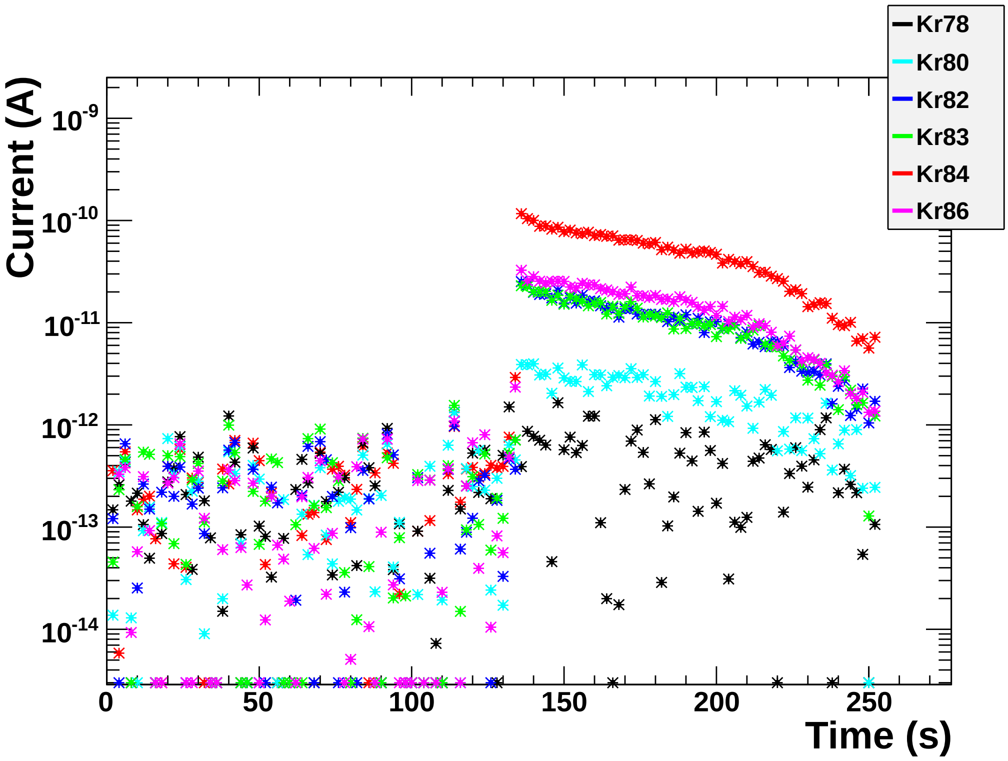

Figure 7.2.: *Time evolution of krypton isotopes at* (1100 ± 41) *ppb* $\frac{Kr}{Xe}$ *(Run 6-02).*

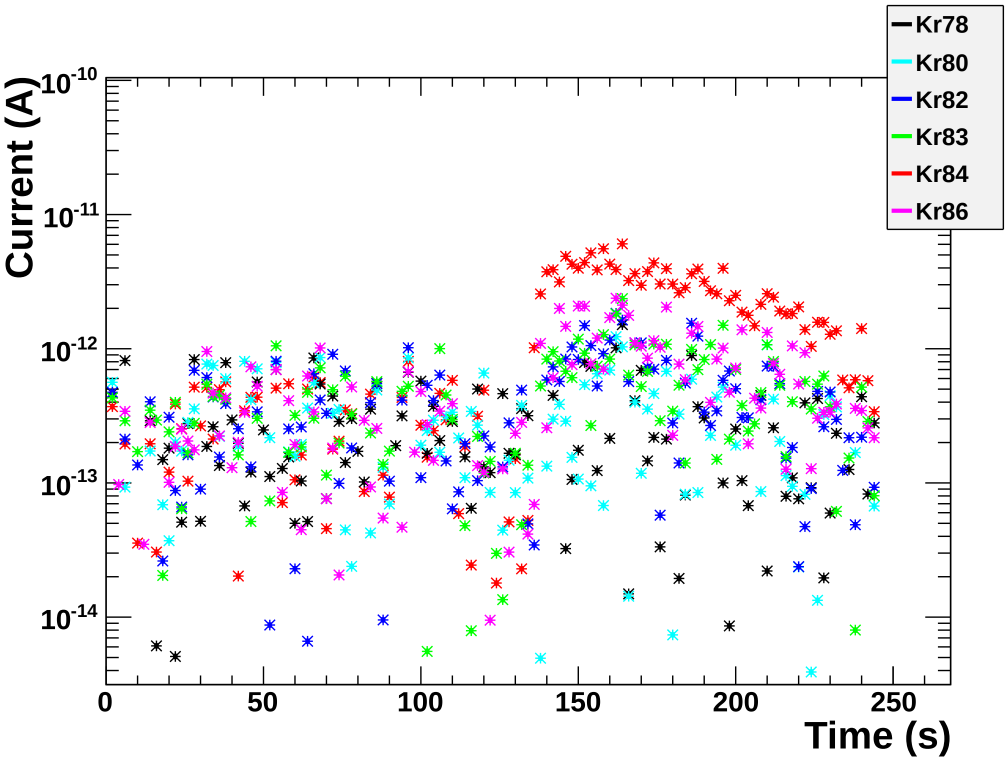

Figure 7.3.: *Time evolution of krypton isotopes at* (150 ± 6) *ppb* $\frac{Kr}{Xe}$ *(Run 6-03).*

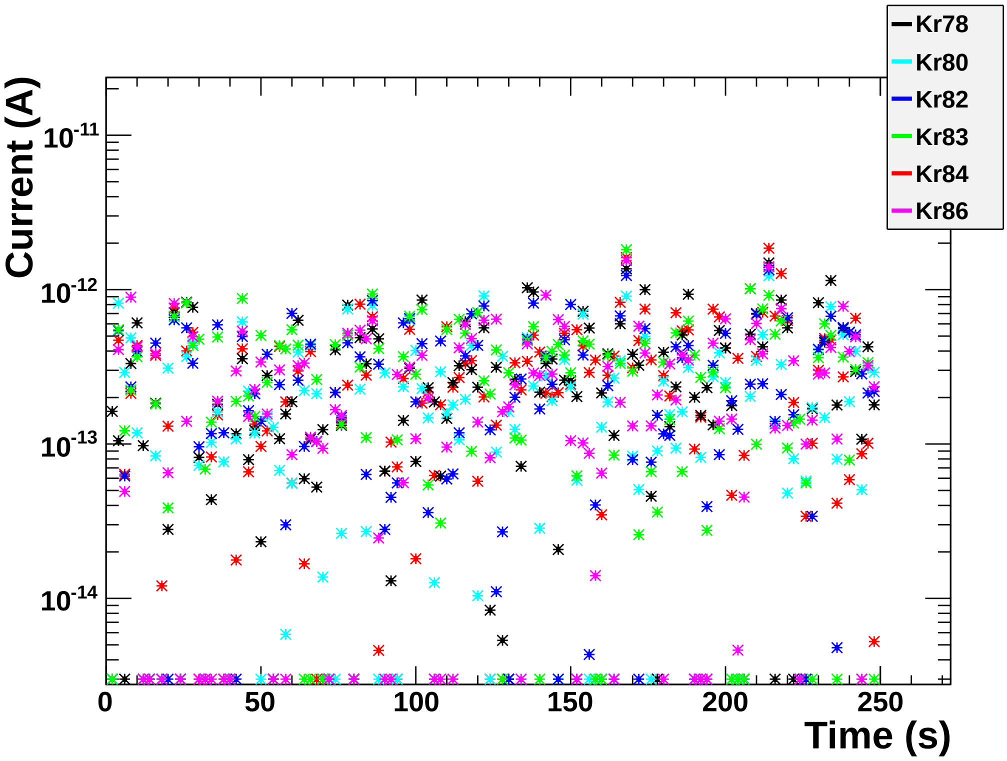

Figure 7.4.: *Time evolution of krypton isotopes at* (20 ± 1) *ppb* $\frac{Kr}{Xe}$ *(Run 6-04).*

7.1.1. Normalizing by flow rate

As already mentioned the current measured by the quadrupole mass filter decreases over time due to a decreasing flow rate. The flow rate is directly proportional to the change in pressure per time interval $\frac{dp}{dt}$ within the sample volume. This pressure decrease is recorded with high precision by the Baratron pressure sensor, which is connected to the sample volume. Therefore the time evolution of the measured current values of krypton can be normalized by flow rate in order to unify the recorded signals. The decrease over time of the measured current consequently flattens out as can be seen in figures 7.5 to 7.8. A slight decrease remains at krypton concentrations of a few ppm. In the following, this long and flat slope will be referred to as the *plateau*.

Furthermore, the recorded pressures inside the sample volume of the dedicated mixing chamber and inside the main chamber where the quadrupole mass filter is mounted are shown as well. The pressure in the sample volume measured by the Baratron is indicated in yellow. Its decrease over time is directly proportional to the flow rate. The pressure inside the main chamber is simultaneously measured by two pressure gauges. On the one hand the Transpector2 provides an in-situ pressure measurement indicated in pale blue colors. However, the sensitivity of this pressure gauge is rather low and can therefore in most cases only be seen right after introducing the sample. On the other hand a more sensitive IONIVAC pressure gauge (p_{MC}) indicated in brown colors measures the pressure inside the main chamber normalized to xenon equivalent, in order to account for the dependence on the gas species.

The pressure measured by the Transpector2 and the IONIVAC pressure gauge can directly be seen after introducing the sample, but before signals from krypton isotopes arise. The pressure rises sharply and decreases slightly before adopting the slope of the krypton signal. Evidence of this can be found in figure 7.5, where the total pressure also has a small bump at $t \in [130; 150]$ seconds, according to the krypton signals. As time progresses, the pressure asymptotically reaches a constant value. This can be interpreted as the contribution of the constant vapor pressure of xenon being present even after closing the leak-valve.

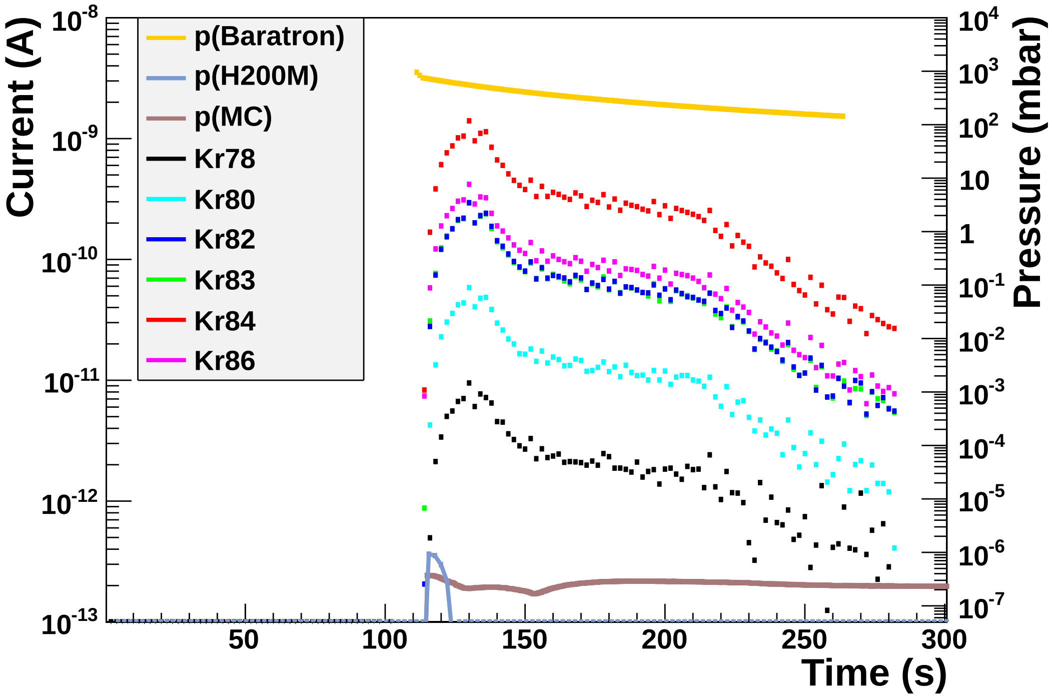

Figure 7.5.: *Time evolution of krypton isotopes normalized by flow rate at* (8800 ± 282) *ppb* $\frac{Kr}{Xe}$ *(Run 6-01).*

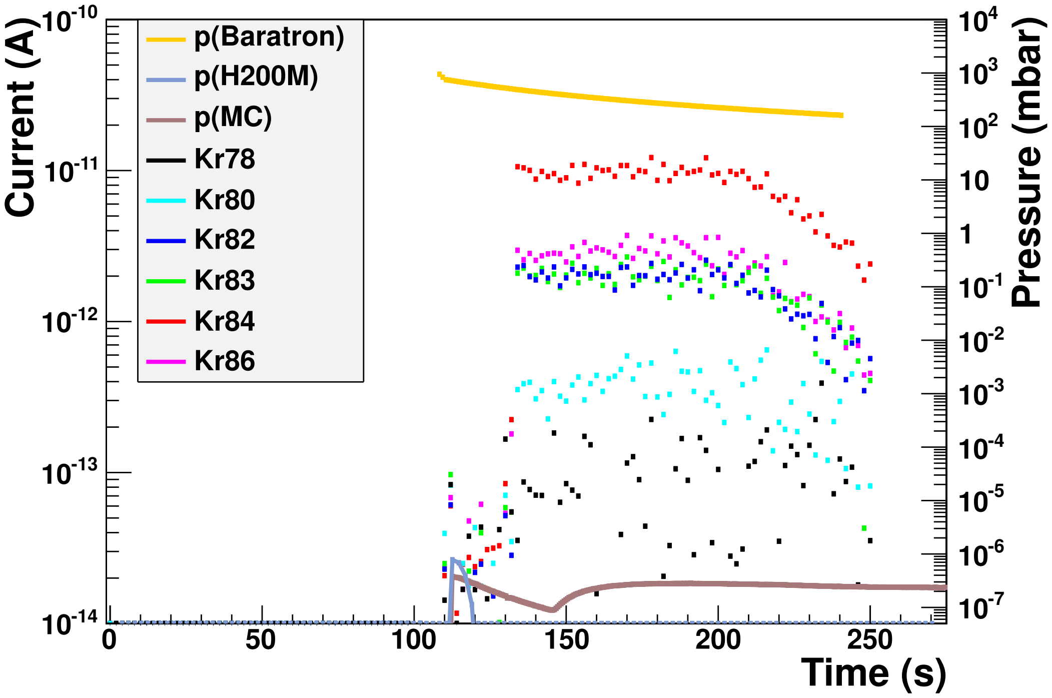

Figure 7.6.: *Time evolution of krypton isotopes normalized by flow rate at* (1100 ± 41) *ppb* $\frac{Kr}{Xe}$ *(Run 6-02).*

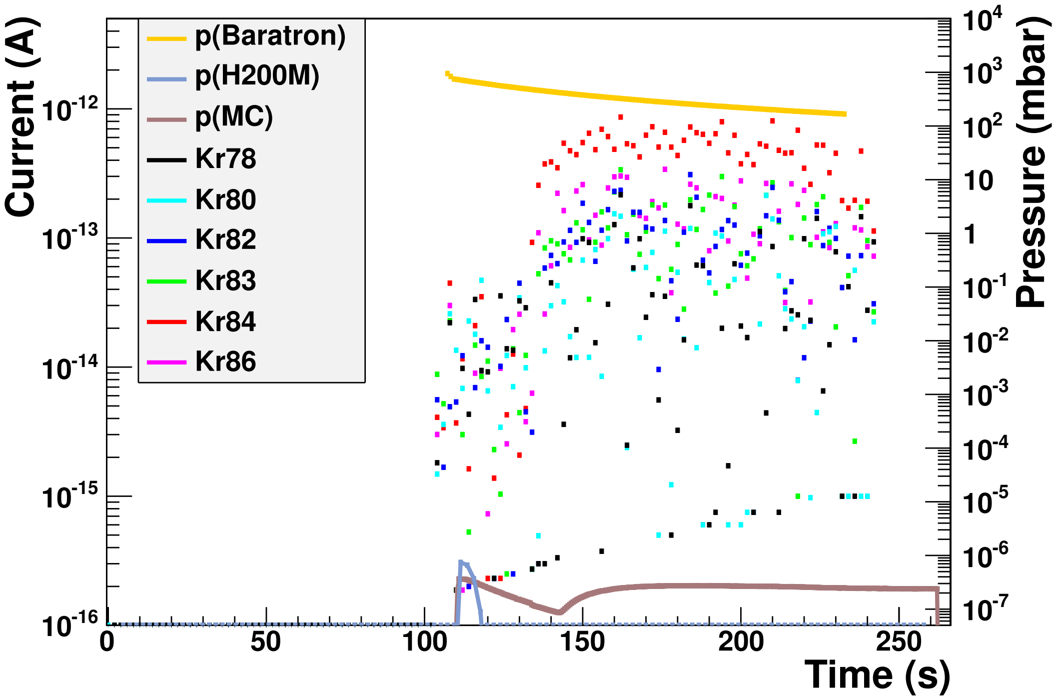

Figure 7.7.: *Time evolution of krypton isotopes normalized by flow rate at* (150 ± 6) *ppb* $\frac{Kr}{Xe}$ *(Run 6-03).*

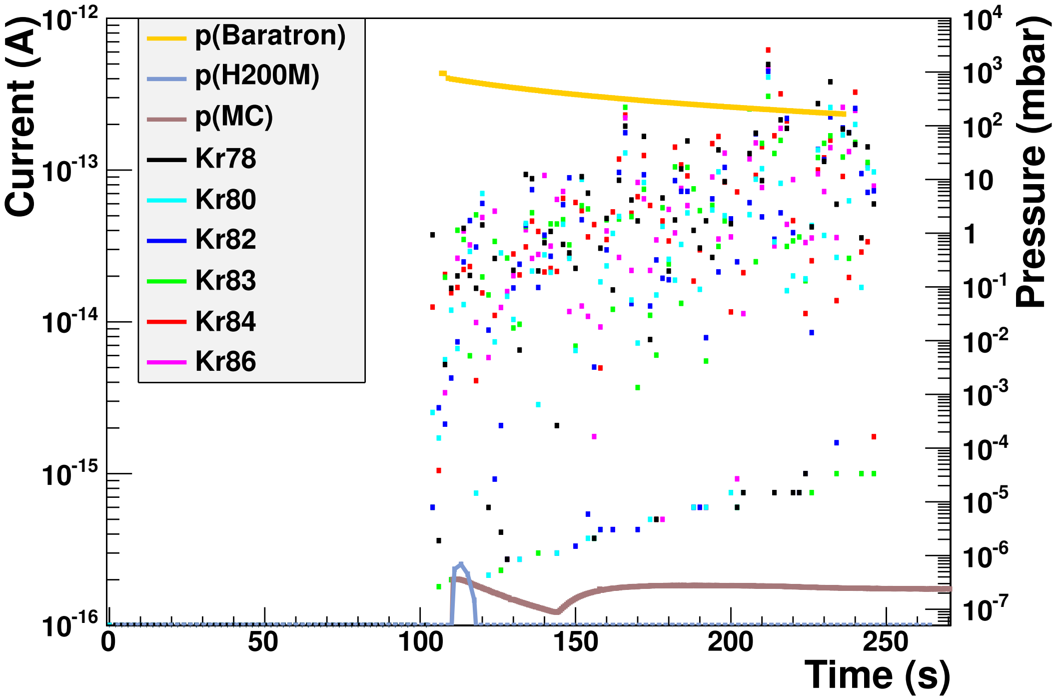

Figure 7.8.: *Time evolution of krypton isotopes normalized by flow rate at* (20 ± 1) *ppb* $\frac{Kr}{Xe}$ *(Run 6-04).*

7.1.2. Sensitivity estimation by isotopic composition

From the isotopic ratios shown in table A.4 a rough estimate of the sensitivity of the experiment can be obtained.

Consequently the sensitivity of the experiment can be determined from the ratio of the relative abundances of the barely detectable isotope and the base peak of ^{84}Kr, as long as the isotope of lower natural abundance can still be distinguished from the background. This means the krypton concentration can be reduced by the relative isotopic composition, while ^{84}Kr would still be detectable.

The isotopic ratios are obtained by averaging over all krypton isotopes, even over those which do not exist in nature over the previously mentioned plateau. On average, as the time delay between opening the leak-valve and the first krypton signals depends on the doped concentration of krypton, higher time channels for the plateau integration have to be used. In order to sum up all currents consistently with the same statistics, integration starts at $t = 140$ s. This is the time of the signal showing up with the highest delay. All currents are then integrated over 50 seconds. The background is taken into account by subtracting the integrated current values of $\frac{m}{z} = 85$ Th. Figures 7.9 to 7.12 show the pattern of isotopic ratios for different concentrations of krypton considering only the uncertainty in artificial krypton doping. In order to estimate the sensitivity of the CT-MS technique the marginal signals of ^{78}Kr and ^{80}Kr at 1100 ppb and 150 ppb of doping are selected.

According to table A.4 the factors of relative isotopic compositions for ^{78}Kr and ^{80}Kr with respect to ^{84}Kr are 163 and 25, respectively.

$$\frac{\text{Artificially doped krypton concentration}}{\text{Factor of relative isotopic composition}} = \text{Limit for sensitivity} \tag{7.1}$$

$$\frac{(1100 \pm 41)\ \text{ppb}}{163} \approx (7 \pm 1)\ \text{ppb} \tag{7.2}$$

$$\frac{(150 \pm 6)\ \text{ppb}}{25} \approx (6 \pm 1)\ \text{ppb} \tag{7.3}$$

With respect to the relative natural abundances an upper limit for the sensitivity can be estimated around (6.5 ± 1.5) ppb by considering the range of the two measurements at 1100 and 150 ppb of artificial krypton doping. The result is in agreement with the measurement at 20 ppb $\frac{\text{Kr}}{\text{Xe}}$. However, the value of $\frac{m}{z} = 78$ Th deviates from the expected isotopic ratio at figure 7.12. In order to test whether a contamination is present at $\frac{m}{z} = 78$ Th and finally detect krypton in pure xenon samples the CT-MS technique is modified. The improvements are presented in the following section.

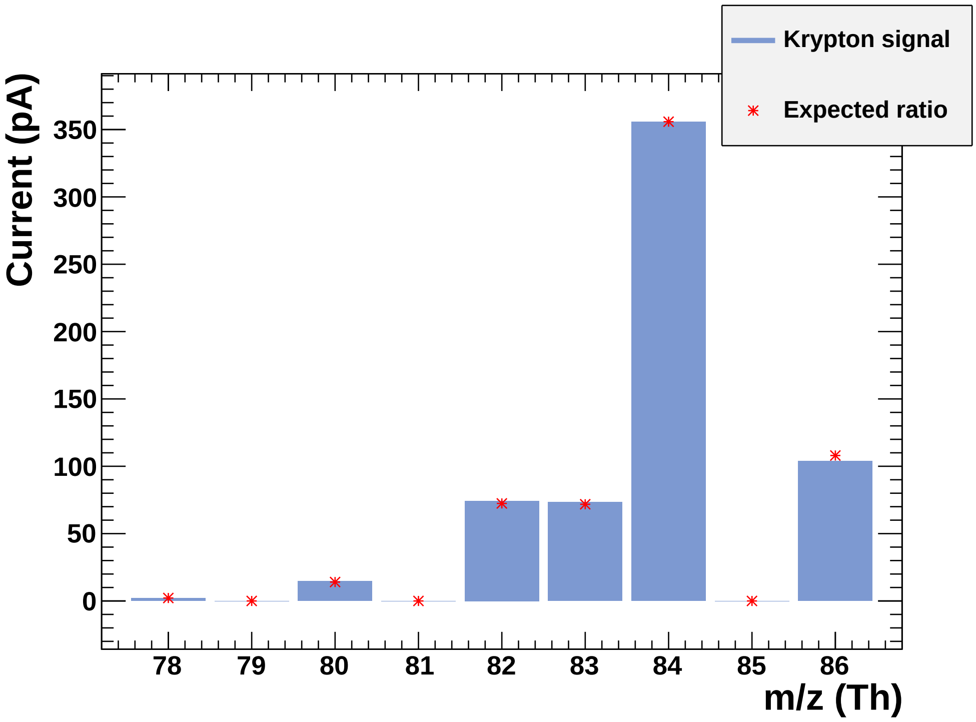

Figure 7.9.: *Measured and expected isotopic ratios of krypton at an artificial doping of* (8800 ± 282) *ppb* $\frac{Kr}{Xe}$ *(Run 6-01).*

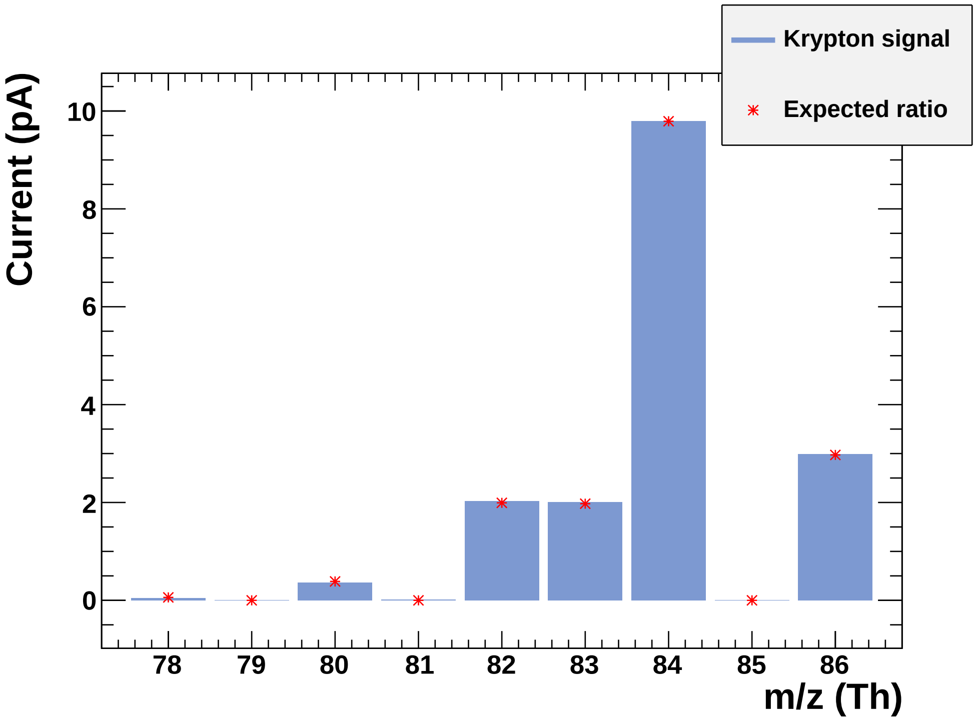

Figure 7.10.: *Measured and expected isotopic ratios of krypton at an artificial doping of* (1100 ± 41) *ppb* $\frac{Kr}{Xe}$ *(Run 6-02).*

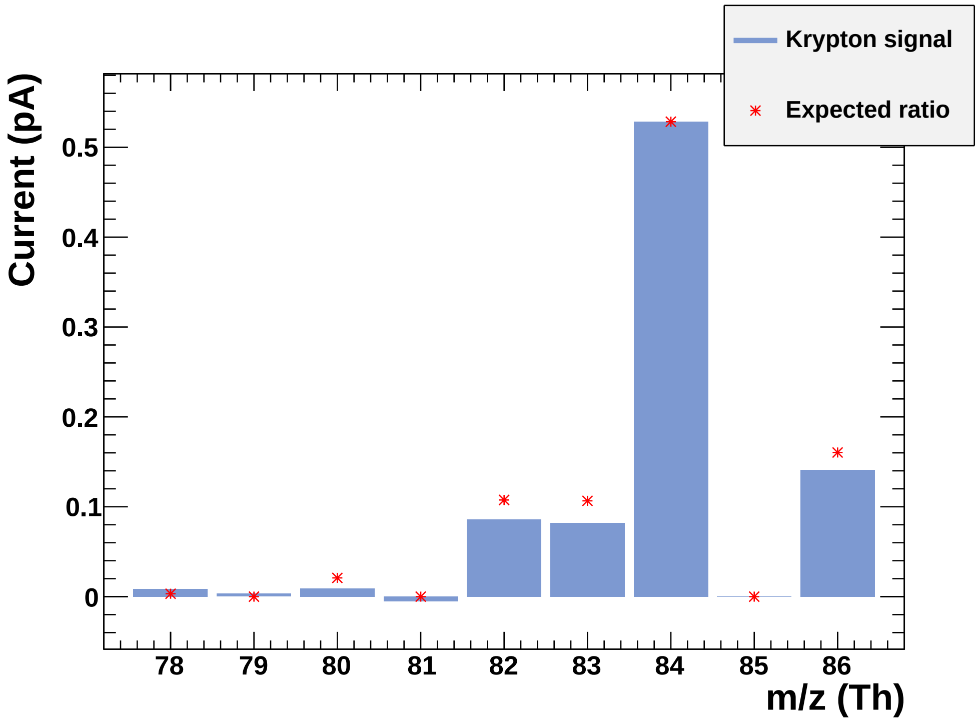

Figure 7.11.: *Measured and expected isotopic ratios of krypton at an artificial doping of* (150 ± 6) *ppb* $\frac{Kr}{Xe}$ *(Run 6-03).*

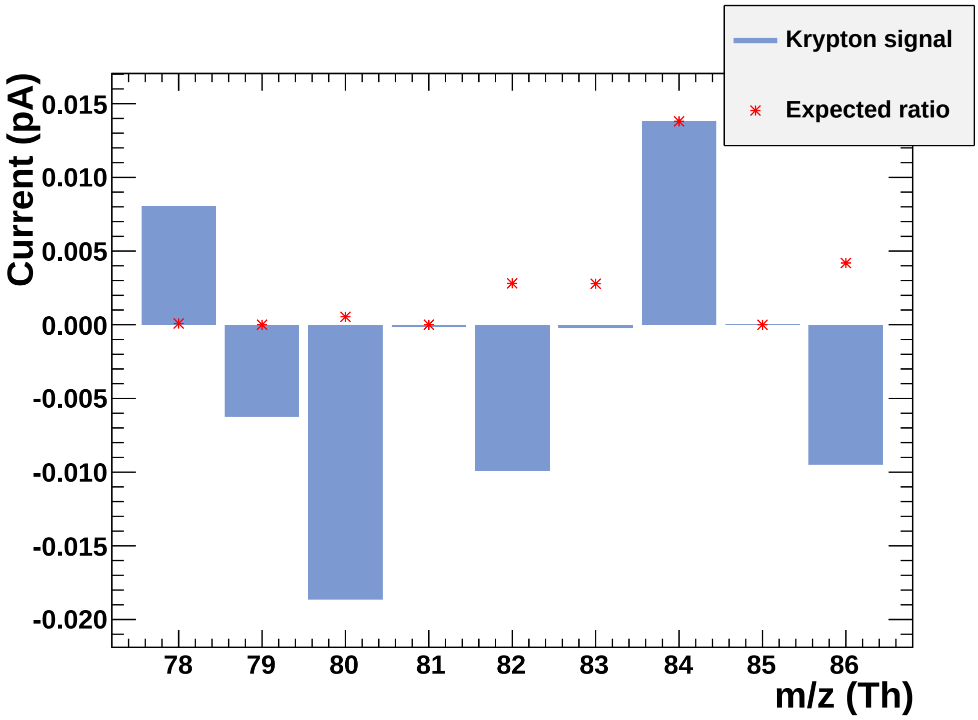

Figure 7.12.: *Measured and expected isotopic ratios of krypton at an artificial doping of* (20 ± 1) *ppb* $\frac{Kr}{Xe}$ *(Run 6-04). The negative values are due to background subtraction.*

7.2. Enhancement of the CT-MS technique by reducing the effective pumping speed

The efficiency of electron ionization depends on the intrinsic properties and the design of the ion source, as well as on the operation parameters of the setup. According to [Gro04] the overall ionization efficiency for an atom entering the ionizing region is rather low, as the majority of the sample is removed by the turbo molecular pumping system. This issue is showing up, as the mean free pass both for the sample atoms and for the electrons is large and the collision cross-section of the electrons themself is rather low. In order to increase the sensitivity of the setup by more than an order of magnitude the effective pumping speed of the turbo molecular pump is reduced.

Partially closing of the VAT UHV gate valve which separates the main chamber with the quadrupole mass filter from the turbo molecular pump gives rise to such an enhancement. The hand wheel of the gate valve is moved 14.5 turns until the gate is close to catch. This leads to a significant reduction in the effective pumping speed. Fully closing of the turbo molecular pump for a short time interval has been investigated and rejected, as the current signals break down at low concentrations $\lesssim 100$ ppb. Reasons for this might be caused by the reduced mean free path of the ions or the ionization itself is suppressed by the high amount of xenon gas present in the main chamber.

Time evolution of krypton signals at reduced effective pumping speed

The time evolution of krypton while the effective pumping speed is reduced is visible in figures 7.13 to 7.20. The overall slope of the signals is similar to the previously shown time evolution of krypton. The measured currents have increased due to the reduction in pumping speed. However, at low concentrations the ^{78}Kr isotope behaves differently, as it shows a constant signal of $I \sim 5 \cdot 10^{-12}$ A. First evidence of this can be seen in figure 7.14, where it does not decrease after closing the leak-valve at $t = 200$ s, but stays constant. In the following measurements it always shows the same current values, independent of the krypton concentration. Even in the second measurement with pure xenon (figure 7.17), which is discussed in detail in section 7.3.1, its current stays constant around $5 \cdot 10^{-12}$ ampere. Hence it is assumed that an unknown contamination with $\frac{\mathrm{m}}{\mathrm{z}} = 78$ Th is present. Possible candidates are discussed in chapter 8.1.

Normalization by flow rate at reduced effective pumping speed

Normalization by flow rate is performed according to the described method in section 7.1.1. As before, a plateau shows up. Due to the partially closed gate valve the pressure in the main chamber reaches the operating region of the pressure gauge of the Transpector2.

The offset between the two recorded pressures in the main chamber has its origin in the correction for the sort of gas applied to the IONIVAC pressure gauge IE 514.

The time evolution of different krypton concentrations normalized by flow rate is visible in figures 7.21 to 7.28.

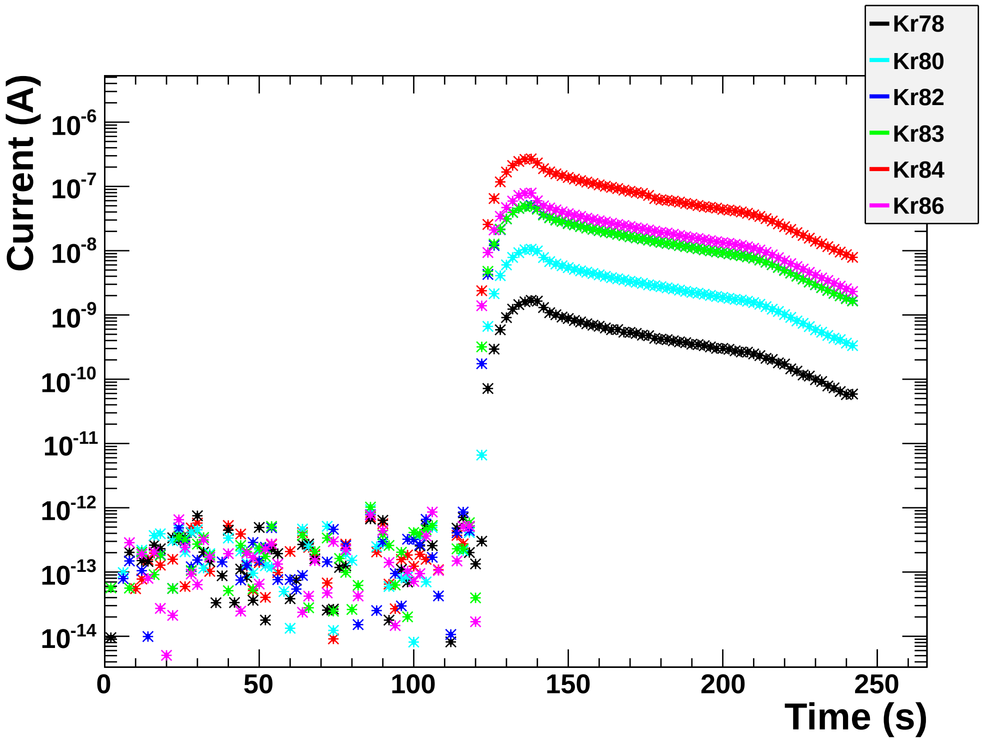

Figure 7.13.: *Time evolution of krypton isotopes at* (9000 ± 289) *ppb* $\frac{Kr}{Xe}$ *with reduced effective pumping speed (Run 7-01).*

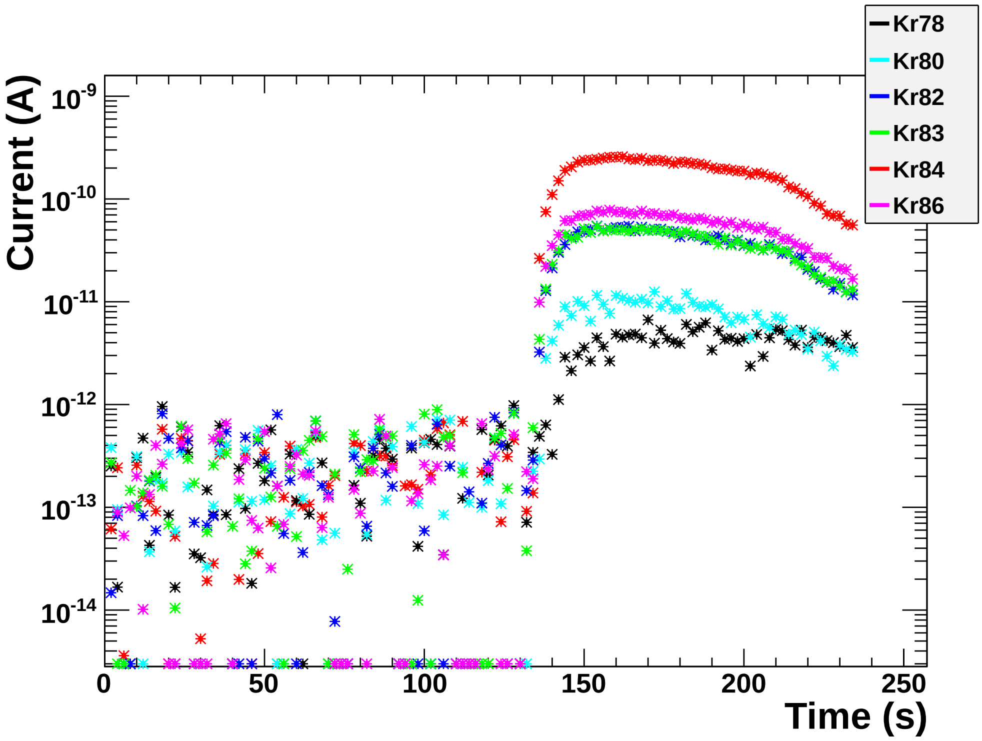

Figure 7.14.: *Time evolution of krypton isotopes at* (154 ± 7) *ppb* $\frac{Kr}{Xe}$ *with reduced effective pumping speed (Run 7-03).*

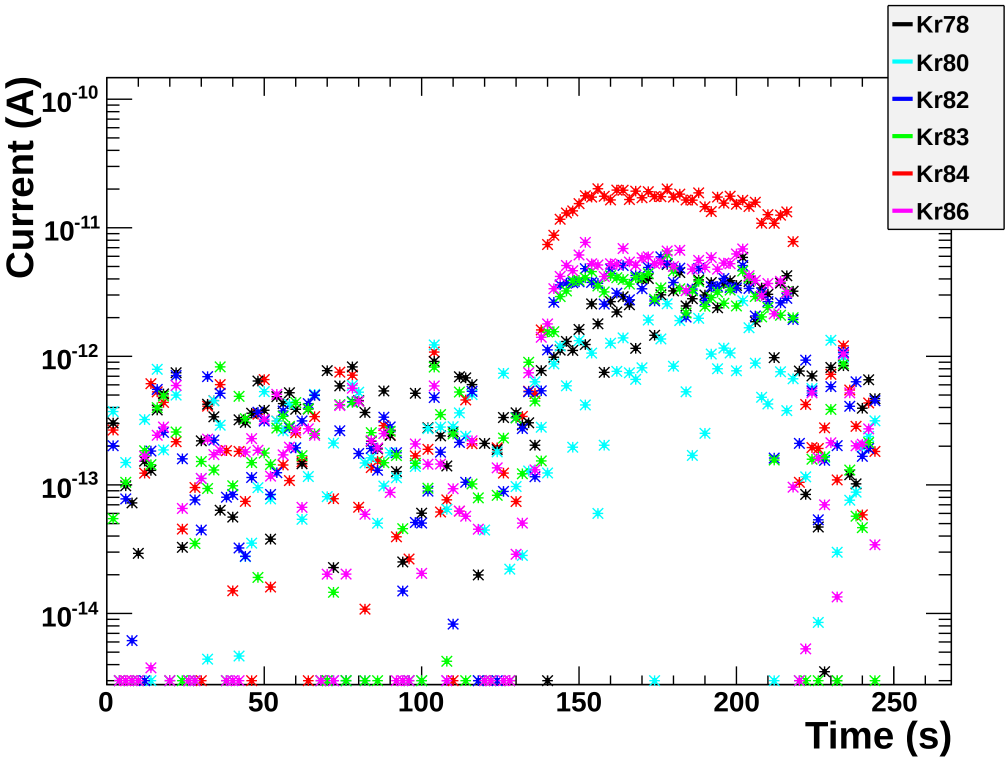

Figure 7.15.: *Time evolution of krypton isotopes at* (20 ± 1) *ppb* $\frac{Kr}{Xe}$ *with reduced effective pumping speed (Run 7-04).*

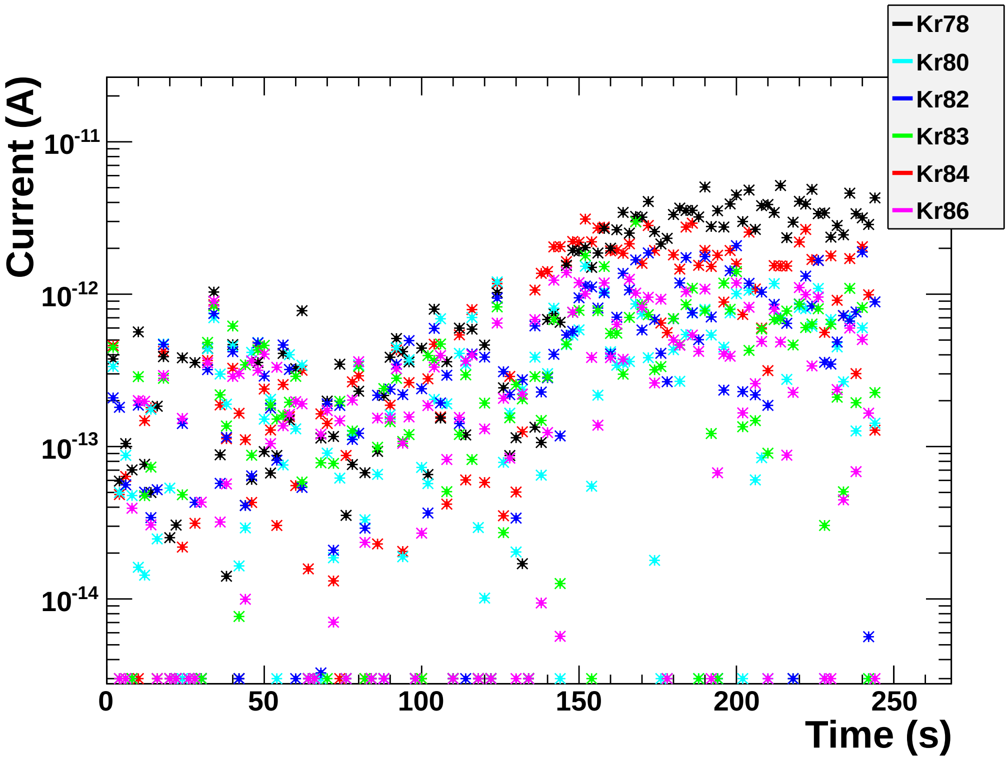

Figure 7.16.: *Time evolution of krypton isotopes in pure xenon with reduced effective pumping speed (Run 7-05).*

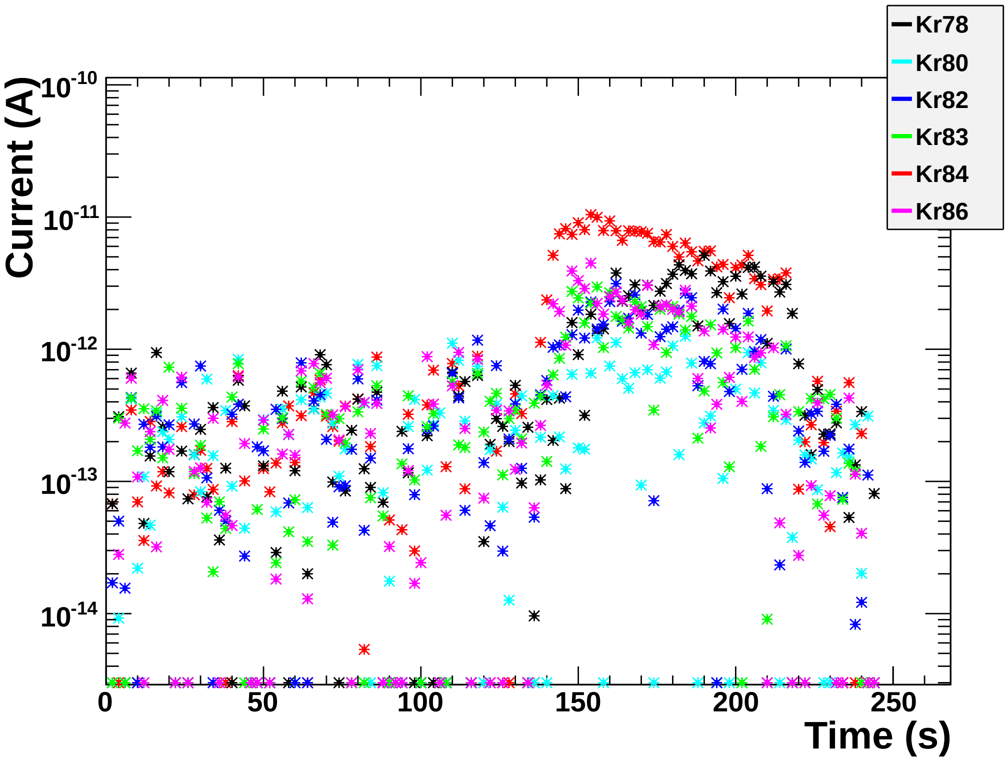

Figure 7.17.: *Time evolution of krypton isotopes in pure xenon with reduced effective pumping speed (Run 7-06).*

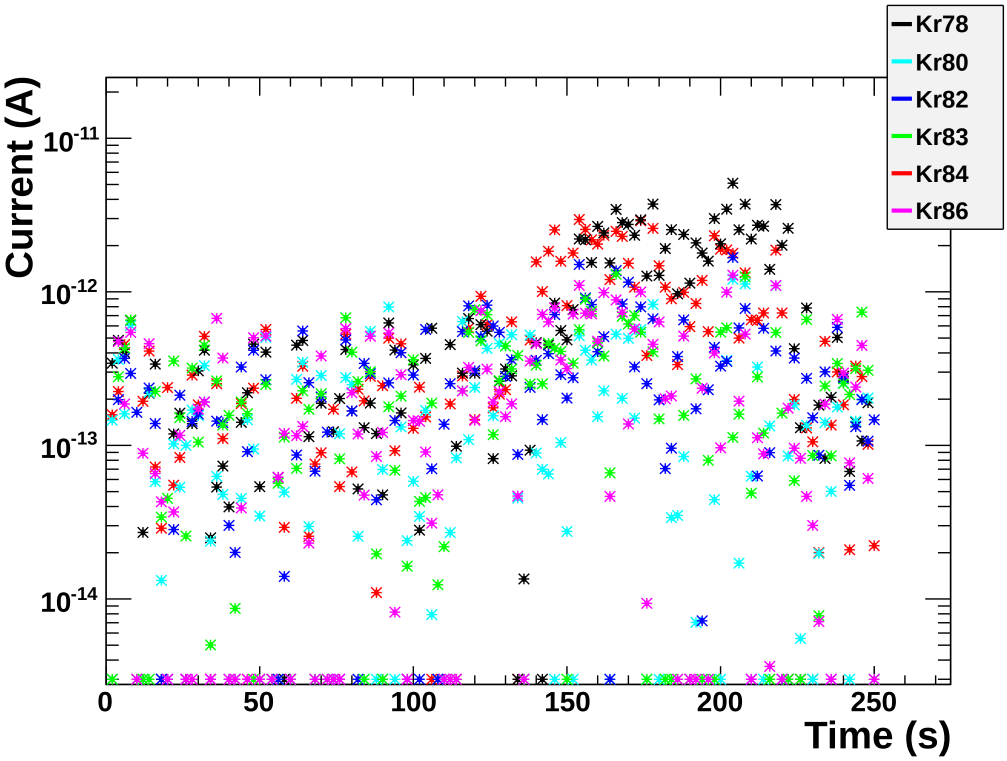

Figure 7.18.: *Time evolution of krypton isotopes in pure xenon with reduced effective pumping speed (Run 7-07).*

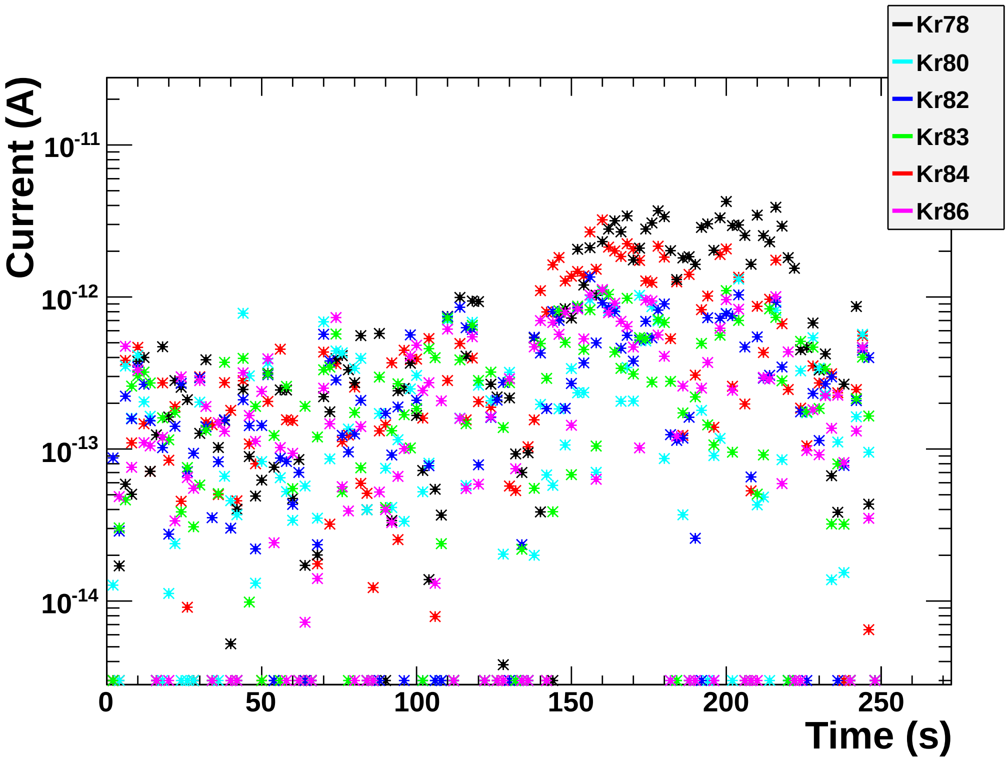

Figure 7.19.: *Time evolution of krypton isotopes in pure xenon with reduced effective pumping speed (Run 7-08).*

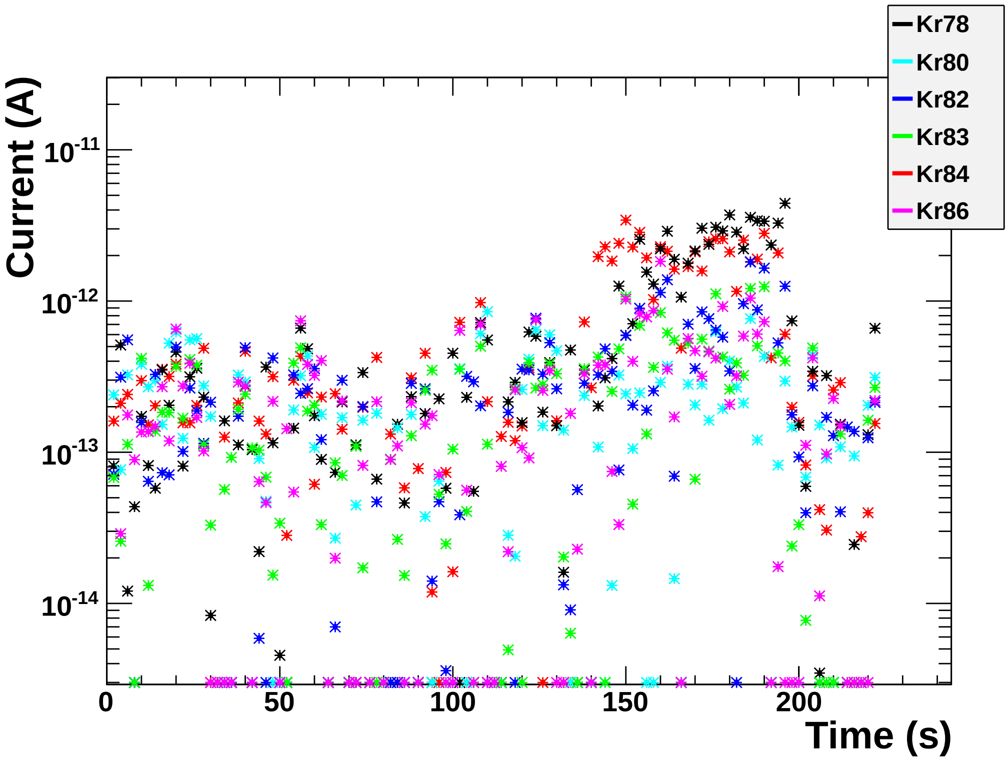

Figure 7.20.: *Time evolution of krypton isotopes in pure xenon with reduced effective pumping speed (Run 7-09).*

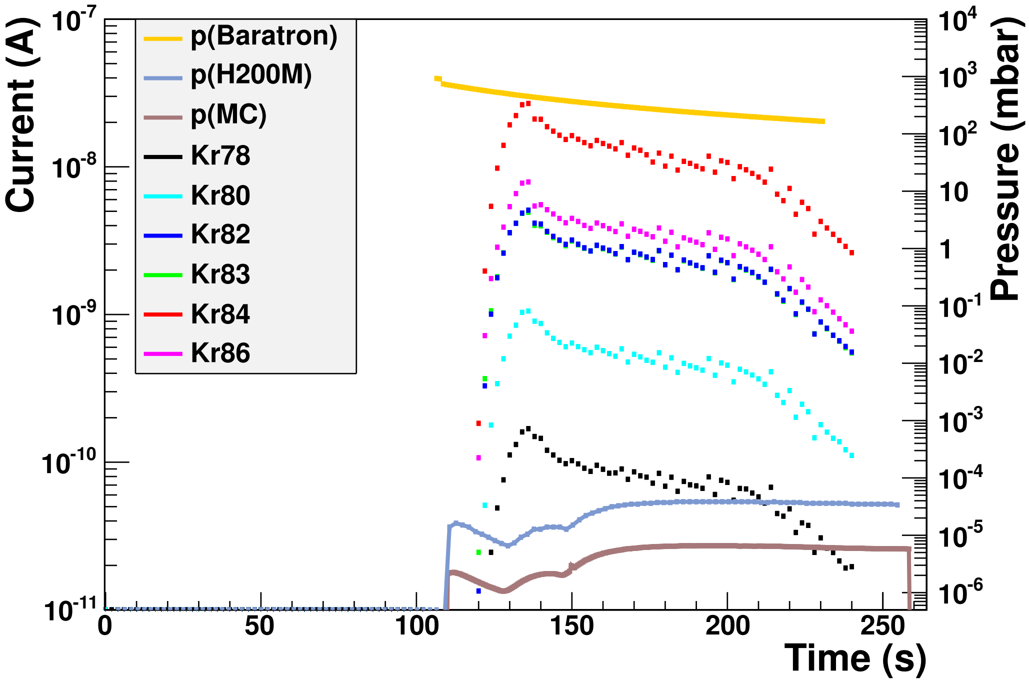

Figure 7.21.: *Time evolution of krypton isotopes at* (9000 ± 289) *ppb* $\frac{Kr}{Xe}$ *with reduced effective pumping speed normalized by flow rate (Run 7-01).*

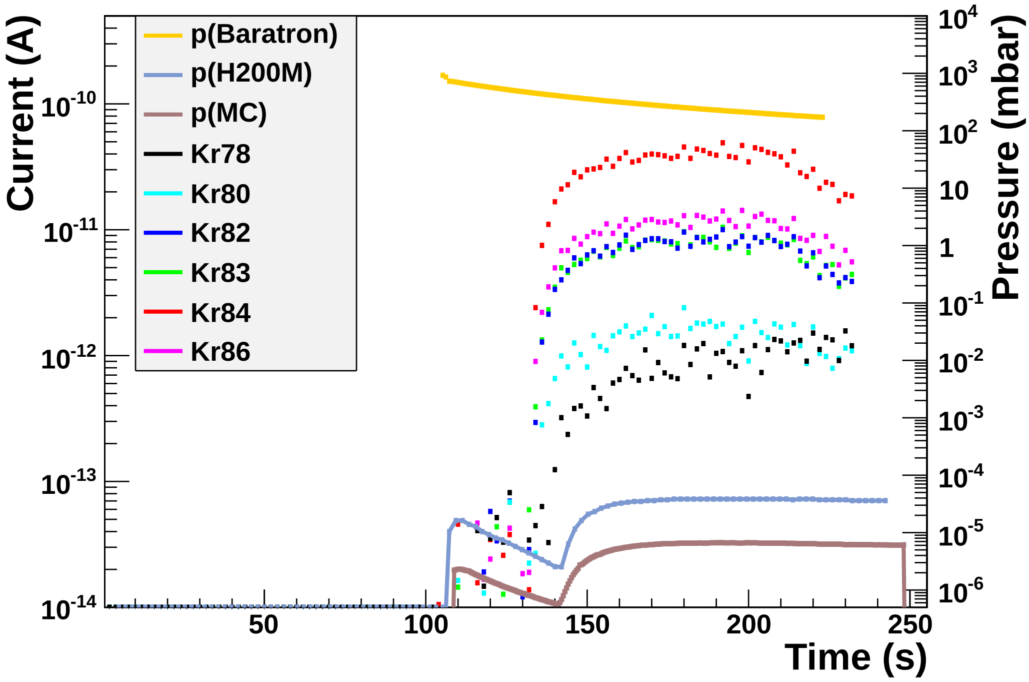

Figure 7.22.: *Time evolution of krypton isotopes at* (154 ± 7) *ppb* $\frac{Kr}{Xe}$ *with reduced effective pumping speed normalized by flow rate (Run 7-03).*

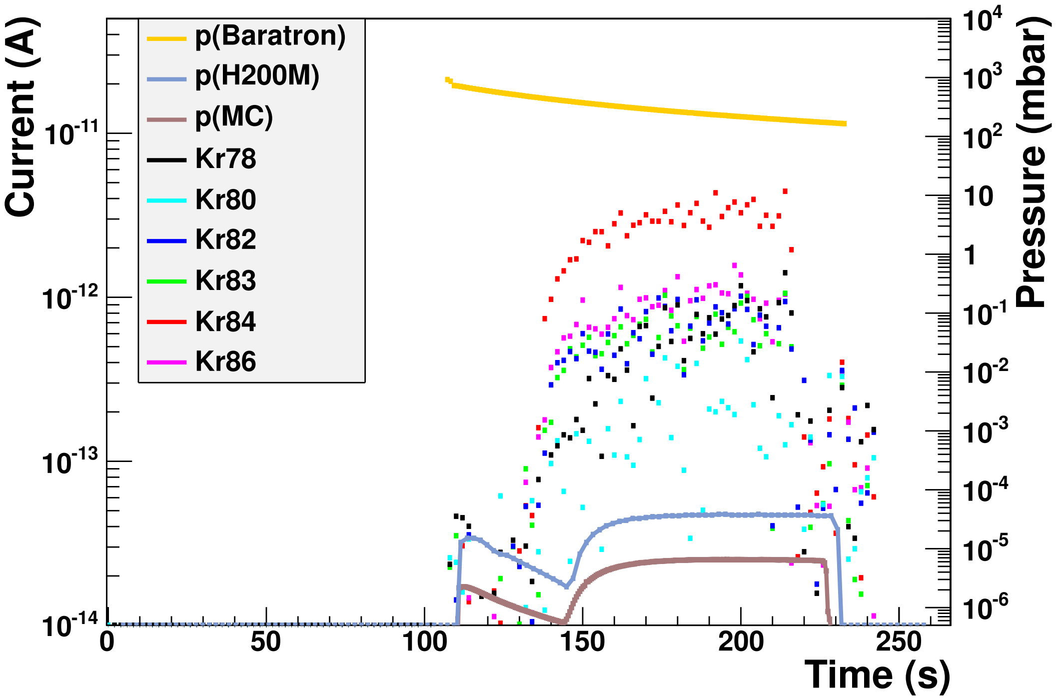

Figure 7.23.: *Time evolution of krypton isotopes at* (20 ± 1) *ppb* $\frac{Kr}{Xe}$ *with reduced effective pumping speed normalized by flow rate (Run 7-04).*

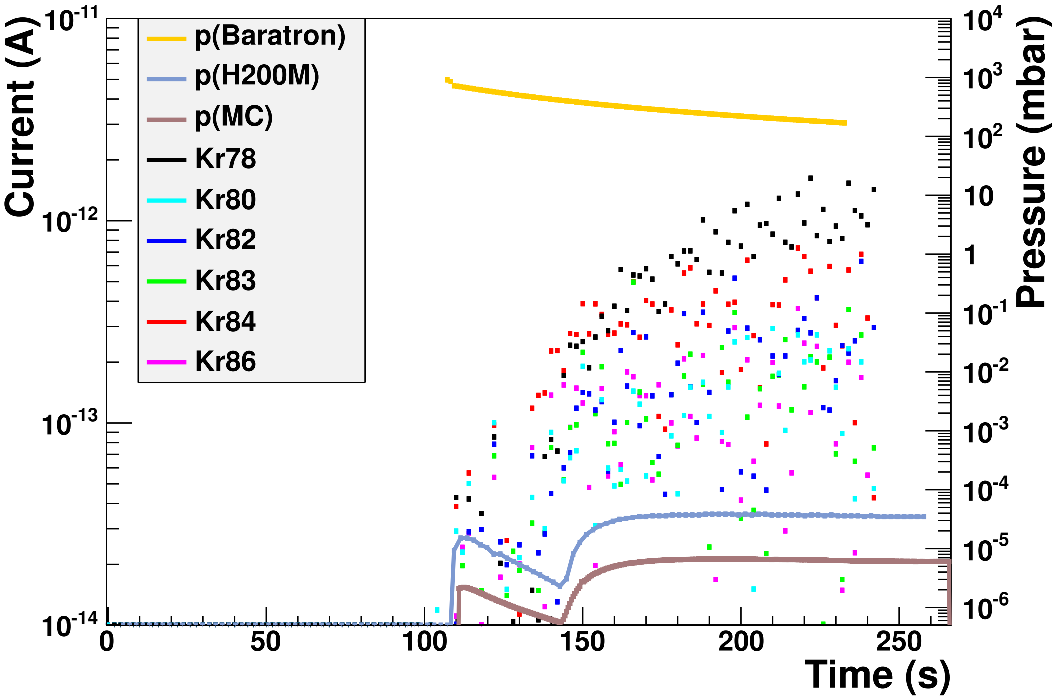

Figure 7.24.: *Time evolution of krypton isotopes in pure xenon with reduced effective pumping speed normalized by flow rate (Run 7-05).*

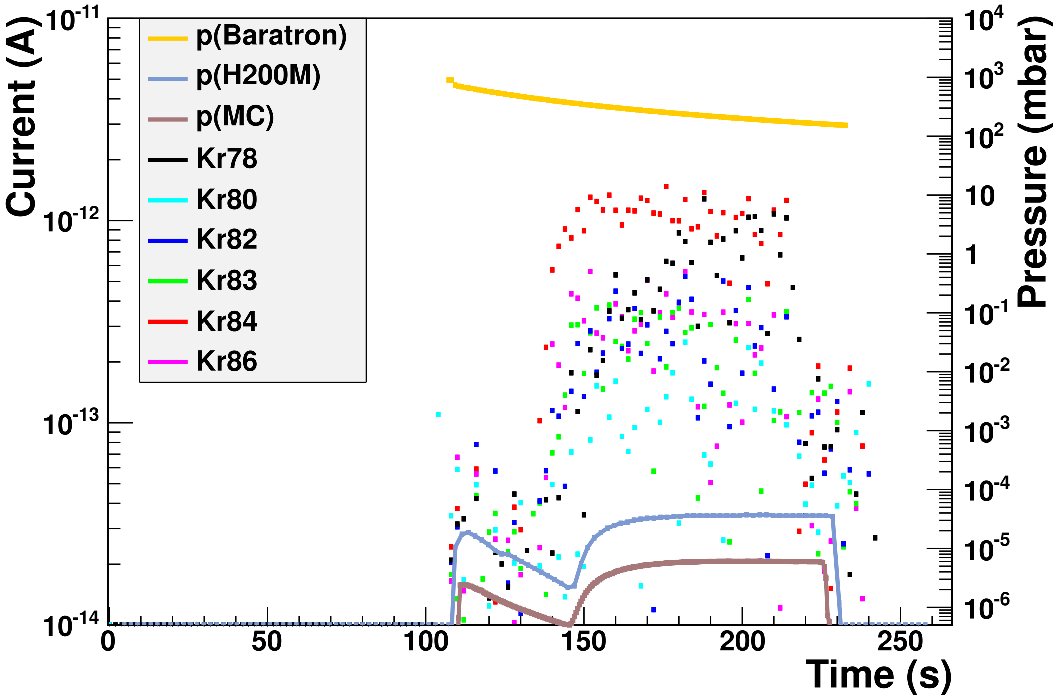

Figure 7.25.: *Time evolution of krypton isotopes in pure xenon with reduced effective pumping speed normalized by flow rate (Run 7-06).*

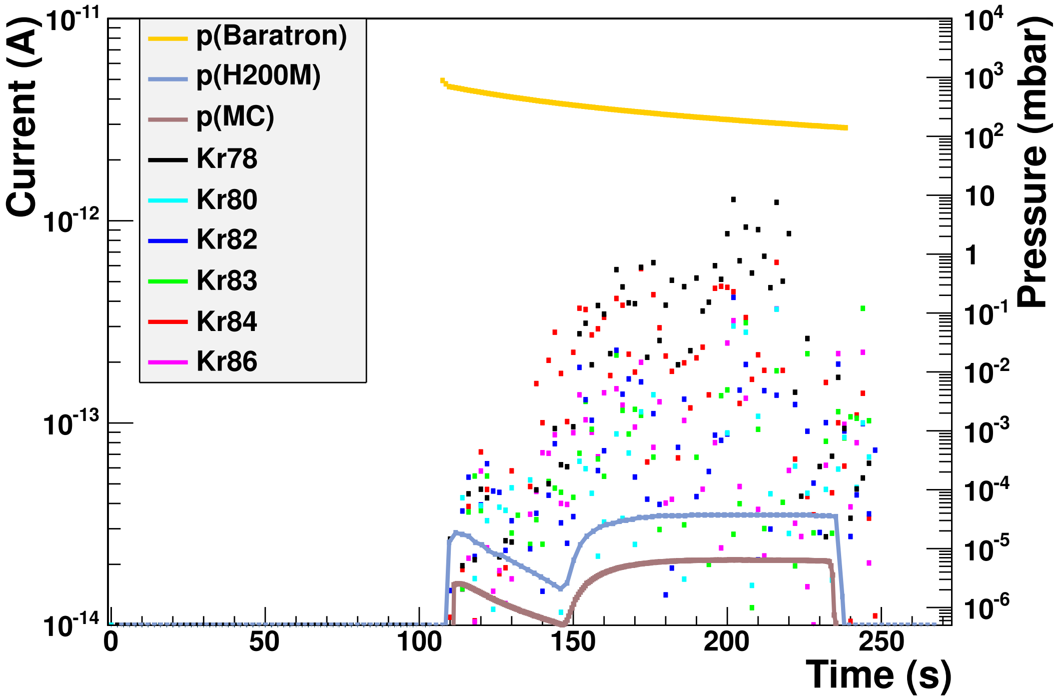

Figure 7.26.: *Time evolution of krypton isotopes in pure xenon with reduced effective pumping speed normalized by flow rate (Run 7-07).*

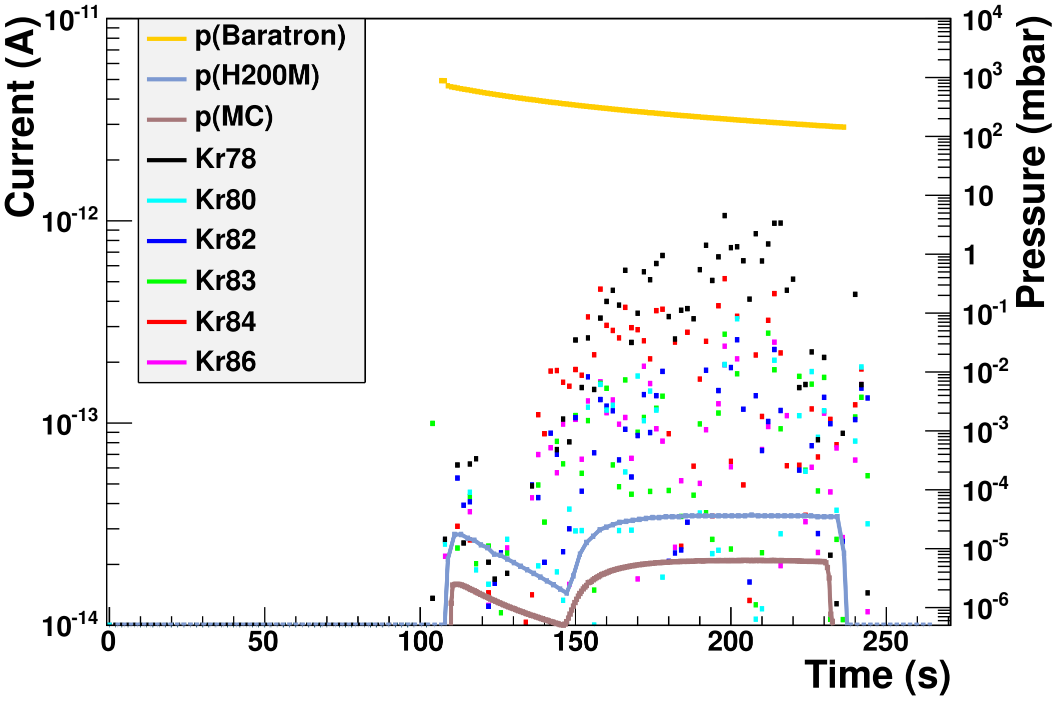

Figure 7.27.: *Time evolution of krypton isotopes in pure xenon with reduced effective pumping speed normalized by flow rate (Run 7-08).*

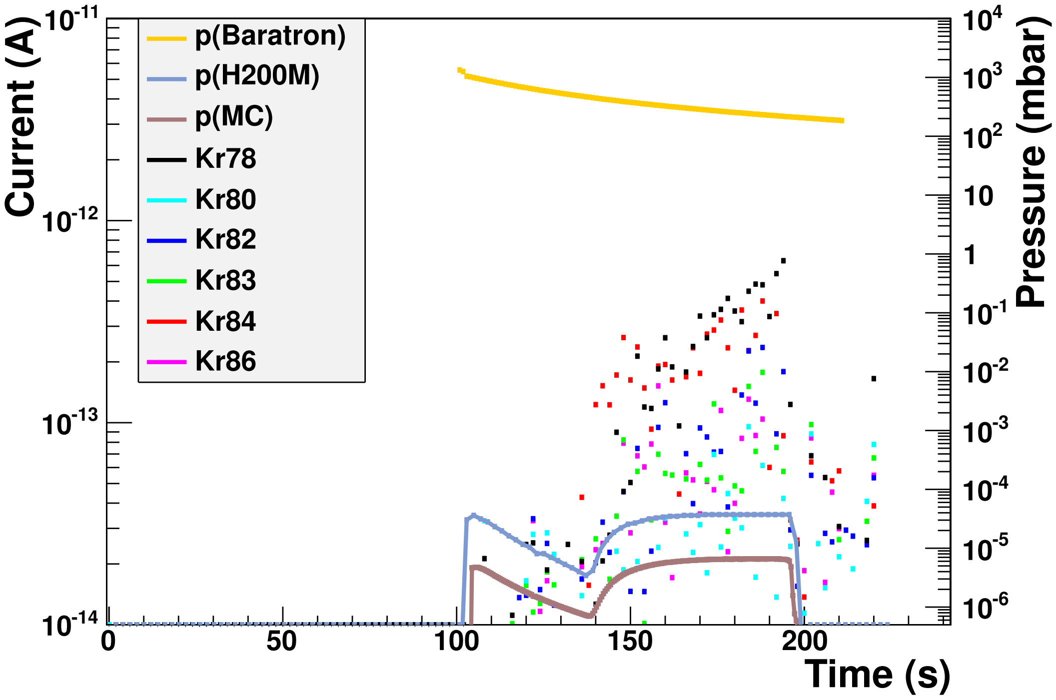

Figure 7.28.: *Time evolution of krypton isotopes in pure xenon with reduced effective pumping speed normalized by flow rate (Run 7-09).*

7.3. New analysis method for reduced effective pumping speed

For the following analysis only the plateaus of the flow normalized time evolution of different krypton signals are considered. This is done by averaging over the plateau for all krypton isotopes and afterwards subtracting the value of $\frac{m}{z} = 85$ Th in order to account for backgrounds. Taking $\frac{m}{z} = 85$ Th instead to the measured data in the time interval of [0,100] seconds before introducing the sample accounts for electronic background, xenon-related background or systematics of the applied technique.

Taking $\frac{m}{z} = 85$ Th as a background might seem odd at first, as the goal of this experiment is the determination of krypton concentrations in xenon in order to extract the ^{85}Kr concentration. To a good approximation $\frac{m}{z} = 85$ Th can be used as a background reference as the natural abundance of $\frac{^{\mathrm{nat}}\mathrm{Kr}}{^{85}\mathrm{Kr}} \sim 1.5 \cdot 10^{-11}$ only accounts for a marginal signal which is orders of magnitude below the sensitivity of the experiment.

Evidence of this can be seen in the following estimation: The current signal of ^{85}Kr is 1800 times lower than the signal of ^{84}Kr at an artificially doped concentration of 9000 ppb $\frac{\mathrm{Kr}}{\mathrm{Xe}}$. The ratio of $\frac{^{80}\mathrm{Kr}}{^{85}\mathrm{Kr}}$ still gives a factor of 72 in difference, which is in agreement with the abundances of the krypton isotopes[1].

As at low concentrations ^{78}Kr significantly deviates from its expected abundance of 0.35 % and furthermore does not show the same time evolution as all the other isotopes do, it is assumed that an unknown contamination is present. Therefore the ^{78}Kr data are rejected in the following analysis. Possible origins for the assumed contamination are discussed in chapter 8.1.

---

[1] The factor of relative isotopic composition for ^{84}Kr and ^{80}Kr is $\frac{^{84}\mathrm{Kr}}{^{80}\mathrm{Kr}} = \frac{0.57}{0.0225} \approx 25 = \frac{1800}{72}$.

7.3.1. Dixon's Q-test

The second measurement of pure xenon differs from the other four un-doped measurements, as can be seen in figures 7.17 and 7.25. Therefore Dixon's Q-test [Dea51] is applied in order to decide whether the data of the second measurement can be discarded from the following analysis.

The Q-value is defined as the difference between the outlying value of interest x_i and its nearest neighbor $\widetilde{x}_i$ in the set of data, divided by the full range of the data set.

$$\mathrm{Q} = \frac{x_i - \widetilde{x}_i}{x_{\mathrm{max}} - x_{\mathrm{min}}} \tag{7.4}$$

The test is applied to all krypton isotopes separately after subtraction of the $\frac{m}{z} = 85$ Th values besides the previously rejected ^{78}Kr isotope.

Depending on the sample size, a specific data point is discarded in case the Q-value exceeds a critical value $\mathrm{Q_C}$. The left half of table 7.1 shows the confidence levels for discarding a specific data point for a sample size of 5 members according to [Ror91].

Q_C	Rejection at
0.557	80 % C.L.
0.642	90 % C.L.
0.710	95 % C.L.
0.780	98 % C.L.
0.821	99 % C.L.

Q-value results	Rejection with
Q(^{80}Kr) = 0.333	———
Q(^{82}Kr) = 0.875	99 % C.L.
Q(^{83}Kr) = 0.889	99 % C.L.
Q(^{84}Kr) = 0.943	99 % C.L.
Q(^{86}Kr) = 0.821	99 % C.L.

Table 7.1.: *The left table lists the critical Q-values for a sample size of N=5 [Ror91]. The right table lists the results from the Q-test for different isotopic patterns.*

On the right half of table 7.1 the calculated Q-values for all isotopes of the second pure xenon measurement are presented. Besides ^{80}Kr, which has a Q-value of Q(^{80}Kr) = 0.333, all data points can be discarded with 99 % confidence level. The lower Q-value of ^{80}Kr can be explained by the fact that the concentration of ^{80}Kr, which has only a natural abundance of 2.25 %, is close the background level and therefore has no values which significantly differ from each other. Evidence of this can be seen as two out of five current values achieve negative values after background subtraction.

Hence the full data set of the second pure xenon measurement is discarded with the previously stated confidence level.

The deviation of the second pure xenon measurement could be caused by the reduction in effective pumping speed. As the gate valve is closed manually, an additional unknown systematic error is introduced.

7.3.2. Measurements without artificial krypton concentration

The averaged and background subtracted data of the pure xenon measurements without artificial krypton concentration[2] c are analyzed.
The measured currents I from all 20 data points[3] from the pure xenon measurements ($c = 0$) are fitted with a zeroth order polynomial, accounting for their isotopic abundance f listed in table A.4, according to

$$I_0 = \frac{I(c = 0)}{f} \tag{7.5}$$

where c represents the concentration of artificially doped krypton added to the intrinsic krypton concentration c_0 in xenon within the dedicated mixing chamber.
As many of the experimental uncertainties are unknown, equal errors for all data points are assumed. To a good approximation this is valid, as the uncertainties of the krypton isotopes should not differ a lot from each other as they have the same ionization probability as well as transmission rate through the mass filter. Moreover, their detection efficiency including gain of the EM should only slightly differ from each other because of their small difference in mass.
This set of data is then treated with *Minuit C-Version 97.01* from H. Barth in order to minimize χ^2 and obtain the unknown uncertainties on the recorded currents. Figure 7.29 shows the relation of χ^2 on the assumed absolute uncertainty giving rise to an optimal ($\chi^2 = 1$) error estimation of ± 0.024 pA per data point.
Figure 7.30 gives a clear expression of the determination of I_0. The measured currents $I(c = 0)$ are weighted by their natural abundance f and ordered by their $\frac{m}{z}$ ratio. A constant fit[4] gives rise to

$$I_0 = (0.336 \pm 0.019) \text{ pA} \tag{7.6}$$

according to equation 7.5.
However, the errors on I_0 do not scale with $\frac{1}{\sqrt{N}}$ as

$$0.024 \cdot \frac{1}{\sqrt{20}} = 0.005 \neq 0.019$$

disagrees with the assumption of statistical error propagation.
Therefore at least one additional uncertainty has to be present besides the statistical error.

---

[2] The intrinsic krypton concentration in “pure“ xenon is indicated with c_0.

[3] 4 sets of data with 5 isotopes each. All data sets are listed in table A.2 in the appendix.

[4] Zeroth order polynomial

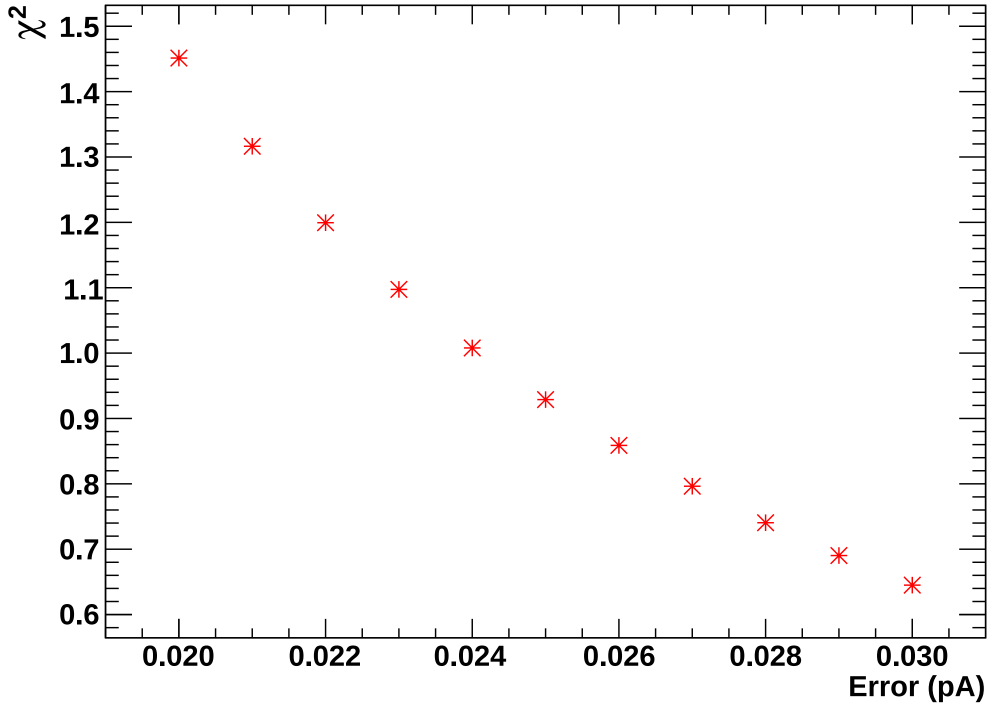

Figure 7.29.: *Estimation of optimal* χ^2 *assuming a constant error in measured current. Minuit C-Version 97.01 gives rise to an absolute error of* ± 0.024 *pA for each current measurement* I*.*

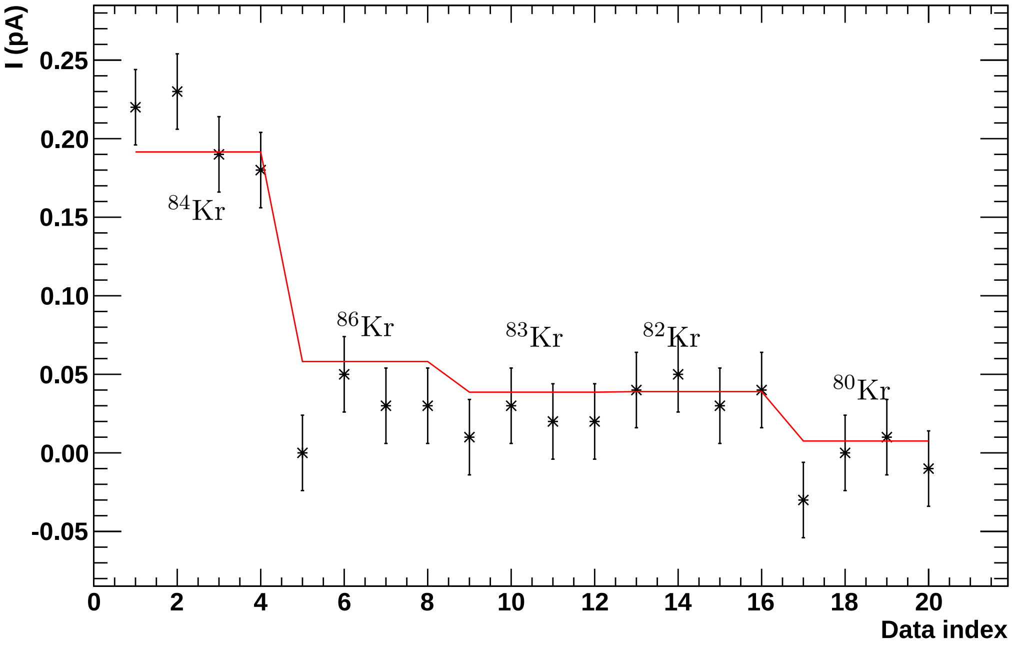

Figure 7.30.: *Section wise fitting of a constant value of measured currents* $I(c = 0)$*. The data are weighted by their natural abundance* f *and ordered by their* $\frac{m}{z}$ *ratio. The fit* $I_0 = \frac{I}{f}$ *assumes equal constant uncertainties of* ± 0.024 *pA for the measured currents* I*.*

7.3.3. Measurements with artificial krypton concentration

Since a linear fit does not describe the measured data properly, another ansatz is required. As the artificially doped krypton concentration c approaches the level of intrinsic krypton contamination in pure xenon c_0, the measured currents I asymptotically approach a constant value at I_0.

It does not exist an a priori function which describes the data. However, a quadratic approach matches the data both at high and low levels of artificial krypton doping.

As any function can be approximated by a polynomial of n-th grade, second order terms are additionally considered in the following analysis. A Taylor series of $I = I_0 + ac$ around $c = 0$, while $I(c \neq 0)$ describes the measured current values, leads to a quadratic approach as well:

$$I(c) = f \cdot (I_0 + ac + bc^2) \tag{7.7}$$

The measured current I is caused by the sum of artificially doped krypton at a concentration c and the intrinsic krypton concentration in xenon $c_0 \equiv \frac{I_0}{a}$. For small artificial concentrations c, the intrinsic krypton concentration c_0 becomes more and more dominant.

$$I = I_0 + ac \tag{7.8}$$

$$\Leftrightarrow \qquad c = \frac{I - I_0}{a} \tag{7.9}$$

$$= \frac{I}{a} - \underbrace{\frac{I_0}{a}}_{c_0} \tag{7.10}$$

The data with $c \neq 0$ are again treated with Minuit while I_0 is fixed at the value obtained previously and a and b are the new fit parameters.

Absolute uncertainties

For all data points equal absolute errors are assumed and χ^2 is minimized in order to account for the unknown uncertainties.

The relation of χ^2 on the assumed absolute uncertainty gives rise to an optimal error of ±72 pA per data point ($\chi^2 = 1$). Details of this are shown in figure 7.31.

Figure 7.32 gives a clear expression of the determination of the parameters a and b. The measured currents $I(c \neq 0)$ are ordered by their krypton concentration at different $\frac{m}{z}$ ratios. A second order polynomial fit applied to all isotopes gives rise to

$$I = I_0 + ac + bc^2 \tag{7.11}$$

$$I_0 = (0.336 \pm 0.019)\ \text{pA}$$

$$a = (0.369 \pm 0.783)\ \frac{\text{pA}}{\text{ppb}}$$

$$b = (2.5 \cdot 10^{-4} \pm 9.0 \cdot 10^{-5})\ \frac{\text{pA}}{\text{ppb}^2}$$

$$c_0 \left(\frac{\text{Kr}}{\text{Xe}}\right) = \frac{I_0}{a} = (0.91 \pm 1.93)\ \text{ppb} \qquad \textit{preliminary} \tag{7.12}$$

according to equation 7.7.

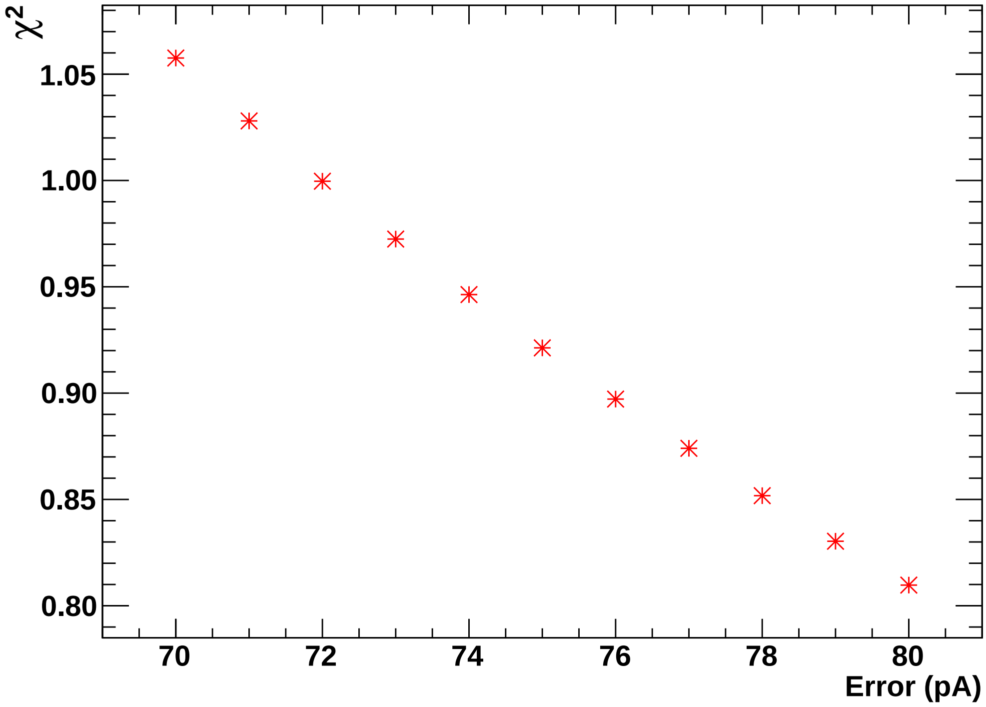

Figure 7.31.: *Estimation of optimal* χ^2 *assuming a constant error. A quadratic fit gives rise to an absolute error of* ±*72 pA for each current measurement* I*.*

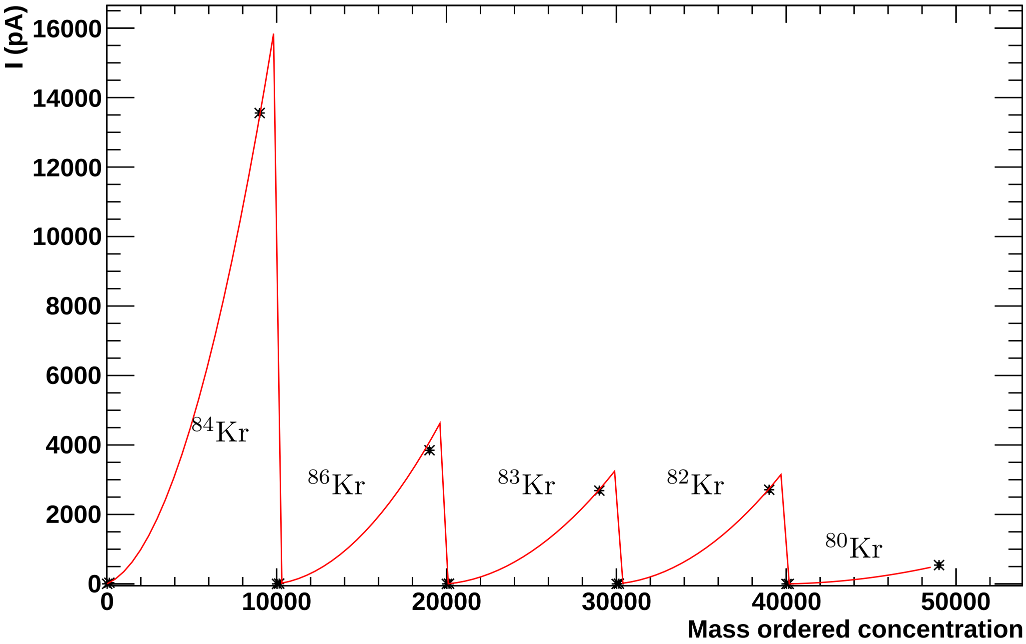

Figure 7.32.: *Second order polynomial fit of measured currents* $I(c \neq 0)$*. The data are ordered by their krypton concentration at different* $\frac{m}{z}$ *ratios. The fit* $I = I_0 + ac + bc^2$ *assumes equal constant uncertainties of* ±72 *pA for the measured currents* I*.*

Relative uncertainties

An uncertainty of ±72 pA disagrees with the measured data at low doping concentrations $c\left(\frac{\mathrm{Kr}}{\mathrm{Xe}}\right) \leq 20$ ppb, as it is 100 times higher than the measured current values. That is why this approach is modified by assuming equal relative errors.

All data points with $c \neq 0$ are analyzed with Minuit in order to minimize χ^2, assuming equal relative errors in order to account for the unknown uncertainties.

The relation of χ^2 to the assumed relative uncertainty gives rise to an optimal error of ±32 % per data point ($\chi^2 = 1$). Details of this are shown in figure 7.33.

Figure 7.34 gives a clear expression of the determination of the parameters a and b. The measured currents $I(c \neq 0)$ are ordered by their krypton concentrations at different $\frac{m}{z}$ ratios. A second order polynomial fit applied to all isotopes gives rise to

$$I = I_0 + ac + bc^2 \tag{7.13}$$

$$\begin{aligned} I_0 &= (0.336 \pm 0.019)\ \mathrm{pA} \\ a &= (0.196 \pm 0.025)\ \frac{\mathrm{pA}}{\mathrm{ppb}} \\ b &= (2.8 \cdot 10^{-4} \pm 4.0 \cdot 10^{-5}\ \frac{\mathrm{pA}}{\mathrm{ppb}^2} \end{aligned}$$

$$c_0\left(\frac{\mathrm{Kr}}{\mathrm{Xe}}\right) = \frac{I_0}{a} = (1.71 \pm 0.24)\ \mathrm{ppb} \qquad \textit{preliminary} \tag{7.14}$$

according to equation 7.7.

The assumed relative errors cause high uncertainty at concentrations $c\left(\frac{\mathrm{Kr}}{\mathrm{Xe}}\right) \geq 150$ ppb, where the error is expected to be small because of less dilution processes and higher signal currents. However, the range of higher concentrations is of minor importance as the ppb level is investigated.

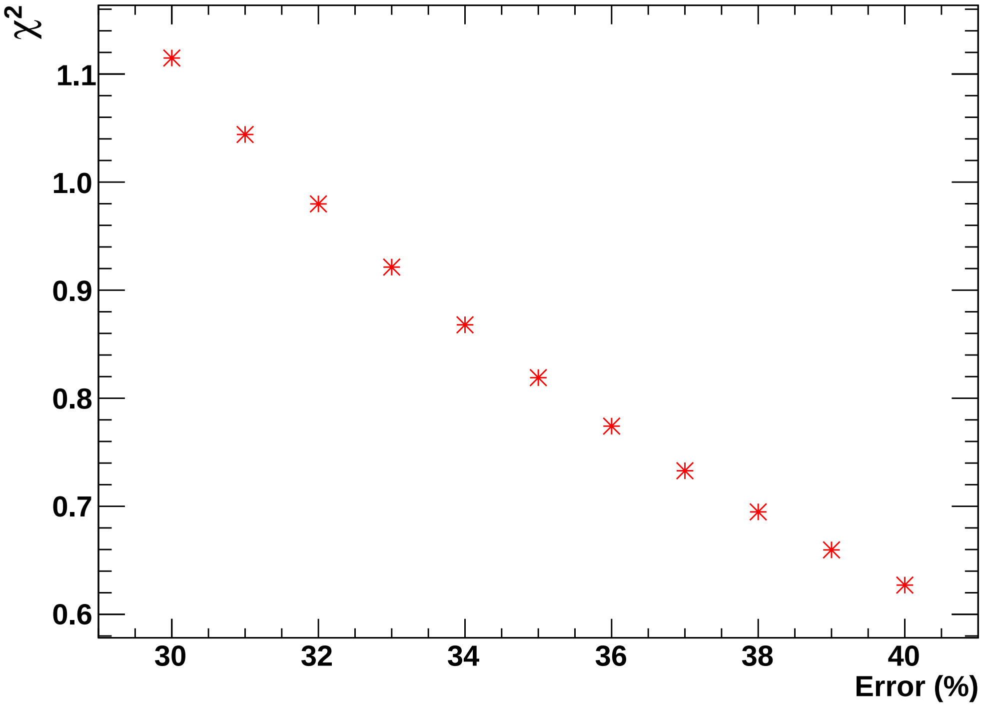

Figure 7.33.: *Estimation of optimal* χ^2 *assuming a relative error. A quadratic approach gives rise to an relative error of* ±32 *% for each current measurement* I*.*

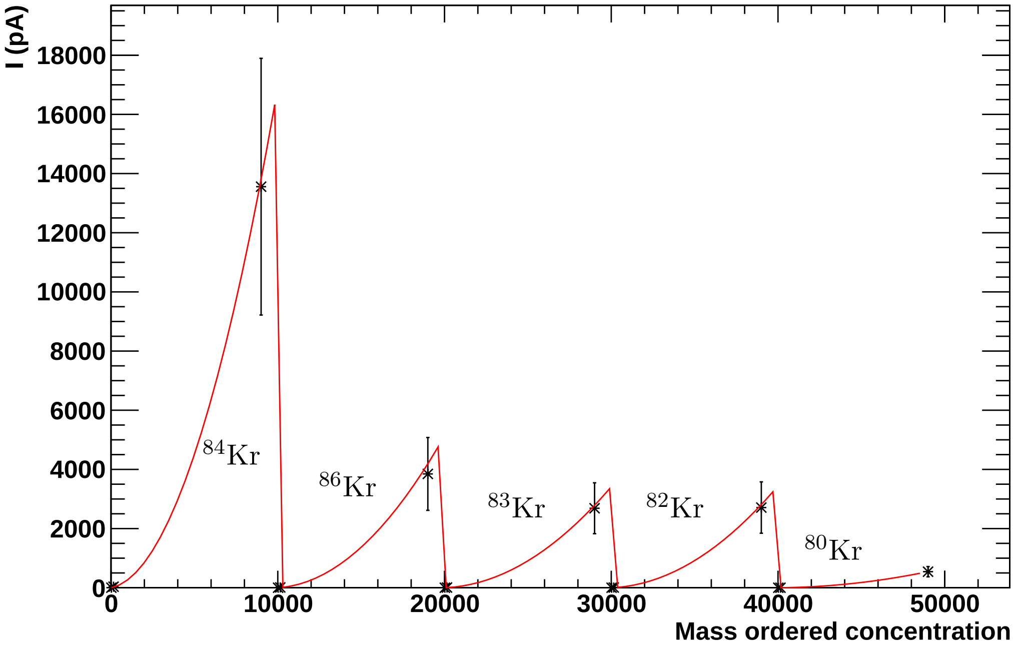

Figure 7.34.: *Second order polynomial fit of measured currents* $I(c \neq 0)$*. The data are ordered by their krypton concentration at different* $\frac{m}{z}$ *ratios. The fit* $I = I_0 + ac + bc^2$ *assumes equal relative uncertainties of* ±32 *% for the measured currents* I*.*

Combination of absolute and relative errors

As reasonable uncertainties both at high and low concentrations are required, a combination of the previously examined absolute and relative errors is assumed in order to address this problem. The relative error would dominate at higher concentrations, whereas the absolute error limits the sensitivity at low concentrations.
Using Minuit in order to optimize χ^2 of the previously defined fit function

$$I(c) = f \cdot (I_0 + ca + cb^2) \quad ; \quad I_0 = (0.336 \pm 0.019)\ \mathrm{pA} \tag{7.15}$$

considering both a relative and an absolute uncertainty gives rise to a full set of solutions which fulfill the condition $\chi^2 = 1$.
Figure 7.35 shows the dependence of χ^2 on the assumed uncertainties. An additional selection of different error combinations is listed in table 7.2.

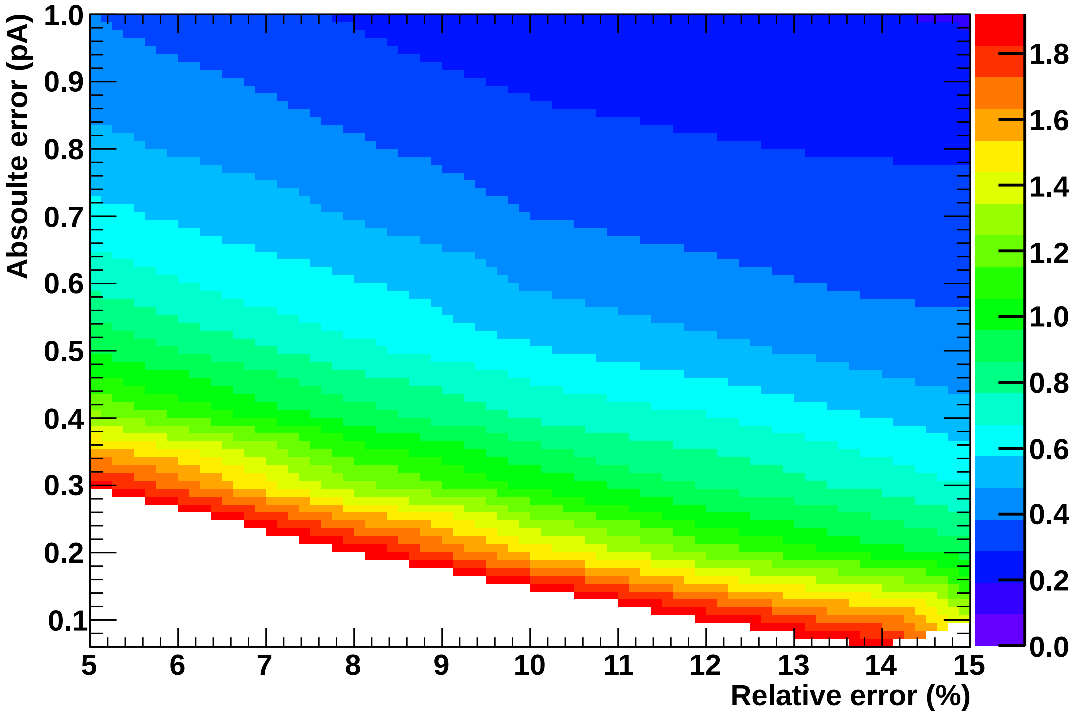

Figure 7.35.: *χ^2 as a function of combined relative and absolute uncertainties. $\chi^2 = 1$ is indicated in light green colors.*

Rel. err (%)	Abs. err (pA)	χ^2	$a\left(\frac{\mathrm{pA}}{\mathrm{ppb}}\right)$	$b\left(\frac{\mathrm{pA}}{\mathrm{ppb}^2}\right)$	$c_0\left(\frac{\mathrm{Kr}}{\mathrm{Xe}}\right)_{\mathrm{prel.}}$
5	0.48	1.009	0.350±0.017	$(2.5 \pm 0.1) \cdot 10^{-4}$	(0.96±0.07) ppb
10	0.30	1.033	0.322±0.022	$(2.5 \pm 0.1) \cdot 10^{-4}$	(1.04±0.09) ppb
15	0.17	1.019	0.291±0.025	$(2.6 \pm 0.2) \cdot 10^{-4}$	(1.15±0.12) ppb

Table 7.2.: *Some assorted uncertainties extracted from figure 7.35 fulfilling the request of $\chi^2 = 1$.*

The relative error of ±5 % is in agreement with the determined uncertainty of the artificial krypton doping at low concentrations. Moreover, $\pm 5.0 \cdot 10^{-13}$ ampere corresponds

to the “dark current“ measured by the Transpector2 in case no sample gas is present, corresponding to a pressure in the main chamber of $p_{\mathrm{MC}} \sim 10^{-9}$ mbar.
Figure 7.36 shows the measured currents $I(c \neq 0)$ ordered by their krypton concentrations at different $\frac{m}{z}$ ratios. A second order polynomial fit applied to all isotopes gives rise to

$$I = I_0 + ca + cb^2 \tag{7.16}$$

$$\begin{aligned} I_0 &= (0.336 \pm 0.019)\ \mathrm{pA} \\ a &= (0.350 \pm 0.017)\ \frac{\mathrm{pA}}{\mathrm{ppb}} \\ b &= (2.5 \cdot 10^{-4} \pm 1.0 \cdot 10^{-5})\ \frac{\mathrm{pA}}{\mathrm{ppb}^2} \end{aligned}$$

$$c_0\left(\frac{\mathrm{Kr}}{\mathrm{Xe}}\right) = \frac{I_0}{a} = (0.96 \pm 0.07)\ \mathrm{ppb} \qquad \textit{preliminary} \tag{7.17}$$

according to equation 7.7.

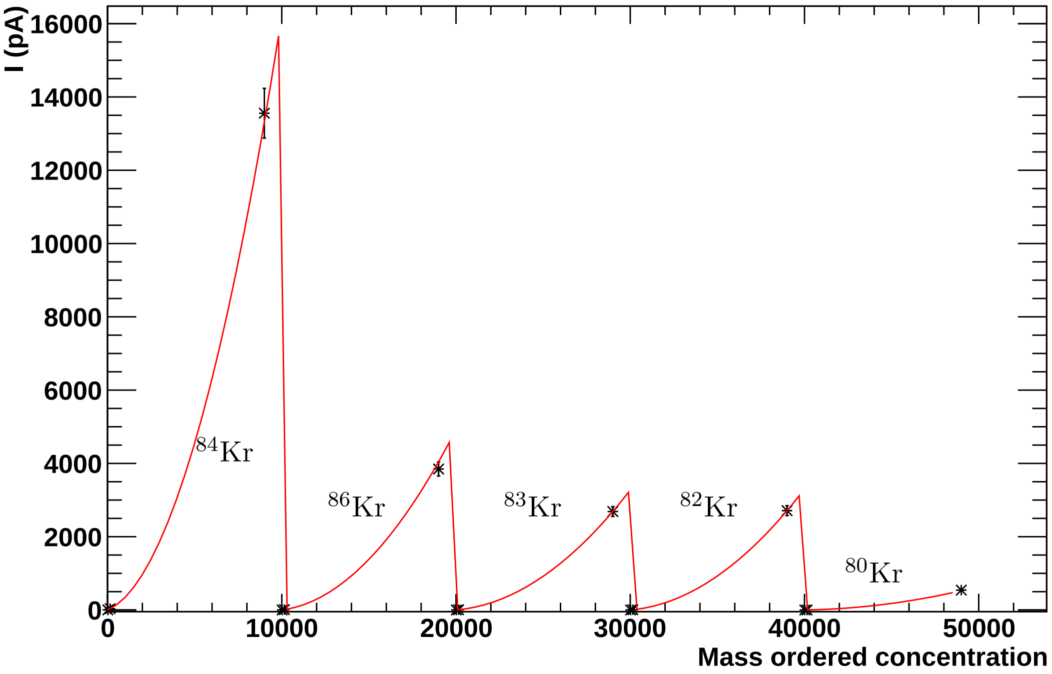

Figure 7.36.: *Second order polynomial fit of measured currents $I(c \neq 0)$. The data are ordered by their krypton concentration at different $\frac{m}{z}$ ratios. The fit $I = I_0 + ac + bc^2$ assumes a combination of relative and absolute uncertainties of ($\pm 5\,\% \pm 0.48$) pA for the measured currents I.*

However, these combined errors give only an lower limit of the entire uncertainty of the experiment, as other possible errors might arise from the pressure gauges (drift of the Baratron offset around zero), temperature fluctuations in the lab or deviations in the reproducibility of the effective pumping speed.
Therefore the three calibration measurements of 9000 ppb, 150 ppb and 20 ppb are separately analyzed using the previously estimated combined uncertainty in order to obtain a more appropriate uncertainty.

The combined error of ($\pm 5\,\% \pm 4.8 \cdot 10^{-13}$) ampere is separately applied to each doped data set both for a linear ($b = 0$) and a quadratic approach ($b \neq 0$) in order to estimate the overall dynamic range of the two assumptions. The results are listed in table 7.3.

Doping level	$a\left(\frac{\text{pA}}{\text{ppb}}\right)$	$b\left(\frac{\text{pA}}{\text{ppb}^2}\right)$	$c_0(\frac{\text{Kr}}{\text{Xe}})$
9000 ppb	0.842±0.923	$(1.9 \pm 1.0) \cdot 10^{-4}$	(0.40±0.44) ppb
9000 ppb	2.593±0.058	b=0	(0.13±0.01) ppb
150 ppb	0.317±0.288	$(6.2 \pm 19.2) \cdot 10^{-4}$	(1.06±0.96) ppb
150 ppb	0.409±0.018	b=0	(0.82±0.06) ppb
20 ppb	0.222±0.754	$(9.2 \pm 337) \cdot 10^{-4}$	(1.51±5.13) ppb
20 ppb	0.204±0.048	b=0	(1.65±1.89) ppb

Table 7.3.: *Case-by-case analysis of artificially doped measurements with an assumed uncertainty of (*$\pm 5\,\% \pm 0.48$*) pA both for a linear (*$b = 0$*) and a quadratic approach (*$b \neq 0$*).*

The parameters a shown in table 7.3 deviate from each other both at different concentrations and different approaches, namely linear and quadratic approximations.

Concerning the highest krypton concentration of 9000 ppb the obtained values for a differ both from the parameters at 20 and 150 ppb and from each other depending on the applied fit function. Moreover, the parameters at 20 and 150 ppb only change slightly by varying the fit method from a linear to a quadratic approach. A likely explanation would be that these values are closer to the region of pure xenon which is being investigated. Therefore it is assumed that the applied fit method only has a small impact on the results by considering low doping concentrations. Hence the parameter a from the 20 and 150 ppb measurement, obtained by a linear approximation, is chosen for an estimation of the final result of the krypton fraction in xenon and the overall uncertainty. By comparing these to datasets at different concentrations to some extend the reproducibility of the effective pumping speed of the turbo molecular pump is taken into account as well.

$$\begin{aligned} c_0\left(\frac{\text{Kr}}{\text{Xe}}\right) &= \frac{I_0}{\bar{a}} \qquad ; \qquad \bar{a} = (0.31 \pm 0.10)\,\frac{\text{pA}}{\text{ppb}} \\ &= \frac{(0.336 \pm 0.019)\ \text{pA}}{(0.31 \pm 0.10)\,\frac{\text{pA}}{\text{ppb}}} \\ &\approx (1.1 \pm 0.4)\ \text{ppb} \end{aligned} \tag{7.18}$$

Therefore the intrinsic concentration of krypton in xenon is determined to (1.1±0.4) ppb.

7.3.4. Limit on sensitivity

The analysis of the undoped measurements in section 7.3.2 leads to

$$I_0 = (0.336 \pm 0.019)\ \text{pA}$$

as stated in equation 7.6.

The current I_0 is different from zero with a 17 σ confidence level. In section 7.3.3 the krypton fraction in pure xenon is estimated to $c_0\left(\frac{\text{Kr}}{\text{Xe}}\right) = (1.1 \pm 0.4)$ ppb which corresponds to a measurable current of $I_0 = 0.336$ pA. As no xenon sample with a smaller krypton contamination is available, the sensitivity of the CT-MS technique has to be estimated with respect to the lowest detectable current I_0.

Referring to the 1 σ error of I_0 gives rise to the smallest measurable krypton concentration of

$$\frac{0.019}{0.336} \cdot (1.1 \pm 0.4)\ \text{ppb} = (62 \pm 23)\ \text{ppt} \tag{7.19}$$

Hence a sensitivity of ~ 100 ppt is stated. However, this does not necessarily mean that the described CT-MS technique provides 100 ppt accuracy, as the uncertainties are still not fully understood and have to be constrained by a reliable absolute calibration.

7.4. Summary of trace gas analysis of krypton

The presented technique of cold trap enhanced mass spectrometry provides a sensitivity of at least (6.5 ± 1.5) ppb $\frac{\text{Kr}}{\text{Xe}}$.

By reducing the effective pumping speed of the turbo molecular pump the sensitivity is further improved to ~ 100 ppt $\frac{\text{Kr}}{\text{Xe}}$. Hence the in-situ contamination of krypton in commercially bought xenon from *AirLiquide* could be determined to (1.1 ± 0.4) ppb.

With respect to the natural abundances of krypton the analyzed xenon samples consist of $(1.7 \pm 0.5) \cdot 10^{-20}\, \frac{^{85}\text{Kr}}{\text{Xe}}$. This fraction would cause a background of (33 ± 12) mdru, assuming the conditions of the XENON100 detector.

The aimed total background of XENON1T is < 0.1 mdru. Consequently a reduction of krypton to the sub-ppt level by distillation is necessary when upscaling the detector.

8. Analysis of additional features of the experiment

In this chapter some physical effects arising in the experiment, which do not belong to the main topic of this thesis, are discussed.
The first section deals with the contamination at $\frac{\mathrm{m}}{\mathrm{z}} = 78$ Th and gives several approaches in order to solve this problem.
Furthermore, the time delay of krypton signals after introducing the sample is discussed.
Finally, the technique of CT-MS is applied to other gas species than krypton.

8.1. Background around $\frac{\mathbf{m}}{\mathbf{z}} = 78$ Th

There was a drastic increase of the signal around $\frac{\mathrm{m}}{\mathrm{z}} = 78$ Th at low concentration, after the partial closing of the gate valve to the turbo molecular pump was tried out for the first time.
The high intensity at $\frac{\mathrm{m}}{\mathrm{z}} = 78$ Th shows up after the sample is introduced and does not vanish as fast as the other signals do after closing the leak-valve.
The following list shows isobars around $\frac{\mathrm{m}}{\mathrm{z}} = 78$ Th existing in nature which could cause this effect.

i) Triple ionized thorium $\frac{m}{z} = \frac{232.04}{3} = 77.4$ Th
As the filament of the ion source is made of an iridium wire with thorium-oxide, thorium might be a source of contamination. High pressure exposure of the filament during the measurements might have led to damages and therefore to a release of thorium ions. However, as no signal was recorded around $\frac{232.04}{2} = 116.02$ Th, this hypothesis is rather unlikely.

ii) Diffusion pump oil $\frac{m}{z} = 78$ Th
Although diffusion pump oil has the observed $\frac{m}{z}$ ratio it can be ruled out, as only dry compressing vacuum pumps were used in the experiment.

iii) Benzene $\mathrm{m}(C_6H_6)$=78.11 amu
Benzene, especially its most frequent isotopic composition $^{12}C_6H_6$ with 78.00 amu, is so far the most likely candidate for the measured values around $\frac{\mathrm{m}}{\mathrm{z}} = 78$ Th at low concentrations of krypton. Two possible origins of benzene in this experiment are known so far. Firstly, it could naturally be present in the xenon sample, as it consists of a specified fraction of hydrocarbons of ≤ 500 ppb. However, a counter-argument is that the signal showed up after the investigation of the enhancement by closing the valve to the turbo molecular pump. Assuming an in-situ contamination of the xenon one expects the signal to show up at each measurement, which is not the case. Secondly, the gate valve itself consists of elastomeric sealings which might release hydrocarbons such as benzene. This hypothesis is underlined by the fact that the contamination did not show up while fully closing the gate valve, as the elastomeric sealing match the outer part of the valve. This hypothesis is in agreement with the recorded signal of $\frac{m}{z} = 78$ Th, which does not vanish by closing

the leak-valve. However, the fact that the signal shows up after introducing the sample gas constrains this assumption.

8.2. Time delay of krypton signal

The time delays in krypton signals varying between $20 - 50$ s from start of the measurement hint at some unexpected physics. According to the conductivities calculated in chapter 5 one would expect a constant propagation time for each element. Moreover, krypton has a higher velocity than xenon and should therefore reach the main chamber first. Evidence of this can be seen in the time evolution plots of several ppm of artificial doping, as the bump in the krypton signal is visible in the absolute pressure evolution as well. The constant pressure in the main chamber preserved even after closing the leak-valve most likely corresponds to the xenon vapor pressure emerging from the cold trap.

An explanation for this time effect could be a marginal freeze out of krypton inside the cold trap. Assuming absorption of several monolayers of krypton or trapped krypton in xenon ice both gives rise to a time delay. Hence the time dependence on krypton concentration can be explained by the following hypothesis. As the flow rate of krypton decreases with lower concentrations the time until the cold trap is saturated with krypton increases.

Time delay and evaporation of pure krypton samples

In addition to the krypton in xenon measurements pure krypton samples have been analyzed in order to rule out the assumption that krypton gets trapped by xenon ice inside the cold trap.

A mixing chamber similar to the previously discussed one consisting only of two equal sized volumes without a pressure gauge was filled with pure krypton and connected to the leak-valve. The sample inside the volume directly connected to the leak-valve is introduced to the system while the valve in between the two volumes is kept close. Afterwards the krypton which was stored in the second volume is expanded into the first one. Therefore the input pressure is halved. By repeating this procedure the amount of krypton introduced into the system is reduced by a factor of 2 in each measurement. Moreover, the flow rate is assumed to decrease with respect to the input pressure as well. Figure 8.1 shows the time dependence of the set of pure krypton measurements. With decreasing input pressure the time delay until a first rise in krypton is detected increases. Because of the lower input pressure the flow through the leak-valve reduces as well. An accumulation in the main chamber is unlikely as the turbo molecular pump is operating at maximum pumping speed[1]. Hence an explanation for the time delay would be some monolayer absorption of krypton inside the cold trap. As the flow rate decreases with lower input pressure the time until the cold trap is saturated increases. Evidence for this hypothesis can be seen in figure 8.2. After each measurement the cold trap was emptied by taking the nitrogen reservoir away from the copper tubing. Right after taking away the cold trap, the Transpector2 mass filter recorded a sharp increase in current which vanishes quickly. Figure 8.2 shows the integrated current of the evaporation peaks at $\frac{m}{z} = 84$ Th after disabling the cold trap according to the input pressure of ^{84}Kr. From this plot it can be concluded that a certain amount of krypton freezes out inside the cold trap and evaporates after taking away the cold trap.

---

[1] That is no enhancement by closing the gate valve to the turbo molecular pump.

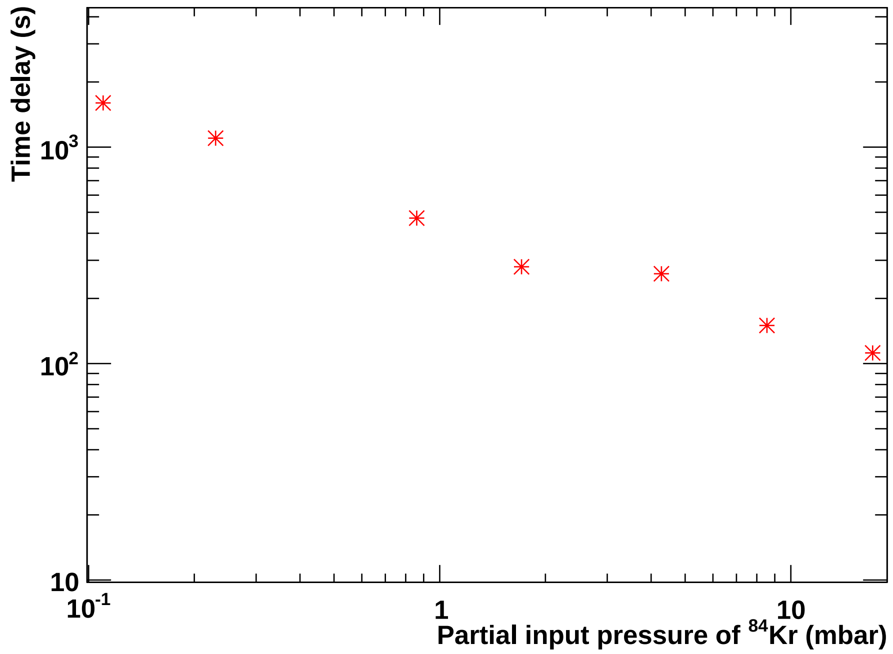

Figure 8.1.: *Time delay of the* ^{84}*Kr signal according to partial input pressure of* ^{84}*Kr which is related to the total flow rate.*

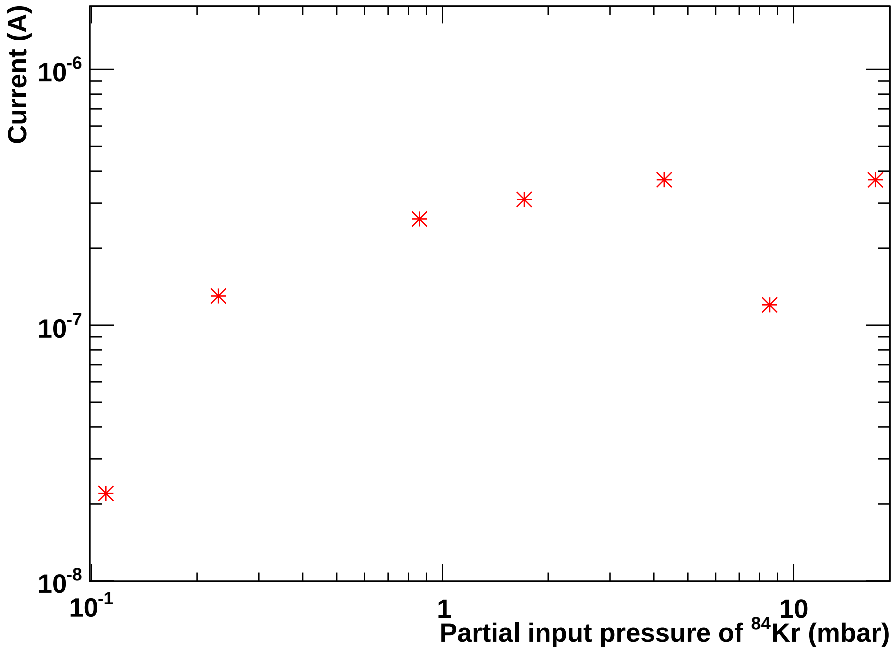

Figure 8.2.: *Integrated currents of the* ^{84}*Kr evaporation peaks after disabling the cold trap with respect to partial input pressure of* ^{84}*Kr.*

8.3. Applications for other impurities - Proof of principle

The technique presented in chapter 5 is not only advantageous for detecting trace amounts of krypton in xenon, but also suited for other substances.
In principle all elements with a higher vapor pressure than xenon at liquid nitrogen temperature can be analyzed with this technique, benefiting from the enhancement by the cold trap. At this point only one example is given, namely detecting helium in pure xenon.

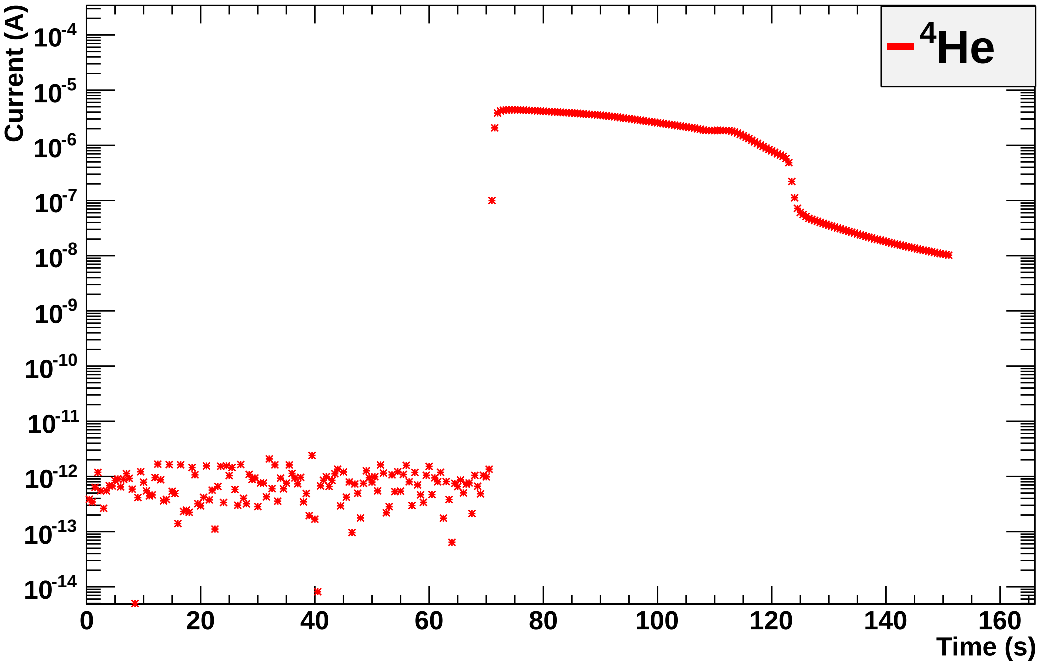

Figure 8.3.: *Time evolution of helium in pure xenon. The sample was introduced at* $t = 70$ *s. The sharp decrease in intensity at* $t \approx 120$ *s is caused by re-opening the gate valve to the turbo molecular pump.*

Figure 8.3 shows the time evolution of helium in pure xenon using the additional enhancement by reduction of the effective pumping speed of the turbo molecular pump. The sample was introduced at $t = 70$ s causing a prompt signal increase. The recorded signal is much higher than the signal measured from pure krypton, although the ionization efficiency for helium is smaller than for krypton. However, the helium and krypton signals cannot be compared directly, as helium has different propagation velocities as well as different vapor pressure at 77 kelvin. Furthermore, the pumping speed for helium also differs from krypton and xenon.
As mentioned previously when describing the time evolution of krypton in xenon in chapter 7 the pressure evolution showed a behavior differing from the recorded krypton signals. A rise in pressure before krypton or xenon reach the main chamber could be explained by additional components present in the xenon which propagate faster through the system than the measured components. Helium fulfills these properties and therefore could give rise to the total pressure measured in the main chamber right after introducing the sample.
The analysis of helium in pure xenon verifies that the CT-MS technique is not only able to detect krypton in xenon but also other gas species.

9. Summary and outlook

The technique of cold trap enhanced mass spectrometry based on the principle developed by [Dob11] et al. has successfully been included as a part of the gas analysis and purification system at Münster. The CT-MS technique can be used as a diagnostic tool for the cryogenic distillation column currently in development.

The first measurements, presented in chapter 7, result in an upper limit for the sensitivity of the CT-MS technique of (6.5 ± 1.5) ppb $\frac{\mathrm{Kr}}{\mathrm{Xe}}$.

Furthermore, an enhancement due to reducing the effective pumping speed of the turbo molecular pump has successfully been tested, leading to an improved sensitivity to the level of ~ 100 ppt $\frac{\mathrm{Kr}}{\mathrm{Xe}}$.

The in-situ krypton concentration of commercially available xenon from *AirLiquide*, which is specified at < 10 ppb $\frac{\mathrm{Kr}}{\mathrm{Xe}}$ has been determined to be (1.1 ± 0.4) ppb, which is a factor 10 improvement in precision.

The CT-MS technique is in principle non-destructive. Although the sample is consumed during the measurement, its mass is small so that the technique can still be called non-destructive. As an optional improvement, the frozen xenon gas inside the cold trap could be recovered in order to address this issue. The recovery would in parallel provide a reduction in krypton. The feasibility of this purification technique has been investigated by [Leo10] and [Dob11].

Moreover, the recovery of the xenon gas would offer a significant improvement of the sensitivity. As mentioned in section 5.4 an increase in flow rate through the leak-valve would only increase the krypton flow into the main chamber, as the xenon gas is held at constant vapor pressure. Therefore the sensitivity scales proportionally to the flow rate. At the moment the flow rate is limited by the amount of gas introduced into the system corresponding to the measuring time until the sample is consumed. By recovering the xenon the measurement would be non-destructive independent of the amount of sample gas.

Furthermore, the technique of CT-MS has successfully been adapted to other gas species such as to the detection of trace amounts of helium in xenon.

Surface effects which cause a slight amount of krypton to freeze inside the cold trap have been observed by measuring a time delay related to the krypton concentration and the evaporation of ^{84}Kr after the measurement.

Moreover, the enhancement by the cold trap could be improved in two ways. Firstly, the geometry of the cold trap could be investigated in more detail. This might become necessary when going to much higher flow rates, as the frozen xenon gas would be able to completely block the cold trap. Secondly, a much higher amplification could be achieved by going to temperatures below 77 kelvin by using a cold head, as the difference in vapor pressure is then even more exploited.

In order to minimize the systematic uncertainties of the measurement the reduction in effective pumping speed due to closing the gate valve to the turbo molecular pump has to be automated or rather become reproducible. This could be achieved by applying an additional cover plate in front of the turbo molecular pump.

To conclude, while some improvement is possible, the system, as it is, is ready for use and performs already well to allow detection on the ppb and sub-ppb level.

A. Appendix

A.1. Ionization and scintillation processes due to WIMP scattering

Scintillation light emerging from liquid xenon is caused by the decay of exited dimers[1] into the ground state.

Excited xenon dimers Xe_2^* are produced both by direct excitation and electron-ion recombination due to interactions with WIMPs [Apr10d].

i) **Direct excitation due to WIMP interactions**
Excited xenon atoms Xe^* arising from WIMP interactions combine with un-excited xenon atoms Xe, forming an exciton Xe_2^*. These excitons decay within picoseconds, emitting VUV[2] photons at a wavelength of $\lambda = 178$ nm [Apr10d].

$$\mathrm{Xe} + \mathrm{WIMP} \rightarrow \mathrm{Xe}^* \tag{A.1}$$
$$\mathrm{Xe}^* + \mathrm{Xe} + \mathrm{Xe} \rightarrow \mathrm{Xe}_2^* + \mathrm{Xe} \tag{A.2}$$
$$\mathrm{Xe}_2^* \rightarrow 2\,\mathrm{Xe} + h\nu \tag{A.3}$$

ii) **Ionization due to WIMP interactions**
The ionized xenon atoms Xe^+ combine with un-ionized xenon atoms Xe. If the arising electrons are not drifted away the excitons Xe_2^+ recombine under an energy release of E_{heat} and give rise to excited xenon atoms Xe^*, which in turn produce VUV photons.

$$\mathrm{Xe} + \mathrm{WIMP} \rightarrow \mathrm{Xe}^+ + e^- \tag{A.4}$$
$$\mathrm{Xe}^+ + \mathrm{Xe} \rightarrow \mathrm{Xe}_2^+ \tag{A.5}$$
$$\mathrm{Xe}_2^+ + e^- \rightarrow \mathrm{Xe}^{**} + \mathrm{Xe} \tag{A.6}$$
$$\mathrm{Xe}^{**} \rightarrow \mathrm{Xe}^* + E_{\text{heat}} \tag{A.7}$$
$$\mathrm{Xe}^* + \mathrm{Xe} + \mathrm{Xe} \rightarrow \mathrm{Xe}_2^* + \mathrm{Xe} \tag{A.8}$$
$$\mathrm{Xe}_2^* \rightarrow 2\mathrm{Xe} + h\nu \tag{A.9}$$

The second process is suppressed by electronegative impurities, as they reduce the mean lifetime of electrons.

As the scintillation light arises from the first excited level, Xe^* it is not absorbed by the xenon atoms and can therefore be detected by PMT arrays at the top and bottom of the TPC [Dok81].

---

[1] Also referred to as *excimer*.

[2] VUV = vacuum ultraviolet

A.2. Calculations for the differential pumping section

Calculations for the differential low conducting pumping section shown in figure A.1 for xenon, krypton and helium gas at T=293.15 K, respectively:

$$\begin{aligned} C_{\mathrm{dpa}}(\mathrm{Xe}) &= \frac{\pi}{16} \cdot \underbrace{\sqrt{\frac{8 \cdot R \cdot T}{\pi \cdot M}}}_{\bar{c}} \cdot d^2 \cdot \frac{14 + 4\frac{l}{d}}{14 + 18\frac{l}{d} + 3\left(\frac{l}{d}\right)^2} \quad ; \quad M_{\mathrm{Xe}} = 0.131293\,\frac{\mathrm{kg}}{\mathrm{mol}} \\ &= \frac{\pi}{16} \cdot 217.426\,\frac{\mathrm{m}}{\mathrm{s}} \cdot \left[\frac{1}{0{,}189\,\mathrm{mm}^2} + \frac{1}{3{,}658\,\mathrm{mm}^2}\right]^{-1} \\ &= 7.67 \cdot 10^{-3}\,\frac{\mathrm{L}}{s} \end{aligned} \tag{A.10}$$

$$\begin{aligned} C_{\mathrm{dpa}}(\mathrm{Kr}) &= \frac{\pi}{16} \cdot \underbrace{\sqrt{\frac{8 \cdot R \cdot T}{\pi \cdot M}}}_{\bar{c}} \cdot d^2 \cdot \frac{14 + 4\frac{l}{d}}{14 + 18\frac{l}{d} + 3\left(\frac{l}{d}\right)^2} \quad ; \quad M_{\mathrm{Kr}} = 0.083798\,\frac{\mathrm{kg}}{\mathrm{mol}} \\ &= \frac{\pi}{16} \cdot 272.154\,\frac{\mathrm{m}}{\mathrm{s}} \cdot \left[\frac{1}{0{,}189\,\mathrm{mm}^2} + \frac{1}{3{,}658\,\mathrm{mm}^2}\right]^{-1} \\ &= 9.60 \cdot 10^{-3}\,\frac{\mathrm{L}}{s} \end{aligned} \tag{A.11}$$

$$\begin{aligned} C_{\mathrm{dpa}}(\mathrm{He}) &= \frac{\pi}{16} \cdot \underbrace{\sqrt{\frac{8 \cdot R \cdot T}{\pi \cdot M}}}_{\bar{c}} \cdot d^2 \cdot \frac{14 + 4\frac{l}{d}}{14 + 18\frac{l}{d} + 3\left(\frac{l}{d}\right)^2} \quad ; \quad M_{\mathrm{He}} = 0.004003\,\frac{\mathrm{kg}}{\mathrm{mol}} \\ &= \frac{\pi}{16} \cdot 1245.2\,\frac{\mathrm{m}}{\mathrm{s}} \cdot \left[\frac{1}{0{,}189\,\mathrm{mm}^2} + \frac{1}{3{,}658\,\mathrm{mm}^2}\right]^{-1} \\ &= 0.0439\,\frac{\mathrm{L}}{s} \end{aligned} \tag{A.12}$$

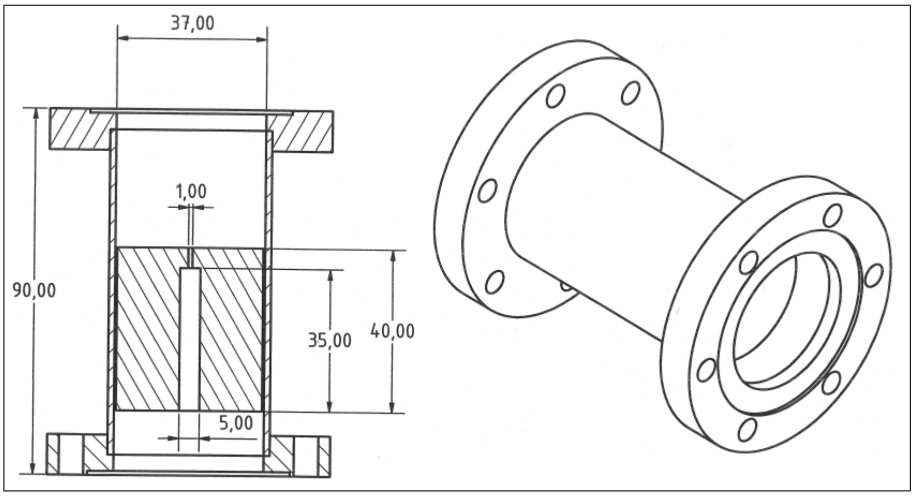

Figure A.1.: *Technical drawing of the differential low conduction pumping section.*

A.3. Electron ionization cross-sections

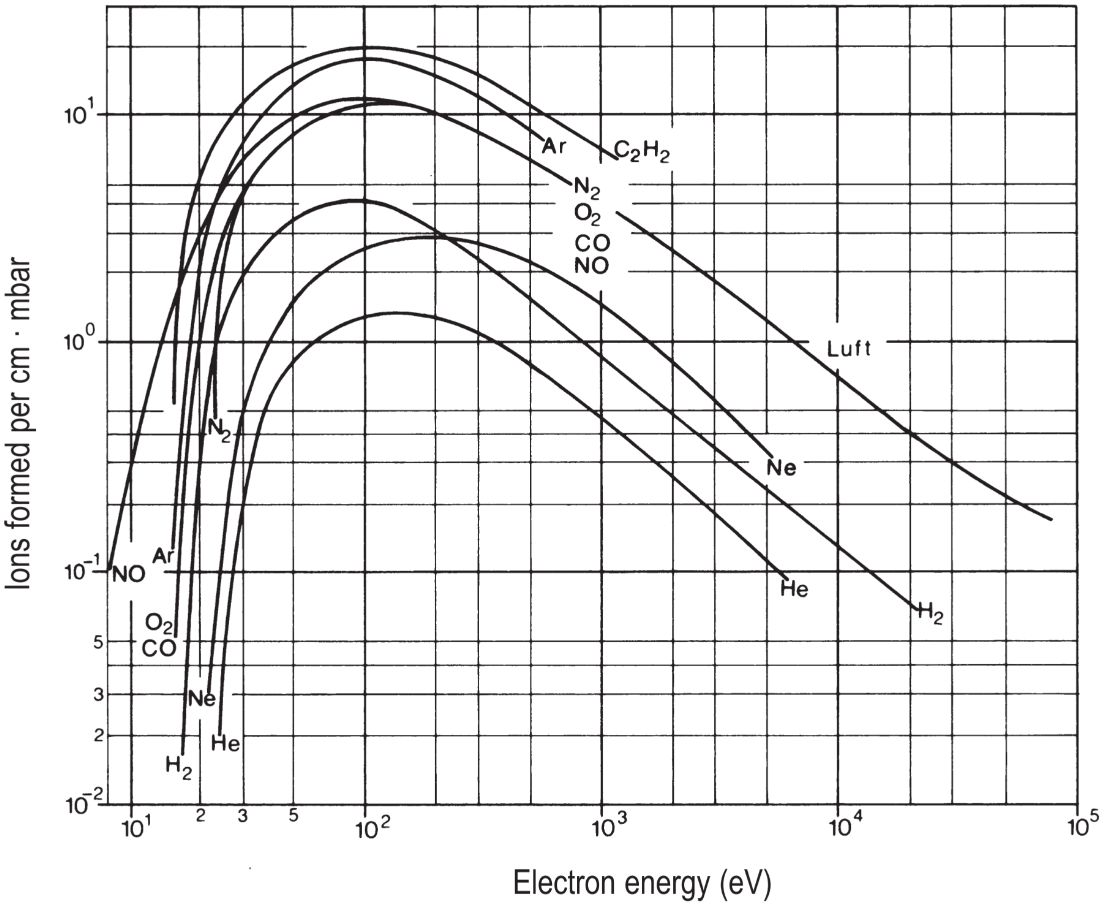

Figure A.2.: *Dependence of ionization cross-section on electron energy for different elements [Umr07].*

A.4. Hit pattern of the XENON100 TPC

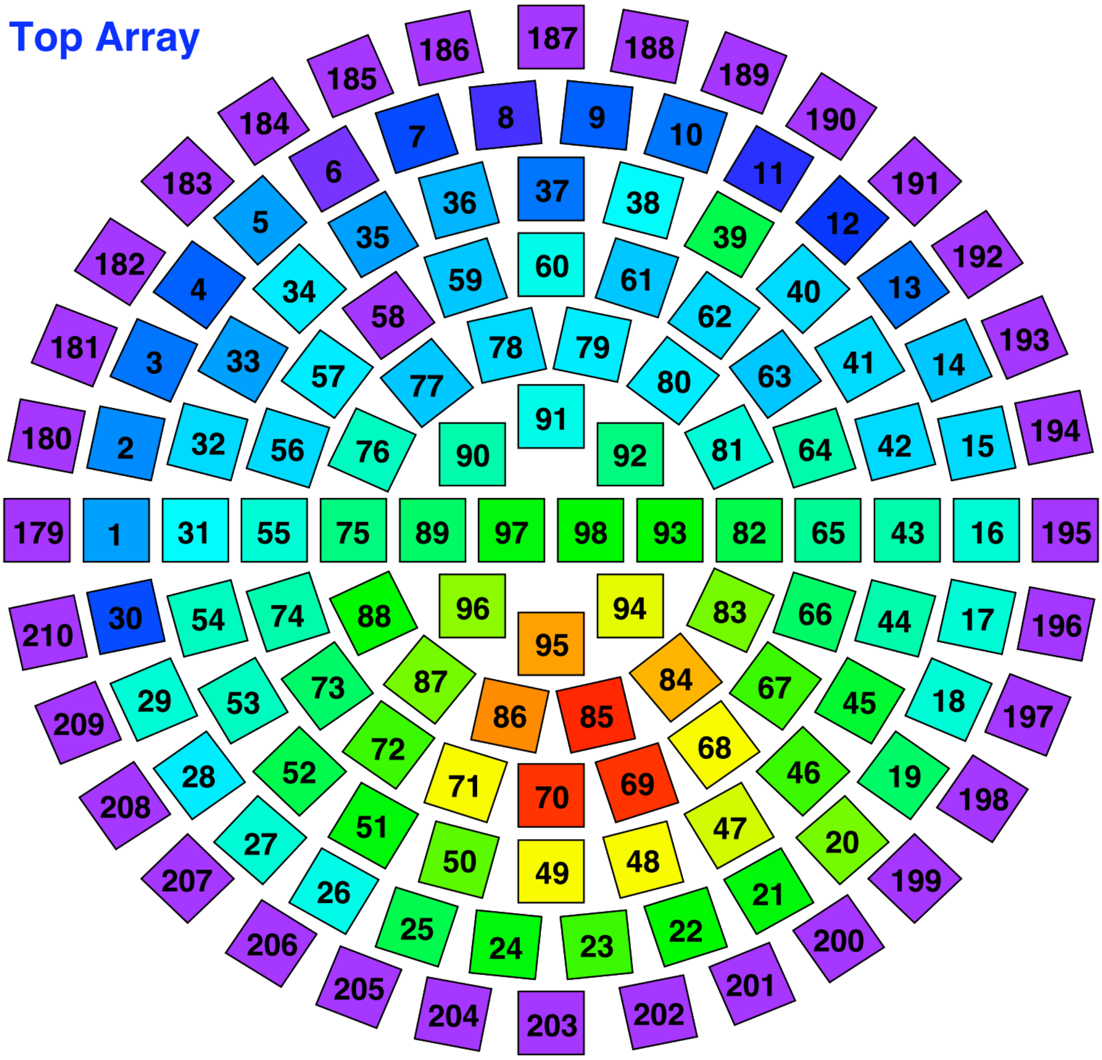

Figure A.3.: *Typical hit pattern of a S2 signal on the top PMT array of the XENON100 TPC. Radial position reconstruction in the x-y plane provides a resolution of about 2 mm [Apr08].*

A.5. Preliminary XENON1T TPC

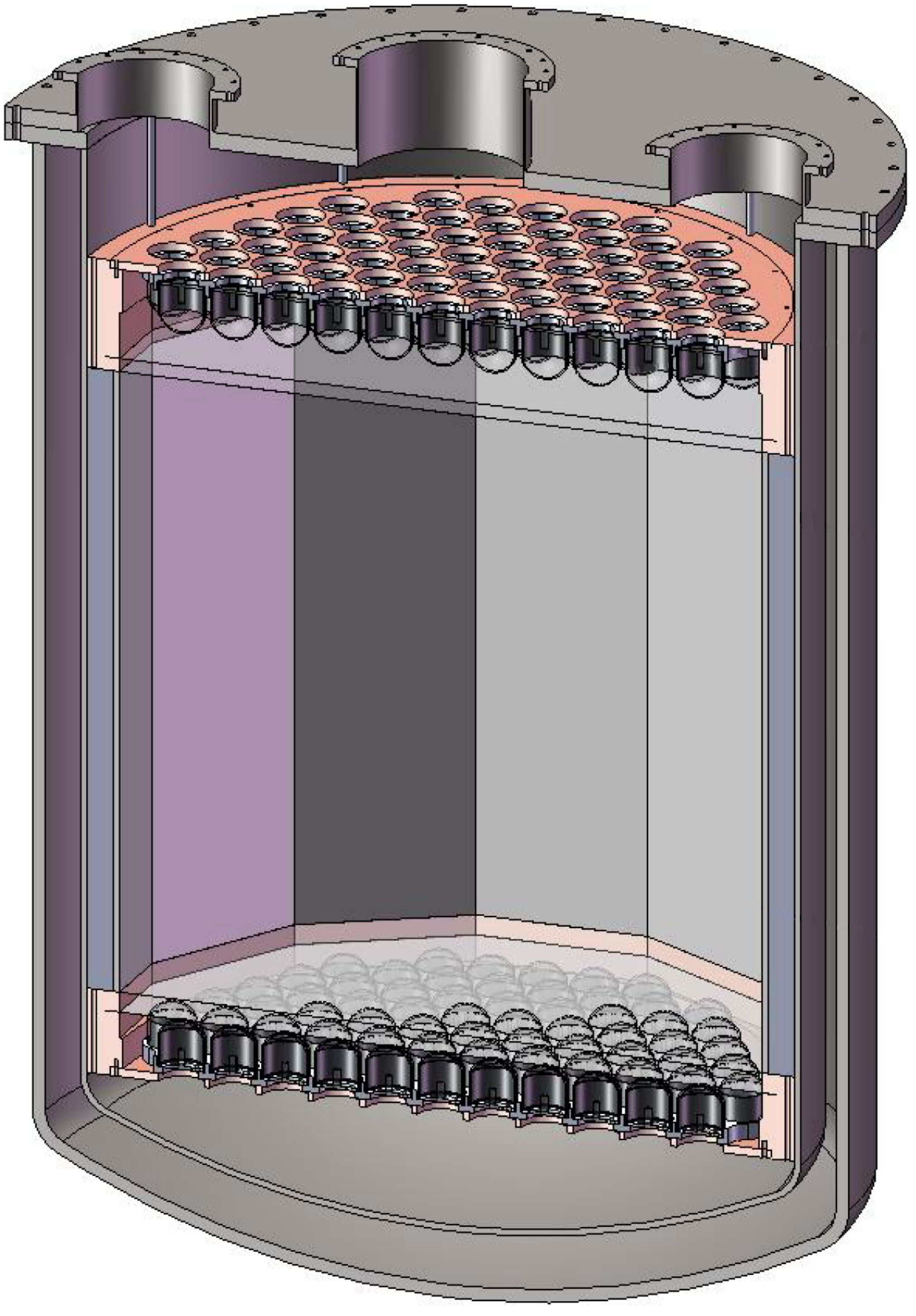

Figure A.4.: *Three dimensional CAT drawing of the preliminary XENON1T TPC. The double walled cryostat vessel and the top and bottom arrays of photo sensitive detectors are visible [Courtesy of the XENON100 Collaboration].*

A.6. Tables and data

Doping level	^{84}Kr	^{86}Kr	^{82}Kr	^{83}Kr	^{80}Kr	^{78}Kr	^{85}Kr
8.8e-06	3.56e-10	1.04e-10	7.46e-11	7.36e-11	1.51e-11	2.45e-12	2.69e-13
1.1e-06	9.82e-12	3.02e-12	2.06e-12	2.04e-12	3.99e-13	7.81e-14	3.21e-14
1.5e-07	5.70e-13	1.82e-13	1.27e-13	1.23e-13	5.02e-14	4.99e-14	4.11e-14
2.0e-08	6.31e-14	3.99e-14	3.94e-14	4.91e-14	3.07e-14	5.74e-14	4.93e-14

Table A.1.: *Normalized and integrated currents of run 6 sorted by natural abundance.*

Doping level	^{84}Kr	^{86}Kr	^{82}Kr	^{83}Kr	^{80}Kr	^{78}Kr	^{85}Kr
9.0e-06	1.36e-08	3.86e-09	2.72e-09	2.69e-09	5.50e-10	8.70e-11	7.67e-12
1.5e-07	3.53e-11	1.05e-11	7.29e-12	7.24e-12	1.48e-12	6.77e-13	5.58e-14
2.0e-08	2.63e-12	8.25e-13	5.95e-13	5.68e-13	1.45e-13	4.08e-13	9.00e-14
Pure xenon	3.22e-13	1.07e-13	1.46e-13	1.13e-13	6.86e-14	4.43e-13	1.02e-13
Pure xenon	1.10e-12	3.35e-13	2.46e-13	2.44e-13	8.05e-14	4.07e-13	5.15e-14
Pure xenon	2.56e-13	7.71e-14	8.12e-14	5.78e-14	3.12e-14	3.08e-13	3.03e-14
Pure xenon	2.40e-13	7.70e-14	8.01e-14	7.03e-14	5.56e-14	3.26e-13	4.64e-14
Pure xenon	2.10e-13	5.73e-14	6.90e-14	5.40e-14	2.53e-14	2.35e-13	3.03e-14

Table A.2.: *Normalized and integrated currents of run 7 sorted by natural abundance.*

Impurities	Specified molar fraction	Measured molar fraction
H_2O	$\leq$ 1.00 ppm	0.19 ppm
O_2	$\leq$ 1.00 ppm	$\leq$ 0.05 ppm
N_2	$\leq$ 2.00 ppm	0.15 ppm
H_2	$\leq$ 1.00 ppm	$\leq$ 0.05 ppm
Ar	$\leq$ 1.00 ppm	$\leq$ 0.05 ppm
C_nH_m	$\leq$ 0.50 ppm	$\leq$ 0.05 ppm
$CO + CO_2$	$\leq$ 1.00 ppm	$\leq$ 0.05 ppm
CF_4	$\leq$ 0.10 ppm	$\leq$ 0.05 ppm
C_2F_6	$\leq$ 0.10 ppm	$\leq$ 0.05 ppm
SF_6	$\leq$ 0.10 ppm	$\leq$ 0.05 ppm
Kr	$\leq$ 0.01 ppm	non-detectable

Table A.3.: *Xenon data sheet by Air Liquide. Measuring uncertainty of $2\sigma = 95$ % Confidence Interval. Detection threshold of 0.05 ppm.*

Gas	Mass	Nat. Abd.
Krypton	78 amu	0.35 %
Krypton	80 amu	2.25 %
Krypton	82 amu	11.6 %
Krypton	83 amu	11.5 %
Krypton	84 amu	57.0 %
Krypton	85 amu	———
Krypton	86 amu	17.3 %

Gas	Mass	Nat. Abd.
Xenon	128 amu	1.9 %
Xenon	129 amu	26.4 %
Xenon	130 amu	4.1 %
Xenon	131 amu	21.3 %
Xenon	132 amu	26.9 %
Xenon	134 amu	10.4 %
Xenon	136 amu	8.9 %

Table A.4.: *Selection of mass numbers and their natural abundance of krypton (left) and xenon (right) isotopes [Gro04].*

Gas	Pumping speed S	Compression ratio
N_2	$300\ \mathrm{L} \cdot \mathrm{s}^{-1}$	$> 1.0 \cdot 10^{10}$
Ar	$260\ \mathrm{L} \cdot \mathrm{s}^{-1}$	———
He	$260\ \mathrm{L} \cdot \mathrm{s}^{-1}$	$9.2 \cdot 10^4$
H_2	$190\ \mathrm{L} \cdot \mathrm{s}^{-1}$	$3.2 \cdot 10^3$

Table A.5.: *Theoretical pumping speed and compression ratio of the MAG W 300 P turbo molecular pump at a nominal rotation speed of 85,800 rpm. Taken from MAG W manual leybold vacuum. The pumping speed for krypton and xenon is assumed to be of the order of* $S(N_2) = 300\,\frac{L}{s}$.

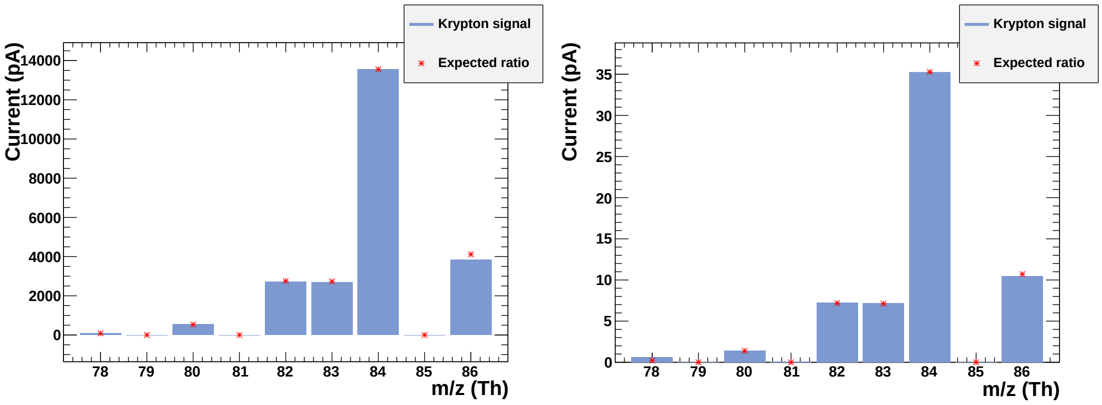

(a) Run 7-01: (9000 ± 289) ppb $\frac{\text{Kr}}{\text{Xe}}$

(b) Run 7-03: (154 ± 7) ppb $\frac{\text{Kr}}{\text{Xe}}$

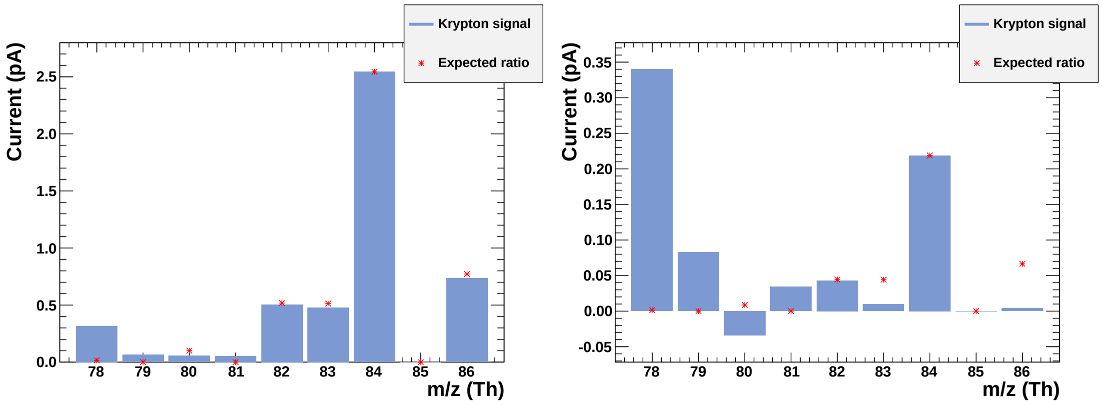

(c) Run 7-04: (20 ± 1) ppb $\frac{\text{Kr}}{\text{Xe}}$

(d) Run 7-05: Pure xenon

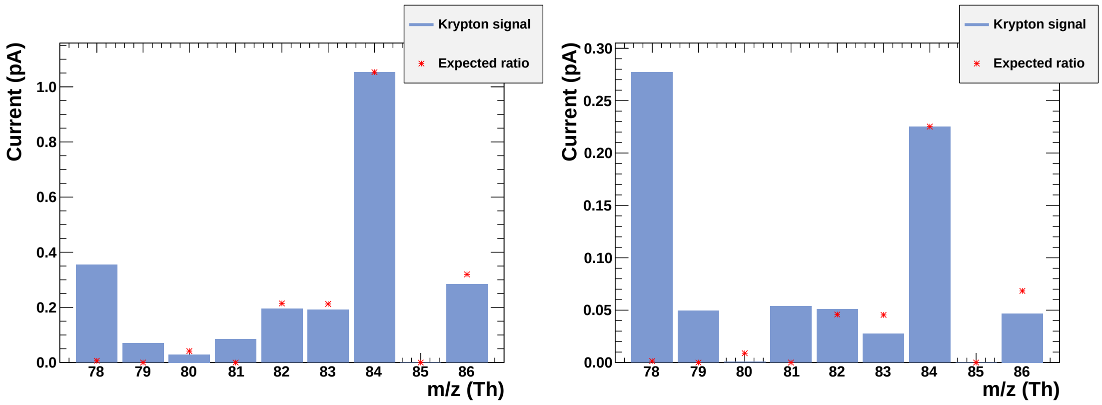

(e) Run 7-06: Pure xenon

(f) Run 7-07: Pure xenon

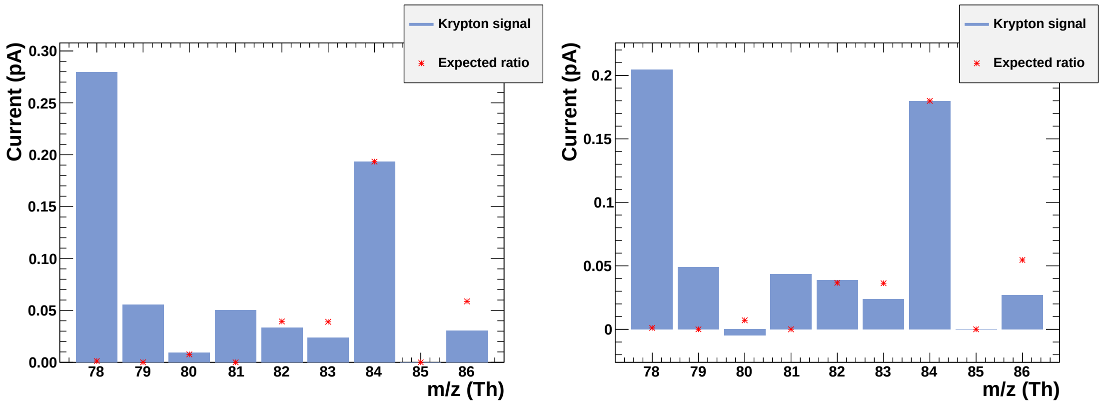

(g) Run 7-08: Pure xenon

(h) Run 7-09: Pure xenon

Figure A.5.: *Measured and expected isotopic ratios of krypton at different artificial concentrations of run 7. The negative values are due to background subtraction.*

A.7. Determination of peak width and position

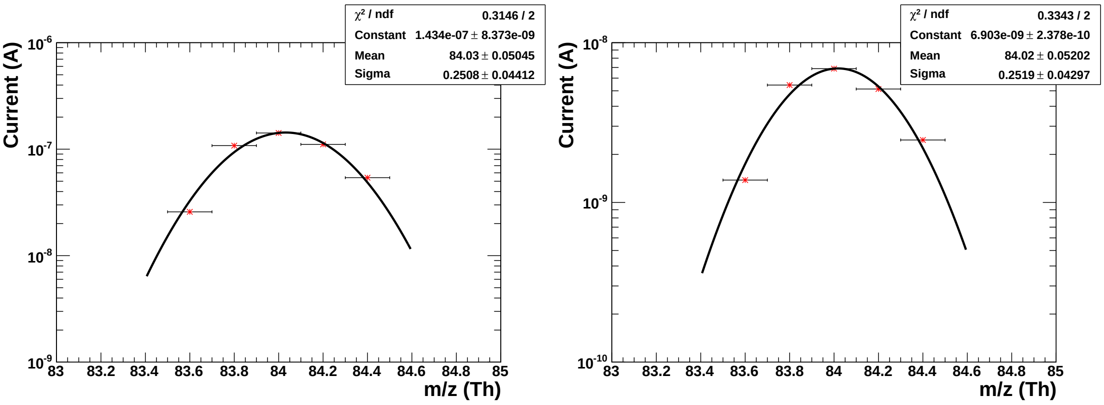

(a) Run 5-01: (17,000 ± 524) ppb $\frac{\mathrm{Kr}}{\mathrm{Xe}}$ (b) Run 5-02: (2500 ± 90) ppb $\frac{\mathrm{Kr}}{\mathrm{Xe}}$

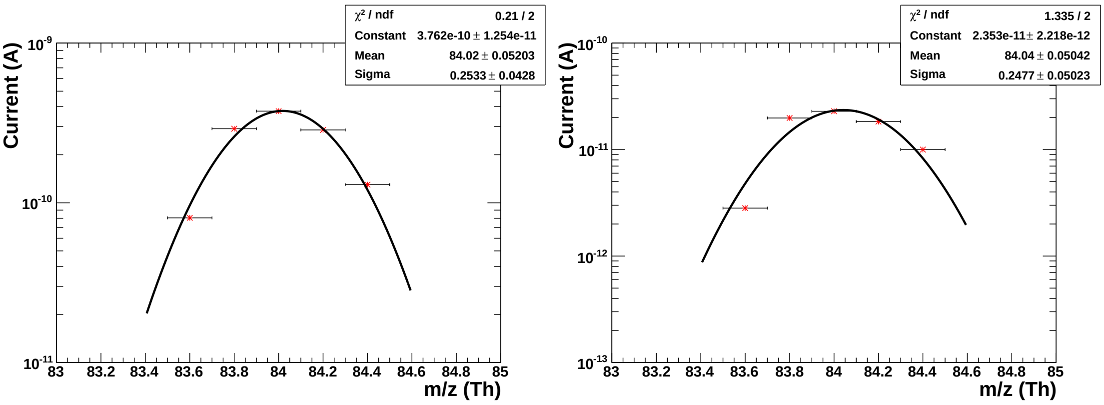

(c) Run 5-03: (334 ± 14) ppb $\frac{\mathrm{Kr}}{\mathrm{Xe}}$ (d) Run 5-04: (44 ± 2) ppb $\frac{\mathrm{Kr}}{\mathrm{Xe}}$

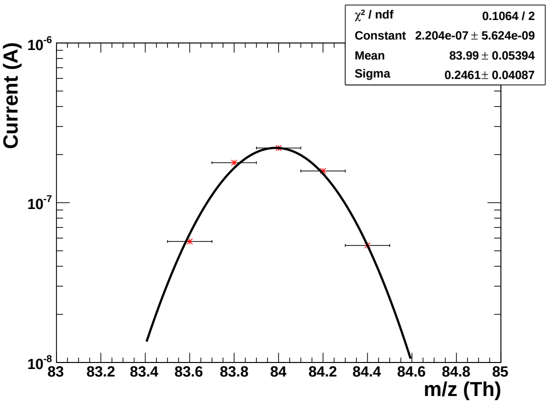

(e) Run 5-06: (30,000 ± 924) ppb $\frac{\mathrm{Kr}}{\mathrm{Xe}}$

Figure A.6.: *Positions of base peaks in run 5. Uncertainties on the* $\frac{m}{z}$ *axis have been accounted by the bin with of 0.1 amu.*

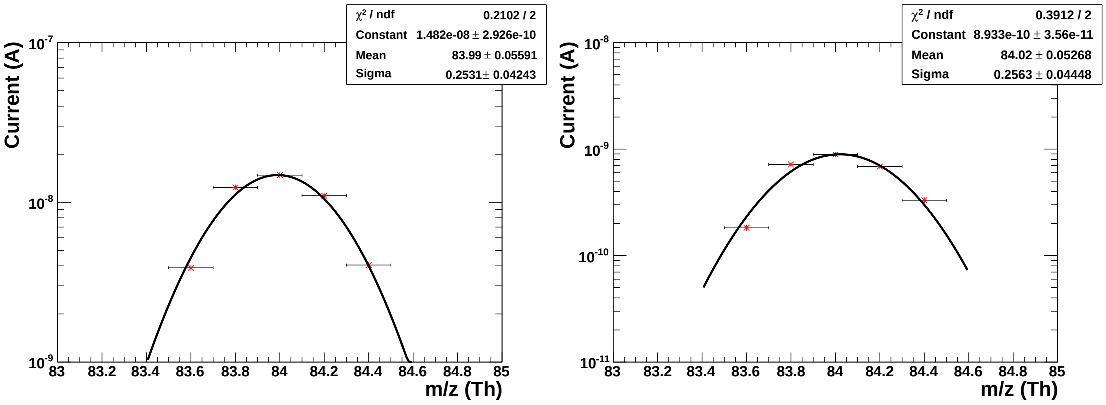

(a) Run 5-07: (4000 ± 144) ppb $\frac{\text{Kr}}{\text{Xe}}$

(b) Run 5-08: (526 ± 22) ppb $\frac{\text{Kr}}{\text{Xe}}$

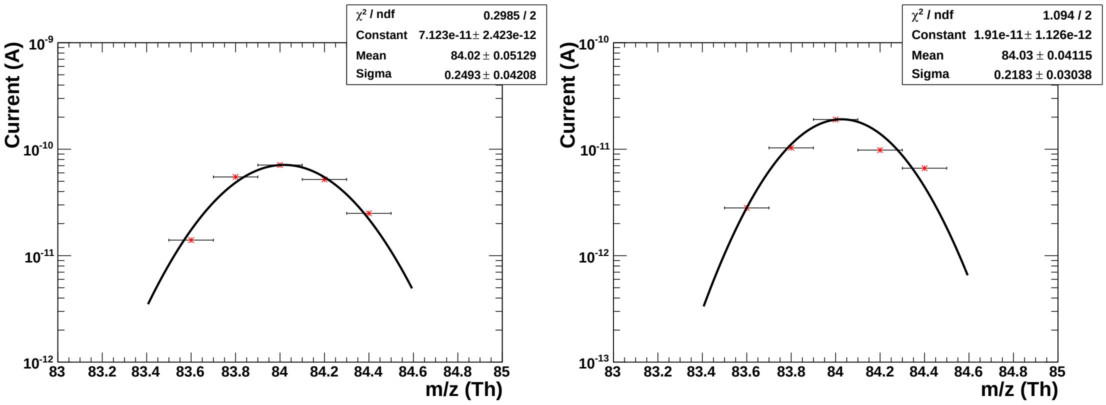

(c) Run 5-09: (69 ± 3) ppb $\frac{\text{Kr}}{\text{Xe}}$

(d) Run 5-10: (33 ± 2) ppb $\frac{\text{Kr}}{\text{Xe}}$

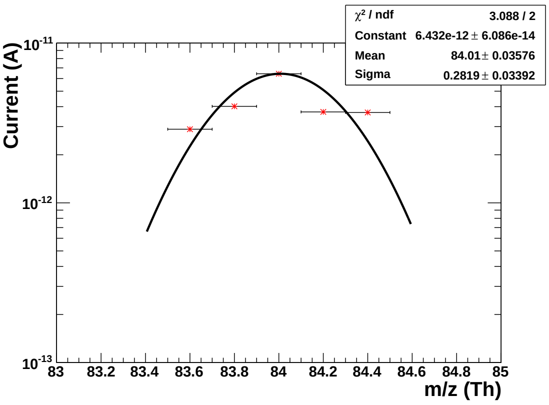

(e) Run 5-11: (16 ± 1) ppb $\frac{\text{Kr}}{\text{Xe}}$

Figure A.7.: *Positions of base peaks in run 5. Uncertainties on the $\frac{m}{z}$ axis have been accounted by the bin with of 0.1 amu.*

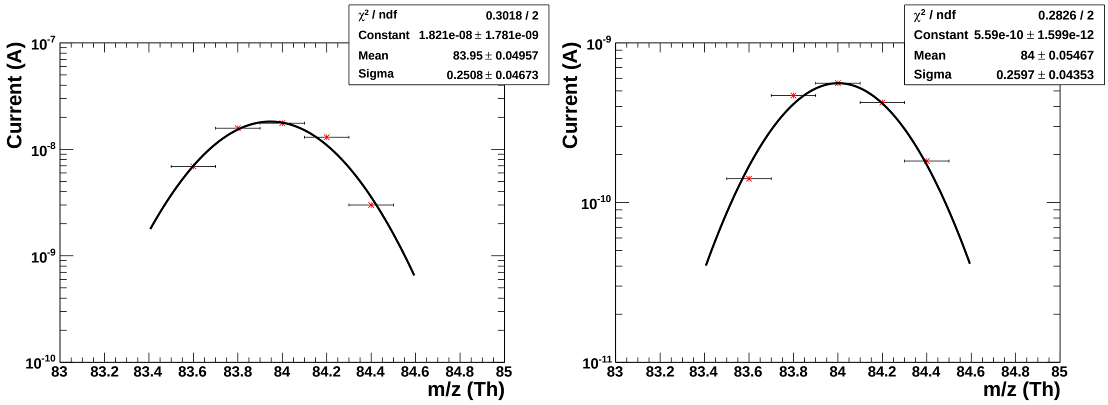

(a) Run 6-01: (8800 ± 282) ppb $\frac{\text{Kr}}{\text{Xe}}$

(b) Run 6-02: (1100 ± 41) ppb $\frac{\text{Kr}}{\text{Xe}}$

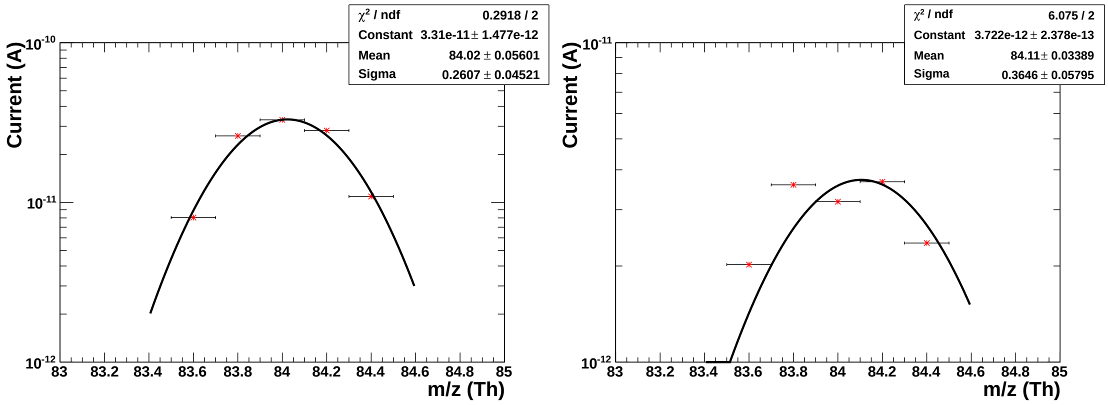

(c) Run 6-03: (150 ± 6) ppb $\frac{\text{Kr}}{\text{Xe}}$

(d) Run 6-04: (20 ± 1) ppb $\frac{\text{Kr}}{\text{Xe}}$

Figure A.8.: *Positions of base peaks in run 6. Uncertainties on the* $\frac{m}{z}$ *axis have been accounted by the bin with of 0.1 amu.*

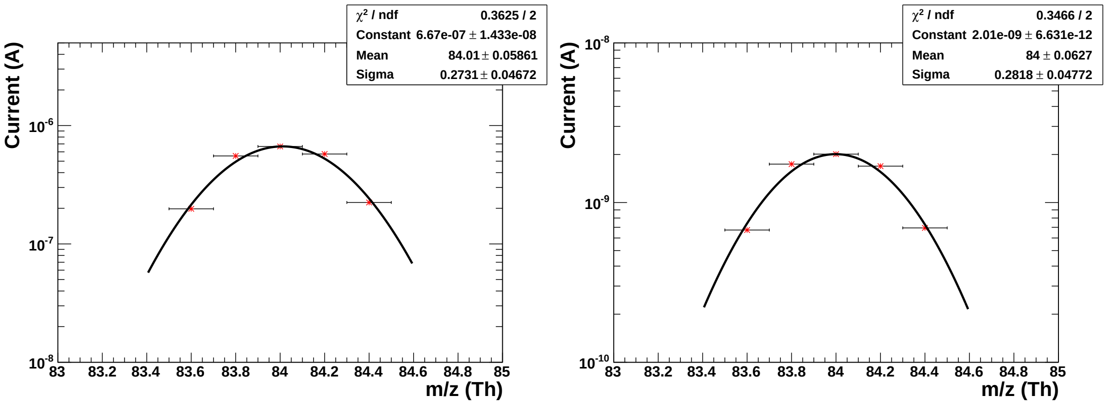

(a) Run 7-01: (9000 ± 289) ppb $\frac{\mathrm{Kr}}{\mathrm{Xe}}$ (b) Run 7-03: (154 ± 7) ppb $\frac{\mathrm{Kr}}{\mathrm{Xe}}$

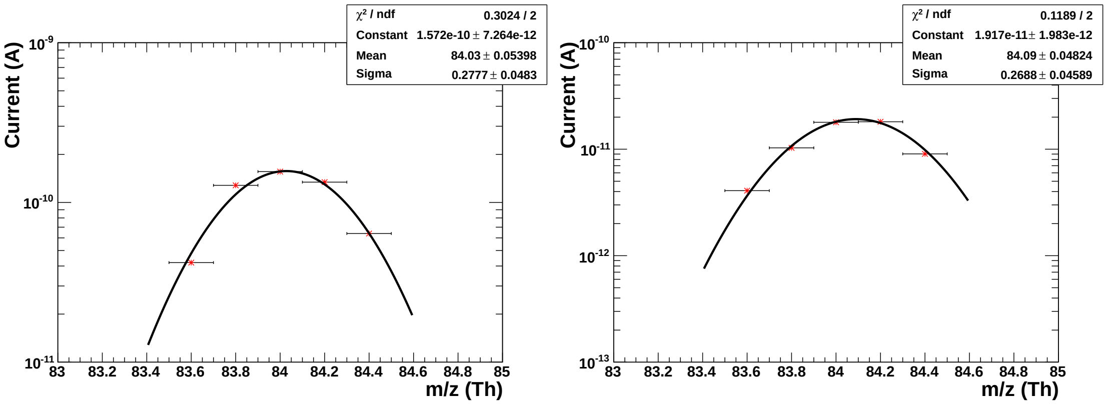

(c) Run 7-04: (20 ± 1) ppb $\frac{\mathrm{Kr}}{\mathrm{Xe}}$ (d) Run 7-05: Pure xenon

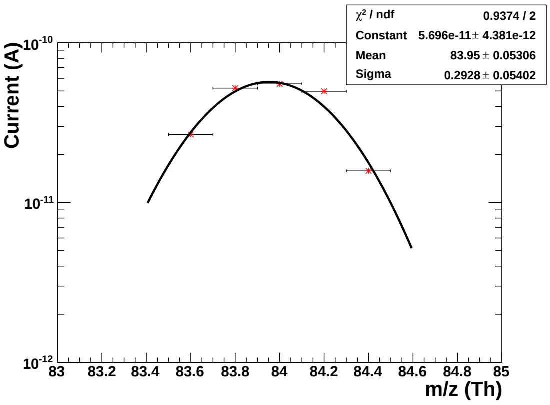

(e) Run 7-06: Pure xenon

Figure A.9.: *Positions of base peaks in run 7. Uncertainties on the $\frac{m}{z}$ axis have been accounted by the bin with of 0.1 amu.*

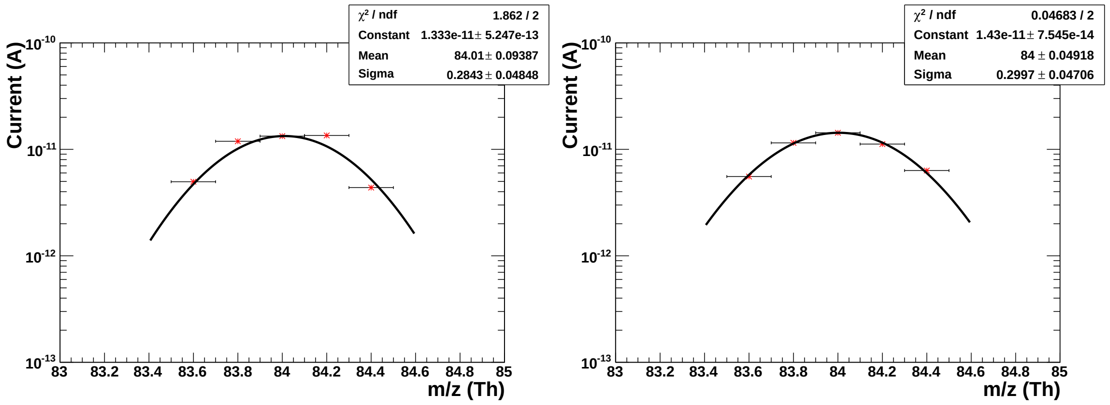

(a) Run 7-07: Pure xenon (b) Run 7-08: Pure xenon

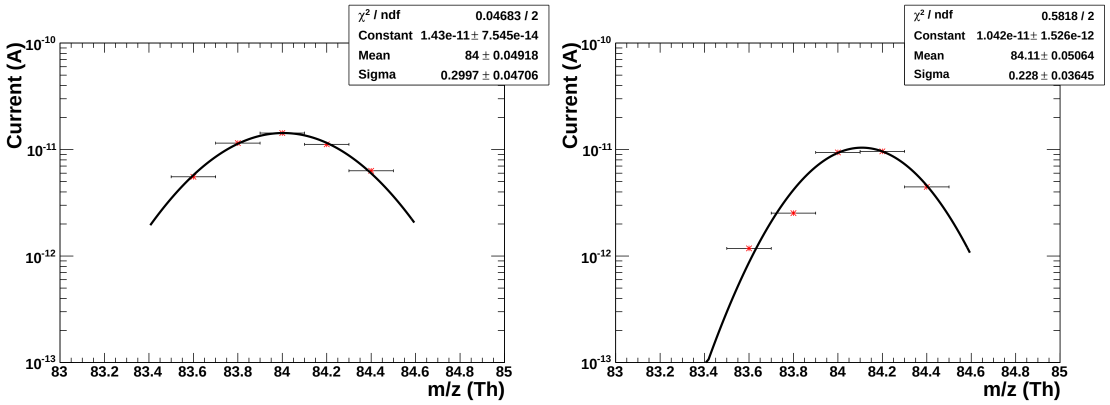

(c) Run 7-09: Pure xenon (d) Run 7-11: Pure xenon

Figure A.10.: *Positions of base peaks in run 7. Uncertainties on the $\frac{m}{z}$ axis have been accounted by the bin with of 0.1 amu.*

List of Figures

Bibliography

[Aal11] C. E. Aalseth et al., Phys. Rev. Lett. 106:131301, 2011
Results from a Search for Light-Mass Dark Matter with a P-type Point Contact Germanium Detector

[Aba11] K. Abazajian et al., arXiv:1109.6291v1 2011
The Halo Model of Large Scale Structure for Warm Dark Matter

[Ack11] N. Ackerman et al. (EXO Collaboration), Phys. Rev. Lett. **107**, 212501 (2011)
Observation of Two-Neutrino Double-Beta Decay in Xe-136 with EXO-200

[Aga04] K. Agashe and G. Servant, Phys. Rev. Lett. 93:231805, 2004
Warped Unification, Proton Stability and Dark Matter

[Alp49] R. A. Alpher and R. C. Herman, Phys. Rev **75** (1949) 1089
Remarks on the Evolution of the Expanding Universe

[Ang08] J. Angle et al. XENON Collaboration, Phys. Rev. Let. **100**, 021303 (2008)
First Results from the XENON10 Dark Matter Experiment at Gran Sasso National Laboratory

[Apr04] E. Aprile et al., IEEE Trans. Nucl. Sci. **51** (2004) 1986

[Apr08] E. Aprile and L. Baudis, Proceedings of Science (IDM2008)
Status and Sensitiviy Projections for the XENON100 Dark Matter Experiment

[Apr09] E. Aprile and T. Zelevinsky, Columbia University January 2009,
Instrument Development for Liquid Xenon Dark Matter Searches: An Atom Trap Trace Analysis System to Measure Ultra-low Krypton Contamination in Xenon

[Apr10a] E. Aprile et al., Technical Design Report of XENON1T at LNGS, October, 2010

[Apr10b] E. Aprile et al., Phys. Rev. Lett. **105**, 131302 (2010),
First Dark Matter Results from the XENON100 Experiment

[Apr10c] E. Aprile et al., Journal of Physics: Conference Series **203** (2010),
The XENON100 Dark Matter Experiment at LNGS: Status and Sensitivity

[Apr10d] E. Aprile and T. Doke, Rev. Mod. Phys. **82**, 2053-2097, 2010
Liquid Xenon Detectors for Particle Physics and Astrophysics

[Apr11a] E. Aprile et al., Phys. Rev. Lett. **107**, 131302 (2011)
Dark Matter Results from 100 Live Days of XENON100 Data

[Apr11b] E. Aprile et al., arXiv:1107.2155v1
The XENON100 Dark Matter Experiment

[Apr11c] E. Aprile at al. (XENON100 Collaboration), Phys. Rev. D **83**, (2011) 082001
Study of the electromagnetic background in the XENON100 experiment

[Apr11d] E. Aprile et al. (XENON100 Collaboration), Astropart. Phys. **35**, 43-49, 2011
Material screening and selection for XENON100

[Apr11e] E. Aprile et al., Astropart. Phys. **34**, 679-698, 2011
Design and Performance of the XENON10 Dark Matter Experiment

[Bag89] V. S. Bagnato et al., Opt. Commun. **72**, 76-81 (1989)
Study of laser deceleration of an atomic beam by monitoring the fluorescence along the deceleration path

[Bak76] G. Bakale et al., J. Phys. Chem. **80** (1976) 2556
Effect of an electric field on electron attachment to sulfur hexafluoride, nitrous oxide, and molecular oxygen in liquid argon and xenon

[Bal05] A. Baldini et al. (MEG Collaboration), Nucl. Instr. Meth. Phys. Res. Sect. A **545** (2005) 753
Absorption of scintillation light in a 100 l liquid xenon γ-ray detector and expected detector performance

[Bea02] J. F. Beacon and N. F. Bell, Phys.Rev. D **65** (2002) 113009
Do solar neutrinos decay?

[Beg03] M. C. Begelman, Science **300**, 1898 (2003), Evidence for Black Holes

[Beg91] K. G. Begeman et al., Mon. Not. R. Astron. Soc. **249** (1991) 523

[Ber02] R. Bernabei et al. (DAMA Collaboration), Nucl. Phys. B **110** (Proc. Suppl.) (2002) 88

[Ber08] R. Bernabei et al., Eur. Phys. J. C **56**, 333-355, 2008
First results from DAMA/LIBRA and the combined results with DAMA/NaI

[Ber04] G. Bertone et al., Phys. Rep. **405** (2005) 279-390
Particle Dark Matter: Evidence, Candidates and Constraints

[Bet02] A. Bettini, Highlits from Gran Sasso - 40th International School of Subnuclear Physics - Erice 2002

[Bla97] K. Blaum, Diploma thesis, Optimierung eines Quadrupol-Massenspektrometers zur isotopenselektiven Ultraspurenbestimmung, Institut für Physik, Johannes Gutenberg-Universität Mainz, 1997

[Bon64] A. Bondi, J. Phys. Chem., **68** (3), pp 441–451, 1964
Van der Waals Volumes and Radii

[Bro10] E. Brown, Search for Low Mass Dark Matter with the XENON100 Experiment and Simulations for 1 ton and 10 ton Dark Matter Detectors, University of California, Los Angeles, 2010

[Cer02] A. C. S. Readhead et al., Astrophys. J. **609** (2004) 498-512
Extended Mosaic Observations with the Cosmic Background Imager

[Che99] C. Y. Chen et al., Science **286** (1999) 1139
Ultrasensitive Isotope Trace Analyses with a Magneto-Optical Trap

[Clo06] D. Clowe et al, ApJ Letters in press 2008
A Direct Empirical Proof of the Existance of Dark Matter

[Day54] I. E. Dayton et al., Rev. Sci. Instrum. **25**, 485 (1954)
The Measurement of Two-Dimensional Fields. Part II: Study of a Quadrupole Magnet

[Dea51] R. B. Dean and W. J. Dixon, Anal. Chem., **23**, (4), pp 636–638, 1951
Simplified Statistics for Small Numbers of Observations

[Des05] DESY Hamburg, Presse-Bildarchiv, 21.01.2012

[Dob11] A. Dobi et al., Department of Physics, University of Maryland, College park MD, 2011
Detection of krypton in xenon for dark matter applications

[Dok81] T. Doke, Nuclear Instruments and Methods in Physics Research A **545** (2005) 753–764
Absorption of scintillation light in a 100 L liquid xenon γ-ray detector and expected detector performance

[Du99] Z. Du et al., J. Anal. At. Spectrom **14**, 1111 (1999)
Elemenal analysis with quadrupole mass filters operated in higher stbility regions

[Dur01] R. Durrer,arXiv:astro-ph/0109274v1
Physics of Cosmic Microwave Background anisotropies and primordial fluctuations

[Ein36] A. Einstein, Science **84**, 506 (1936)
Lens-like action of a star by the deviation of light in the gravitational field

[Fix96] D.J. Fixcen et al., Astrophys. J. **473** (1996) 576
The Cosmic Microwave Background Spectrum from the Full COBE/FIRAS Data Set

[Fre00] K. Freese, arXiv:astro-ph/0007444v1
Death of Stellar Baryonic Dark Matter Candidates

[Fre06] K. Freese, Nuclear Instruments and Methods in Physics Research A **559** (2006) 337-340
The dark side of the universe

[Gam48] G. Gamow, Phs. Rev. **74** (1948) 505
The Origin of Elements and the Separation of Galaxies

[Gro04] J. Gross, Mass Spectrometry, A Textbook; Springer; 2004

[Gru05] C. Grupen, Astroparticle Physics, Springer 2005

[Häu06] P. Häussinger et al., doi:10.1002/14356007.a17_485
Noble Gases, Ullmann's Encyclopedia of Industrial Chemistry. Wiley-VCH, Weinheim 2006

[Hin09] G. Hinshaw et al., Astrophys. J. Suppl. **180**, 225-245, 2009
Five-Year Wilkinson Microwave Anisotropy Probe (WMAP) Observations: Data Processing, Sky Maps, and Basic Results

[Ho08] S. Ho et al., Phys. Rev. D **78**, 043519 (2008)
Correlation of CMB with large-scale structure. I. Integrated Sachs-Wolfe tomography and cosmological implications

[Hu02] W. Hu and S. Dodelson, Ann. Rev. Astron. Astrophys. **40** 2002 (171)
Cosmic Microwave Background Anisotropies

[Inf04] Inficon, Technical Note, 2004

[Jim11] R. Jimenez et al., Phys. Lett. B **703**, 232, 2011
Peccei-Quinn axions from frequency dependence radiation dimming

[Jor65] J. Jortner et al., J. Chem. Phys. **42**, 4250 (1965)
Localized Excitations in Condensed Ne, Ar, Kr, and Xe

[Jou04] K. Jousten (Hrsg.), Wutz Handbuch Vakuumtechnik, Theorie und Praxis, 9. Auflage, Vieweg, 2006

[Jun96] G. Jungman et al., Phys. Rept., **267** (1996) 195-373
Supersymmetric Dark Matter

[Kit06] C. Kittel, Einführung in die Festkörperphysik, Oldenbourg Wissenschaftsverlag GmbH, 14. Auflage, 2006

[Kra05] C. Kra et al., Eur. Phys. J. C **40** (2005)
Final results from phase II of the Mainz neutrino mass searchin tritium beta-decay

[Kra89] L. M. Krauss and P. Romanelli, Phys. Rev. D **39**, 1225–1228 (1989)
New signatures for dark-matter detectors

[Lob03] V. M. Lobashev, Nucl. Phys. A, **719** C153-C160 (2003)
The search for the neutrino mass by direct method in the tritium beta-decay and perspectives of study it in the project KATRIN

[McL47] N. W. McLachlan, Theory and Application of Mathieu-Functions, Clarendon-Press, Oxford (1947)

[Mei11] Y. Mei, PhD Thesis, Direct Dark Matter Search with the XENON100 Experiment, Rice University, 2011

[Mey62] S. Meyerson and R. W. Van der Haar, J. Chem. Phys., **37**, 2458-2462, 1962
Multiply Charged Organic Ions in Mass Spectra

[Mul57] C. A. Muller and J. H. Oort, Nature **168**, 357 - 358 (1951)
The Interstellar Hydrogen Line at 1,420 Mc./sec., and an Estimate of Galactic Rotation

[Nol06] W. Nolting, Grundkurs Theoretische Physik 1 - Klassische Mechanik, Springer-Verlag, 8. Auflage, 2006

[Knu10] M. Knudsen, Ann. Phys. (Leipzig) **31** (1910) 633

[Leo10] D.S. Leonard et al., Nuclear Instruments and Methods in Physics Research A **621** (2010) 678-684
A simple high-sensitivity technique for purity analysis of xenon gas

[Ost03] J. P. Ostriker and P. Steinhardt, Science **300** (2003) 1909
New Light on Dark Matter

[Ozo05] K. Ozone, PhD Thesis, Liquid Xenon Scintillation Detector for the New $\mu \to e\gamma$ Search Experiment, University of Tokyo, Department of Physics, 2005

[Par10] Particle Physics Booklet, Journal of Physics G **37**, 075021 (2010)

[Pen65] A. A. Penzias and R. W. Wilson, Astrophys. J. **142** (1965) 419
A Measurement of Excess Antenna Temperature at 4080 Mc/s

[Phi91] W. Phillips and H. Metcalf, Phys. Rev. Lett. **48**, 596 (1982)
Laser Deceleration of an Atomic Beam

[Pol64] G. Pollack, Rev. Mod. Phys. **36**, 748-791 (1964)
The Solid State of Rare Gases

[Ror91] D. B. Rorabacher, Anal. Chem., **63** (2), 139–146. (1991)
Statistical Treatment for Rejection of Deviant Values: Critical Values of Dixon Q Parameter and Related Subrange Ratios at the 95 percent Confidence Level.

[Ros13] S. Rosendahl, PhD thesis, 2013

[San02] R. H. Sanders and S. S. McGaugh, Ann. Rev. Astron. Astrophys. **40** (2002) 263-317
Modified Newtonian Dynamics as an Alternative to Dark Matter

[Scr03] R. Scranton et al, arXiv:astro-ph/0307335v2
Physical Evidence for Dark Energy

[Sea62] D. Sears and H. Klug, J. Chem. Phys. **37**, 3002 (1962)
Density and Expansivity of Solid Xenon

[Sil85] J. Silk et al., Phys. Rev. Lett. **55**, 257–259 (1985)
The photino, the sun, and high-energy neutrinos

[Sil68] J. Silk, Astrophys. Journal, **151**, 459-471 (1968)
Cosmic black-body radiation and galaxy formation

[Smi96] A. Y. Smirnov and F. Vissani, Phys. Lett. B **380** (1996) 317-323
Upper bound on all products of R-parity violating couplings λ' and λ'' from proton decay

[Sol04] V. N. Solovov et al., Nucl. Instr. Meth. Phys. Res. Sect. A **516** (2004) 462
Measurement of the refractive index and attenuation length of liquid xenon for its scintillation light

[Spr09] A. Sprenger, Setup of the mass spectrometer and high vacuum experiment for the bachelor laboratory class “Scientific Instrumentatin”, Institut für Kernphysik, Uni Münster, 2009

[Tig06] Instruction Manual, Halo+^{TM} Trace Gas Analyzer, M7103 Series Rev. D, Tiger Optics, 2006

[Umr07] W. Umrath, Fundamentals of Vacuum Technology, Cologne, 2007

[Whi83] S. D. White et al., Astrophysical Journal, **274**:L1-L5, 1983
Clustering in a neutrino-dominated universe

[Wil09] D. R. Williams, Earth Fact Sheet NASA, Greenbelt, May 2009

[Yam04] M. Yamashita et al., Nucl. Instr. Meth. Phys. Res. Sect. A **535** (2004) 692
Scintillation response of liquid Xe surrounded by PTFE reflector for gamma rays

[Zwi33] F. Zwicky, Helv. Phys. Acta. **6**, 124 (1933)

[Zwi37] F. Zwicky, Phys. Rev. **51**, 290–290 (1937)
Nebulae as Gravitational Lenses

Declaration

I declare that I have written this diploma thesis on my own and have not used other sources than those I referred to. All parts of the thesis which correspond to other literature have been marked by referring to the source. This is valid for graphics and other drawings, too.

Eigenständigkeitserklärung

Ich versichere, dass ich die vorliegende schriftliche Diplomarbeit selbstständig verfasst und keine anderen als die angegebenen Quellen und Hilfsmittel benutzt habe. Alle Stellen der Arbeit, die anderen Werken dem Wortlaut oder Sinn nach entnommen wurden, habe ich in jedem Fall unter Angabe der Quelle als Entlehnung kenntlich gemacht. Das gleiche gilt für Zeichnungen und andere Darstellungen.

Acknowledgements

Great thanks to Prof. Dr. C. Weinheimer for the opportunity to work at this challenging project. Furthermore I am grateful for this support and engagement even though he was always short of time.

Thanks to Prof. Dr. A. Khoukaz for his revision on this thesis.

Special thankts to Stephan Rosendahl for all his support and supervision, especially at the beginning of my work.

Thanks to Dr. Ethan Brown for all his support and supervision.

Thanks a lot to Stephan Bauer and Johannes Schulz for their regular visits in the lab, which caused a lot of fun.

Thanks to Christian Huhmann and all engineers for their technical help with the experimental setup.

Thank-you to the XENON team for a joyful time. It is amazing what can be created from a bunch of valves.

Thanks to Gerda Kaninenberg and Stefan Lennardt for the pleasure of physics.

Further thanks goes to Stephan Bauer, Dr. Ethan Brown, Dr. Volker Hannen, Dr. Friedrich Hülsmann, Cecilia Levy, Stephan Rosendahl, Friederike Schröter as well as Ricarda Wagner for their suggestions and comments on this thesis.

Many thanks to my mother for her support and the offer to study both in Münster and abroad.

Special thanks to my father† for all his advice and the discussions, which caused my interest in science.

Great thanks to my girlfriend Friederike Schröter, for all of her support and motivation. Without you I would not have succeeded in my work. Thank you!

Danksagung

Herrn Prof. Dr. C. Weinheimer danke ich für die Aufnahme in seine Arbeitsgruppe und die Möglichkeit an diesem spannenden Projekt mitarbeiten zu können. Ebenso möchte ich mich für seine Unterstützung und sein persönliches Engagement bedanken und dass er trotz seines engen Terminplans immer für Fragen zur Verfügung stand.

Herrn Prof. Dr. A. Khoukaz danke ich für die Übernahme der Zweitkorrektur dieser Arbeit.

Stephan Rosendahl danke ich für seine Unterstützung und Anleitung, insbesondere zu Beginn meiner Arbeit.

Dr. Ethan Brown danke ich für seine Unterstützung und Anleitung.

Stephan Bauer und Johannes Schulz danke ich für ihre regelmäßigen Besuche im Praktikum. Ohne euch wäre es im Labor nich so lustig gewesen.

Christian Huhmann sowie allen Ingenieuren und Technikern danke ich für ihre Unterstützung beim Auf- und Umbauen des Experiments.

Dem XENON Team danke ich für eine wunderbare und spaßige Zeit. Es ist erstaunlich, was man alles aus einem Ventilhaufen machen kann.

Gerda Kaninenberg und Stefan Lennardt danke ich für die Freude an der Physik.

Stephan Bauer, Dr. Ethan Brown, Dr. Volker Hannen, Dr. Friedrich Hülsmann, Cecilia Levy, Stephan Rosendahl, Friederike Schröter sowie Ricarda Wagner danke ich für ihre Korrekturvorschläge und Anmerkungen zu dieser Arbeit.

Meiner Mutter danke ich für all ihre Unterstützung, dafür dass sie immer für mich da war und nicht zuletzt dafür, dass sie mir das Studium ermöglicht hat.

Meinem Vater† danke ich für seine guten Ratschläge und die vielen Diskussionen, die letztendlich mein Interesse an Naturwissenschaften geweckt haben.

Besonderer Dank gilt meiner Freundin Friederike Schröter, für all ihre Unterstützung und Motivition. Ohne Dich hätte ich das alles nicht geschafft, ich danke Dir.